Accurate cosmological inference in a gravitationally distorted Universe : Learning from simulated gravitationally lensed systems

Lyne Van de Vyvere

Dissertation presented for the degree of
Doctor of Philosophy in Space Sciences

Université de Liège
Faculté des Sciences
Département d'Astrophysique, de Géophysique et d'Océanographie
Unité de recherche STAR

– October 2022 –

Accurate cosmological inference in a gravitationally distorted Universe : Learning from simulated gravitationally lensed systems

Lyne Van de Vyvere

Dissertation presented for the degree of
Doctor of Philosophy in Space Sciences

Université de Liège
Faculté des Sciences
Département d'Astrophysique, de Géophysique et d'Océanographie
Unité de recherche STAR

– October 2022 –

Supervisor:

Dr. Dominique Sluse

Jury members:

Dr. Valérie Van Grootel	*President*
Dr. Damien Hutsemékers	*Secretary*
Pr. Pierre Magain	
Pr. Frédéric Courbin	
Pr. Simon Birrer	
Dr. Dominique Sluse	

This work is supported by the ERC grant COSMICLENS (No 787886)

RÉSUMÉ

En cosmologie, l'un des paramètres clés à connaître est la constante de Hubble, H_0. La constante de Hubble est le taux actuel d'expansion de l'Univers et différentes méthodes permettent de la calculer. Ces dernières années, une tension est apparue entre la valeur de H_0 basée sur l'Univers lointain et celle reposant sur des mesures de distances dans l'Univers proche. Dans ce contexte, l'utilisation de lentilles gravitationnelles pour obtenir une valeur précise de H_0 est prometteuse car elle est basée sur l'Univers proche mais ne se repose pas sur un étalon de distance primaire. Comme les objets massifs déforment l'espace-temps, une source de lumière située derrière une galaxie massive peut être imagée plusieurs fois, on parle alors de lentille gravitationnelle. Si la source est variable, on peut observer un délai entre l'apparition de la variation lumineuse dans les différentes images, et ce délai est inversement proportionnel à la constante de Hubble. Ce facteur de proportionnalité dépend de la masse de la lentille. En modélisant cette dernière et en mesurant le délai, il est possible de calculer H_0. Toutefois, la précision et l'exactitude pouvant être atteintes par cette méthode peuvent dépendre des hypothèses de travail. Il est donc essentiel de rechercher les sources d'erreurs potentielles et de les quantifier.

Les modèles de masse de lentilles gravitationnelles les plus utilisés possèdent une symétrie elliptique[1]. En effet, les lentilles sont généralement des galaxies dites elliptiques[2] qui, en première approximation, présentent bel et bien une telle symétrie. Cependant, les observations plus détaillées de ces dernières révèlent qu'elles sont plus complexes qu'il n'y paraît. En tenant compte de ces complexités, j'ai réalisé des simulations et ainsi testé l'influence de l'hypothèse de symétrie elliptique pour le modèle de la masse de la galaxie lentille. Plus précisément, j'ai exploré l'influence de plusieurs structures dites azimutales qui complexifient la masse: le moment octupolaire, c'est-à-dire la modification d'une forme elliptique vers une forme rectan-

[1] Les contours d'isodensités sont des ellipses concentriques qui possèdent la même orientation et la même ellipticité.

[2] Les galaxies sont généralement classées dans deux grandes catégories: les galaxies spirales, qui sont formées d'un disque plat avec un bulbe sphérique au centre, le tout entouré d'un halo de matière non visible, et les galaxies elliptiques, qui se présentent comme des grandes sphères ou ellipsoïdes plutôt homogènes.

gulaire ou de disque, et les variations d'ellipticité et d'orientation avec le rayon. Plus généralement, la simulation d'observations de lentilles gravitationnelles requiert un modèle de masse, qui peut être soit analytique, soit pixélisé. Dans cette thèse, j'ai majoritairement simulé des lentilles à l'aide de modèles analytiques mais j'ai également exploré un des problèmes potentiels qui résultent de l'utilisation de cartes de masses pixélisées dans les simulations.

Les principaux résultats de cette thèse sont les suivants. (1) Les simulations de lentilles se basant sur une distribution de masse échantillonnée sur une grille (pixels) peuvent être altérées par des artéfacts. En effet, les cartes de masses ne peuvent s'étendre à l'infini et sont donc tronquées. Une telle troncature crée une asymétrie à la frontière de la carte qui se répercute sur les images multiples de la source de lumière, sous forme d'un cisaillement. Un cisaillement, qui se caractérise par une déformation (élongation/compression) des images lentillées, est naturellement présent dans les lentilles gravitationnelles à cause de la présence de galaxies se situant près de la galaxie lentille et dans sa ligne de vue. La troncature induit un cisaillement supplémentaire, qui est artificiel, et la modélisation du cisaillement des lentilles ainsi simulées s'en trouve biaisée. Une prescription pour réduire cet effet en fonction de la finalité des simulations est donnée dans cette thèse. (2) Lorsqu'une lentille est modélisée avec un modèle à symétrie elliptique alors que sa vraie masse est légèrement déformée vers une forme rectangulaire ou de disque, les effets de la déformation peuvent parfois passer inaperçus. En effet, cette déformation a bien un impact sur les images mais ce dernier peut être noyé dans le bruit, ou être confondu avec des structures de la lumière de la source. L'inférence de H_0 basée sur une seule lentille affichant de telles structures azimutales peut ainsi être biaisée de plusieurs pourcents. Néanmoins, l'inférence basée sur l'analyse d'une population de lentilles n'est pas biaisée car la contribution des lentilles en forme de disque est compensée par celle des lentilles plus rectangulaires. (3) Les gradients d'ellipticité et les changements d'orientation avec le rayon présents dans la masse des lentilles ont tous deux un impact sur la force et l'orientation du cisaillement modélisé. Cependant, les variations d'orientation n'influencent pas la détermination de H_0, alors que c'est le cas pour les variations d'ellipticité. La valeur de H_0 inférée pour une population de lentilles avec une variété de gradient d'ellipticité reste cependant correcte.

Pour résumer, le message à retenir de cette thèse est triple. Premièrement, la simulation d'observations de lentilles gravitationnelles à l'aide de cartes de masse doit être réalisée avec précaution. Deuxièmement, les cisaillements modélisés dans les lentilles gravitationnelles ne peuvent pas être considérés comme provenant uniquement de contributions externes à la lentille: des structures internes à la lentille peuvent aussi en créer. Troisièmement, l'inférence de H_0 grâce à une unique lentille gravitationnelle n'est pas robuste lorsque que la masse réelle de la lentille présente des structures azimutales qui ne sont pas modélisées.

ABSTRACT

In the field of cosmology, one of the few key parameters is the Hubble constant, H_0, i.e. the current expansion rate of the Universe. In the last decades, its measurement revealed a mismatch: measurements using probes based on the early Universe conflict with the ones calculated by using distances in the local Universe. In this context, strong gravitational lensing of variable sources is promising to infer a precise value of H_0, local and independent of any distance ladder. As massive objects curve the space time, a source of light behind a massive galaxy can be multiply imaged, and the difference in arrival time between the images is inversely proportional to the Hubble constant. The precision and accuracy one can achieve on H_0 using lensed quasars may however depend on the assumptions one makes on the mass distribution. Searching for potential systematics and quantifying them is thus essential.

Since lensing galaxies are mostly elliptical galaxies[3], the commonly employed mass models display elliptical symmetry[4]. However, elliptical galaxies have been abundantly observed and are known to be slightly more complex. In this thesis, the influence of using elliptical mass models on lensing galaxies which display azimuthal structures is examined thanks to simulations. Different major types of azimuthal structures are explored: the octupolar moment, i.e. boxyness and discyness, and the variations of ellipticity and position angle with radius. To create realistic mock observations of lensing systems, either analytical models or numerical mass maps can be used. While most simulations in this thesis used analytical models, the use of mass maps is also explored and one related problem is emphasized.

The main results are the following. (1) The use of mass distributions sampled on a grid to simulate lensing systems may introduce artefacts in the lensed images. Mass maps can not be infinite and they are consequently truncated. Such truncation introduces an asymmetry in the mass at the border of the map which impacts the multiple lensed images with a shear. Shear, which stretches and compresses the lensed images, naturally exists in lensing systems due to the galaxies in the vicinity and along the line-of-sight towards the system. However, the truncation also creates a shear, which

[3] In opposition to spiral galaxies which display a flat disk with a spherical bulge in the centre, embedded in a dark mater halo, elliptical galaxies are 3D ellipsoids or spheres.

[4] Iso-density contours are concentric ellipses displaying the same axis ratio and position angle.

is artificial and adds up to the fiducial one, hence biasing the model. A prescription to minimize this effect is given in this thesis. (2) The presence of boxyness and discyness in the mass of lensing galaxies may not always be visible: it can be absorbed as structures in the light model of the source, or can be hidden in the noise. Consequently, the H_0 inference from a single lensing system displaying such azimuthal structures can be biased by several percent. Nevertheless, the analysis of a population of lenses remains unbiased as the contribution of boxy lensing galaxies compensates the one of discy galaxies. (3) Twists and ellipticity gradients impact the strength and orientation of the modelled shear. While twists do not influence cosmography inference, the variations of ellipticity do. The inference on H_0 from a population of lensing systems however remains unbiased.

The take home message of this thesis is threefold. First, simulations of lensing systems using mass maps must always be done with caution. Second, modelled shears in lensing systems cannot be trusted as originating only from contributions which are external to the modelled lensing galaxies: internal structures of the lens may also contribute. Third, the cosmographic inference from a single lens system is not robust when the modelled lensing galaxy lacks the azimuthal freedom that is effectively present in its true mass.

ACKNOWLEDGEMENTS

I would like to thank many people who helped me in one way or another to complete this thesis.

I would never be there without my family, close friends and colleagues. I would like to thank my parents, my sister, and my grand-parents for always being there for me. My partner, Lionel P., also supported me in many ways and enlightened every day with running jokes. Clémentine, my office mate and friend, endured my tendency to sing with a smile, and team working made both our lives easier. It has been a real pleasure to share this office with her. My direct co-workers are also part of the reason why I managed to write this thesis, I would like to thank Dominique, Matt, Sampath, Aymeric, Dandan, Simon, and Fred for all the fruitful discussions. During these four years, I can not count how many times I went to one or another person in the building with coding problems, reasoning issues, or just because I was hungry or needed a break. I need to particularly thank Martin, Charly, Elsa, Lionel G., Judith, Antoine, Loïc, Joséphine, Guillaume, Ben, Said, Mathieu, Anindya, Zoe, Arjun, Pierre H., Jacob, Sophie, Lorenzo, Jahanvi, Manu M., Laetitia, Mathilde, Michaël, Manu J., Pierre M., Marc-Antoine, Valérie, Sandrine, Arlette, and many others.

I would like to give a special thank to Pierre M. for giving me my first experience in research, which definitely gave me a liking to it. Then, I would like to give a second special thank to Dominique for believing in me and giving me the opportunity to continue in research. I think the people you work with are in fact more important than the subject which you are working on. Dominique included me in many working groups, always being there, supervising and supporting me, while giving me the freedom to spread my wings. I consider myself as someone lucky: I had the opportunity to work on a wonderful subject with wonderful people. Thank you.

Finally, I also want to thank my dad and Dominique for the throughout review of the form and content of this manuscript. They did a wonderful job; the possible remaining typos or lack of information are on me.

I hope you will enjoy the reading ☺.

CONTENTS

List of Tables

List of Figures

CHAPTER 1

INTRODUCTION

Our whole universe was in a hot, dense state
Then nearly fourteen billion years ago expansion started, wait
The Earth began to cool, the autotrophs began to drool
Neanderthals developed tools
We built a wall (we built the pyramids)
Math, science, history, unraveling the mysteries
That all started with the big bang! Bang!

The Big Bang Theory - Theme Song

Each human perceives the world in its own way. Among them, the astronomers and astrophysicists tend to watch the sky to unravel the mysteries of objects so far away from us that we can barely imagine how they look like. Artists and scientists work together to create artistic views of astrophysical phenomena, mostly based on data but always with an imaginary touch. The further away, the more complex it is to represent the objects accurately. It is even harder to picture the whole Universe in its current state and its evolution through time.

The scientific method to unravel those mysteries is based on observations, that provide exploitable data, as well as on models that are being refined over time to better represent those observations. With the advent of new relevant models, our understanding of the processes at work increases. It can sometimes be like an evidence, like a jigsaw puzzle piece that finally find its place, but it often opens even more questions and possible interpretations. As each new theory is by definition based on underlying

assumptions, the "plausibility" of those assumptions and theories are repeatedly being questioned by scientists, feeding the never-ending cycle of knowledge evolution. I stepped into this cycle four years ago and since then, I have been working to better understand and criticize the assumptions on which the strong gravitational lensing analyses are based, with an increased assiduity when such a phenomenon is used as a cosmological probe.

In Section 1.1, I will focus on the most recent, and most accepted theory of the Universe evolution, the flat ΛCDM model, and will introduce the different methods used to constrain the Hubble constant (H_0), a key parameter in cosmology. In Section 1.2, I will dive into the gravitational lensing, its formalism, and its practical application for cosmography. In Section 1.3, I will discuss the morphologies of elliptical galaxies as they dominate the lens population, and introduce the power-law lens model which is often used in lensing studies. Finally, the thesis structure is laid out in Section 1.4.

1.1 Cosmological context

The **flat Lambda Cold Dark Matter** (flat ΛCDM) **cosmological model** is nowadays the most widely accepted model to describe the Universe state and its evolution. According to this theory, the Universe is made of 4 main ingredients: 1) the baryonic matter that we can typically observe, 2) the non-baryonic, collisionless, and dissipationless dark matter which is "cold", i.e. moving at a non-relativistic speed, 3) the radiation, including for instance the neutrinos, and 4) the dark energy which accelerates the expansion of the Universe. The Universe at present-day is composed of approximately 70% of dark energy and 30% of matter, according to cosmological measurement for this cosmological model. The Universe is also homogeneous, isotropic, and flat due to its expansion since the inflation. The nature of the dark energy, which is vacuum energy in this model and associated with the cosmological constant Λ, remains unknown. Nevertheless, the expansion (and acceleration of the expansion) of the Universe has been observed.

The expansion of the Universe has been theorised since the twenties and in 1929, Edwin Hubble observed that galaxies were moving away from us with a speed proportional to the distance between the Earth and the galaxy. This phenomenon is now understood as the imprint of the space-time dilation. In the nineties, thanks to supernovae observations, our Universe was found to be in fact in an accelerated expansion. The expansion rate of the Universe is called the Hubble parameter and its value at our epoch is known as the **Hubble constant** (H_0).

In recent years, scientists have used different methods to calculate the Hubble constant based on different observations. Some methods are **based on the observation** of imprints of **the early times of the Universe** thanks to the Cosmic Microwave Background (CMB) or the Baryonic Accoustics Oscillations (BAO). In short, in the

early primordial Universe photons and matter were bound together, the photons were unable to move far away as they were absorbed by ions to make the latter vibrate. This equilibrium of gravitation versus pressure generated density waves which created over- and sub-densities. At the recombination epoch, those over- and sub-density patterns were freezed: the photons escaped while the matter, moving more slowly, stayed in place. The photons near over-densities reddened while the the ones in sub-densities environments became bluer. The imprint of those photons are present in the CMB. By studying the fluctuations in the CMB, one can infer the characteristic size of the structures in the early Universe. The current spatial distribution of galaxies is also a tracer of that early epoch, as our current galaxies arise from those over- and sub-densities and are traces of the BAO. The statistical observation of galaxies distribution or the observation of the CMB allow one to visualize the early universe and infer the Hubble constant by assuming a given cosmology. Concurrently, other methods to determine H_0 are **based on observations** of the local expansion of **the Universe in recent times**. Most methods are based on the following: thanks to knowledge about a given phenomenon (like the period-luminosity relation for Cepheids, the parallax measurements, the properties of eclipsing binaries, type Ia supernovae luminosities, Miras stars properties, characteristics of stars on the tip of the red giant branch (TRGB), the Tully-Fisher relation, the surface brightness fluctuations of galaxies (SBF), etc) it is possible to retrieve distances to astrophysical objects and, thanks to the redshift of those objects, one can calculate the expansion rate of the "local" Universe. On the one hand, some distance measurements methods are "rulers", i.e. they are independent of a calibration from other methods for the distance measurements, such as the parallax method, the detached eclipsing binaries or the maser orbits. Some other techniques, on the other hand, depend on those rulers because they need to be calibrated to allow distance measurements. Among others the type Ia supernovae and Cepheids are examples of standard candles: their absolute magnitudes follow a law which has to be calibrated and, once calibrated, the distance can then be calculated by comparing the apparent brightness with the theoretical one. For example, the type Ia supernovae have characteristic luminosity profiles and are so luminous that they can be seen in distant galaxies. They have been observed up to redshift 1.914. But their distances need to be calibrated, by using other supernovae in the vicinity of another probe, such as the Cepheids. The Cepheids are variable stars which show a relationship between the period of variation and their luminosity. The latter also have to be calibrated thanks to nearby Cepheids, provided that they have similar properties, even if the Cepheid arises from different environments. The parallax method, which is a ruler independent of other probes, can be used to calculate the distances of the nearby Cepheids and hence calibrate the period-luminosity relation. This succession of interdependent distance measurements forms what we call the "distance ladder" and allows one to measure the Hubble constant and even the acceleration of the expansion of the Universe. Finally, the **time-delay gravitational**

lensing phenomenon can also be used to retrieve the Hubble constant in the "late" Universe (as opposed to "early" Universe which refers to the status of the Universe in its earliest times). This approach uses the difference of time that light-rays from a luminous source take to propagate in the Universe when they accouter a gravitational potential which is so strong that several images of the source can be observed from Earth. Due to the gravitational time dilation and the geometrical difference of length of the different paths that the light takes, there can be a delay between the different images of the same background object. This delay is inversely proportional to the Hubble constant. Since my thesis focus on this method, it will be more extensively explained in Section 1.2.

The scientists using the different methods to determine H_0 recovered different values for the expansion rate of the Universe. Figure 1.1 summarizes the main recent measurements of H_0. The first 5 measurements in Figure 1.1 are based on the CMB, the BAO, and the Big Bang Nucleosynthesis (BBN). They are thus based on the observation of imprints of the early times of the Universe. The ground-base result in the community for the measurement of H_0 based on the "early" Universe is the one from Planck Collaboration et al. (2020) (hereafter cited as Planck 2018) who found $H_0 = 67.4 \pm 0.5\,\mathrm{km\,s^{-1}\,Mpc^{-1}}$. The other measurements, based on TRGB, time-delays, Cepheids, SBF, and Megamaser, are all probing the expansion of the Universe from observations of the Universe in its recent state. The key number that is quoted as the local measurement of H_0 is the one from Riess et al. (2021) (hereafter cited as SH0ES 2021) who found $H_0 = 73.2 \pm 1.3\,\mathrm{km\,s^{-1}\,Mpc^{-1}}$. This measurement shows a 4.2 σ difference with the result from Planck 2018.

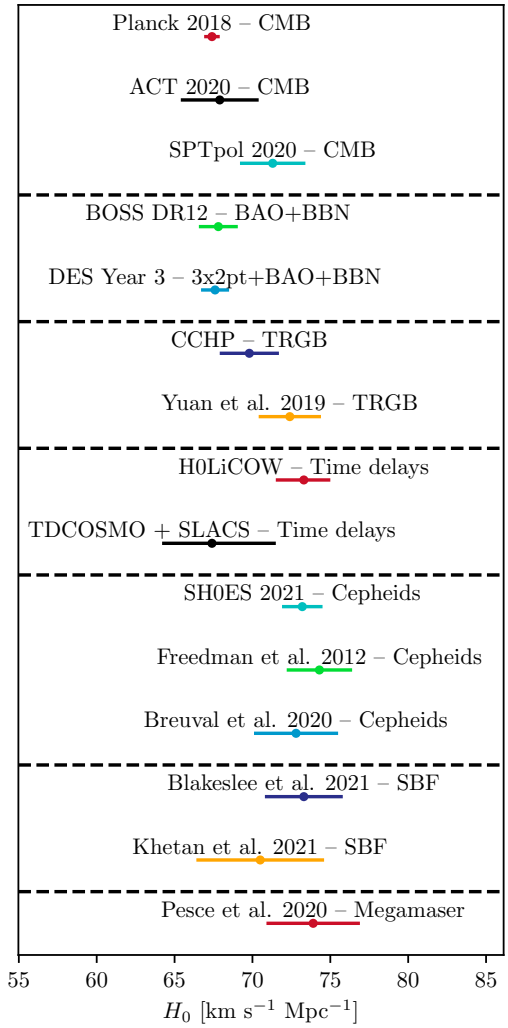

Figure 1.1: Summary of the recent H_0 measurements from Shah et al. (2021).

Notes. From top to bottom: results from the space-based Planck mission observing the CMB (Planck 2018) ; results from ground-based Atacama Cosmology Telescope (ATC) observations of the CMB (Aiola et al. 2020) ; results from the ground-based South Pole Telescope (SPT) observations of the CMB (Henning et al. 2018; Bianchini et al. 2020) ;

Notes. results from BAO measurements using the Baryon Oscillation Spectroscopic Survey (BOSS) (Alam et al. 2017) with extra constraint from BBN ; results from the Dark Energy Survey (DES) Year 3 observations of the BAO, using three two-point correlation functions and extra constrain from BNN (Abbott et al. 2022) ; results from the Carnegie-Chicago Hubble Program (CCHP) using supernovae calibrated with the TRGB, itself calibrated to the Large Magellanic Cloud (LMC) with eclipsing binaries and parallax distance measurements (Freedman et al. 2019) ; results from Yuan et al. (2019) using supernovae calibrated with the TRGB, itself calibrated to the LMC as Freedman et al. (2019) but with different photometry references and reddening maps ; results from 6 time-delay lenses from the H0LiCOW Collaboration (H_0 Lenses in COSMOGRAIL's Wellspring) (Wong et al. 2020) ; results from 7 time-delays lenses with constraints from 33 non-time-delay lenses from the Sloan Lens ACS Survey (Birrer et al. 2020) ; results from distance ladder of type Ia supernovae calibrated with Cepheids, including 75 Cepheids in the Milky Way with parallax measurements (SH0ES 2021) ; results from the distance ladder with the Cepheids period-luminosity relation calibrated thanks to infrared (IR) observations with the Spitzer Space Telescope (Freedman et al. 2012) ; results from the distance ladder with the Cepheids period-luminosity relation calibrated based on parallax of host clusters of the Cepheids or spatially resolved companions of the Cepheids (instead of the parallax of the Cepheids themselves) to avoid the systematics due to the absence of chromatic correction or saturation (Breuval et al. 2020) ; results from the distance ladder with supernovae calibrated using SBF observed in the IR with the Hubble Space Telescope (HST), themselves calibrated with Cepheids and TRGB (Blakeslee et al. 2021) ; results from the distance ladder with supernovae calibrated with SBF coming from different catalogs (Khetan et al. 2021) ; results from distance to 6 Megamaser hosting galaxies (Pesce et al. 2020).

The **discrepancy between the measurement of** H_0, thanks to either local observables or the global imprints of the early Universe, can have different explanations. On the one hand, **the observed discrepancy could be an artefact**. Indeed, one of the measurements can be biased due to insufficient knowledge. For instance, the properties of Cepheids can change depending on the environment or their compositions. A mis-calibration or an absence of calibration in that regard could bias the distances calculations. Secondly, a photometry bias may arise: different instruments, both space-based or ground-based, can not be one hundred percent equivalent. If a systematic error in the calibration of the photometry between different instruments occurs, the apparent brightness of the observed objects can be altered. Thirdly, there is a possibility that both late and early Universe measurements are in fact consistent if the uncertainties on the measurements are strongly underestimated. On the other hand, **the tension** between "early" and "late" Universe results **can be the evidence of an unknown physics**. First, the physics of the flat ΛCDM model may be perfectly right but the Universe in our vicinity could specifically not be representative of the global Universe. For instance, our local Universe could be in an under-dense area with a local value of H_0 which is different from the global one, as suggested by the "Hubble Bubble" theory. Another possibility is that the flat ΛCDM model does not

reproduce the history of our Universe, despite its goodness in predicting the primordial abundances and the CMB spectrum, and another model should in that case be adopted.

In this context, the time-delay gravitational lensing technique is particularly useful to explore the H_0 tension. Indeed, this technique probes the local Universe, with redshifts of the lens typically up to 0.8 and redshift of the source up to 2.5, but is independent of the distance ladder. The H_0 value based on 6 lensing systems studied in details by the H0LiCOW collaboration is $73.3^{+1.7}_{-1.8}$ km s^{-1} Mpc^{-1} (Wong et al. 2020). With 1) the addition of one more lensing system, 2) a more conservative handle of degeneracies and 3) using constrains on the mass profile of lensing galaxies based on a larger sample of non-time-delay lenses, the value becomes $67.4^{+4.1}_{-3.2}$ km s^{-1} Mpc^{-1} (Birrer et al. 2020, hereafter cited as TDCOSMO IV). While the first value is in agreement with the result from SH0ES 2021 and in disagreement with the Planck 2018, the second one has larger error bars and is consistent with both measurements. My thesis is at the heart of the research domain of time-delay cosmography with strong gravitational lensing and focuses on exploring the impact of different assumptions that are made in the current lensing analysis. The next section will provide a more in-depth introduction of the strong gravitational lensing technique.

1.2 Gravitational lensing

The phenomenon of strong gravitational lensing was first observed in 1979 by Walsh et al. (1979) who detected two quasars at the same redshift of 1.405 with great similarities in their spectra and separated by 5.7″. The probability of such coincidence was weak and the possibility that they were in fact two images of the same quasar was put forward. Soon after that, additional observations confirmed the similarity of the radio sources in spectra, and the lensing galaxy between the two images was detected. Even if the lensing phenomenon had already been established theoretically, the discovery of this system called QSO 0957+561 was marvelous and marked the beginning of several lensing systems discoveries. Indeed, one year later, another lensing system, PG 1115+080, was discovered by Weymann et al. (1980). This system was characterized by 3 images of the same quasar. It was found later on that it was in fact a quadruply-imaged source with two images very close to each other, around 0.5″separation, that were blended together in the first observations. Now, a total of 220 lensed quasars have been detected, one fourth being quadruply imaged (also called quads) and the remaining three fourth being mainly doubly imaged (also known as doubles)[1]. Nevertheless, the lensing of quasars is only a part of the strong gravitational lensing domain. And more broadly, there are in fact three categories of gravitational lensing: strong lensing, weak lensing and micro-lensing.

[1] We will later see that there is in fact a subtlety in the number of images.

Strong lensing is the deflection of the light rays from a background light source by the mass of a foreground object, typically a galaxy, called the lens, the deflection of the light rays (aka lensing) being so strong that the source is multiply imaged (as illustrated in Figure 1.2). The quasars are the first lensed sources that have been detected because they are particularly bright and their spectra can easily be compared. With current instruments, it is also possible to see the quasars' host galaxy. As they are a more extended source of light, their imaged fluxes are also more extended and can form arcs or even rings, depending on the lens-source configuration. Strong lensing of galaxies without quasar in their centre is also common. Those systems are however less known in the cosmological context as they do not allow direct measurement of the Hubble constant. Indeed, the H_0 calculation is allowed with strong gravitational lensing thanks to the time delay between several images of a same variable source. Lensed quasars, which are intrinsically variable, will have very luminous and localised images which can be monitored with ground-based telescopes during the time needed to get a delay, which can be several years. The lensed galaxies on the other hand are fainter, extended, and not specifically variable. Except if a supernova explosion occurs in the galaxy, a lensed galaxy without quasar in its centre can not be directly used for time-delay cosmography. Nevertheless, such lensing systems are useful to study the distribution of mass in lenses and several of those systems are now used to constrain the possible properties of lensing galaxies and thus helps constraining H_0 indirectly, as in TDCOSMO IV.

While a strong gravitational field can induce a splitting of the images of a background source, a weaker field can also change the shape of background sources without creating several images of them. Even if galaxies and cluster of galaxies are particularly massive and can produce several images of a background source if the latter is specifically positioned behind the lens, the light-rays travelling to us from a less aligned source would feel a weaker field and would undergo a weaker bending. Numerous background galaxies can thus have weakly distorted images, so that it is almost impossible to know if the observed ellipticity of each individual galaxy comes from its intrinsic shape or from a lensing effect resulting in an elongation in one direction (as can be seen at Figure 1.3). A population analysis is needed to constrain the weak gravitational lensing field. **Weak lensing** analysis thus requires a statistical study of the shape of numerous background light sources to infer the weak distortion arising from the presence of a gravitational field. This method allows one to construct a parameter-free map of the projected mass distribution. The precision of such a map depends on the number of sources that can be analyzed. To increase the number of light sources, fainter (and apparently smaller) background galaxies can be observed. However, the Point-Spread Function (PSF) blurs the measurements, and correction for its effect is still a challenge in weak lensing analyses. Moreover, observing more galaxies in large areas in the sky leads to large data sets which are also more difficult to handle. Those issues prevented most weak lensing studies before the nineties. Since

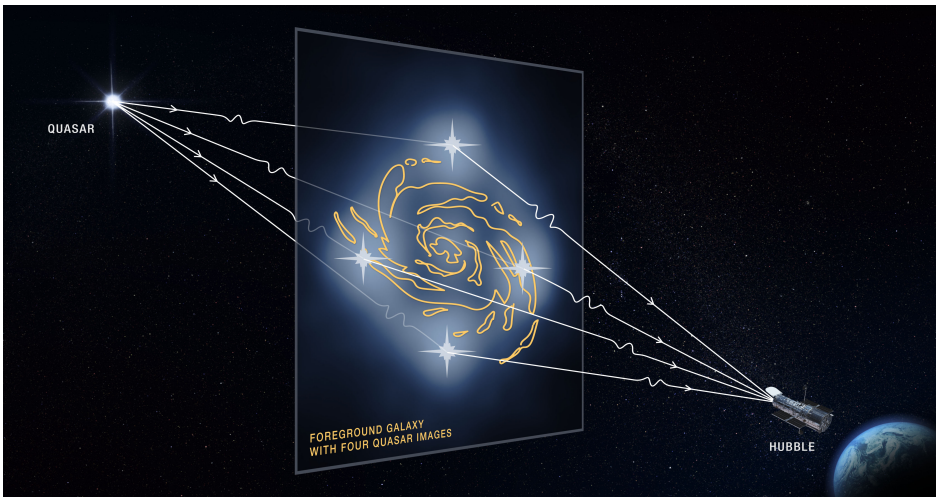

Figure 1.2: General illustration of strong gravitational lensing. A background quasar is strongly lensed by a foreground galaxy and four images of that quasar are visible by the observer. © ESA, NASA, D. Player

then, technological progress has been made: better telescopes and a better handle of the systematics associated to image processing have been developed. The interest in weak lensing also grew as studying the mass distribution in the Universe helps constraining cosmological parameters (but not specifically H_0) and it gained in credibility thanks to compatible results between different teams with different data sets.

The **micro-lensing** effect is similar to the strong lensing one: both involve a splitting of a background source of light into several images due to a gravitational potential. However, micro-lensing focuses on much smaller scales, with image separations of the order of milli-arcseconds, and lensing mass more typical of star-like objects, in the range of mass roughly between $10^{-6}M_\odot$ and $10^{6}M_\odot$. The different images at those scales can not be resolved with the telescopes. The micro-lensing effect can have numerous applications, the most popular one being that it can help searching for exoplanets. As a star passes behind another star in projection, it is magnified and can become multiply imaged. The unresolved light-curve of the background star will thus display a recognizable pattern. If the lensing star is not a single star but a binary system with another star or a planet, the light curve patterns will be different (as illustrated at Figure 1.4) and allows one to detect the presence of the companion, and hence search for exoplanets. While this effect is helpful in some cases, for instance to search for exoplanets, it can also degrade light curve analyses of other science cases if not taken into account. In time-delay strong lensing studies, micro-lensing is par-

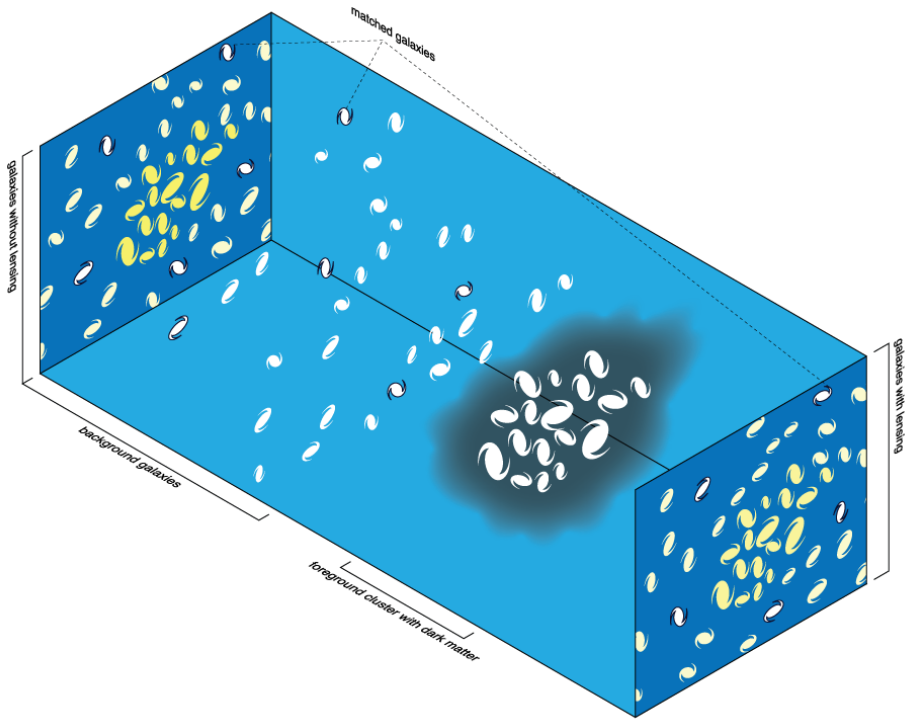

Figure 1.3: Illustration of weak lensing phenomenon. Several background sources of light are weakly lensed by a cluster and appear as globally slightly stretched for the observer. © M. Sachs

ticularly known to introduce specific patterns in the light curve of the quasar images. Indeed, any compact object in the light-ray path, like stars in the lensing galaxy, can also micro-lens the images on the quasar, on top of the global strong lensing of the lensing galaxy. The different macro images of a same quasar are, in that case, not micro-lensed by the same micro-lenses. While these effects are interesting as they may help study the quasars' structures, they are also troublesome to calculate accurate time delays between the different images as those micro-lensing events introduce a noise-like effect in each light curve.

More information on weak lensing formalism and applications can be found in Refregier (2003) and Schneider (2006). Courbin et al. (2002), Mollerach & Roulet (2002), and Wambsganss (2006) provide reviews of gravitational micro-lensing and detail its role in strong lensing of quasars. The strong lensing mechanism is also explained in Courbin et al. (2002), Kochanek (2006), and Treu & Marshall (2016), among others.

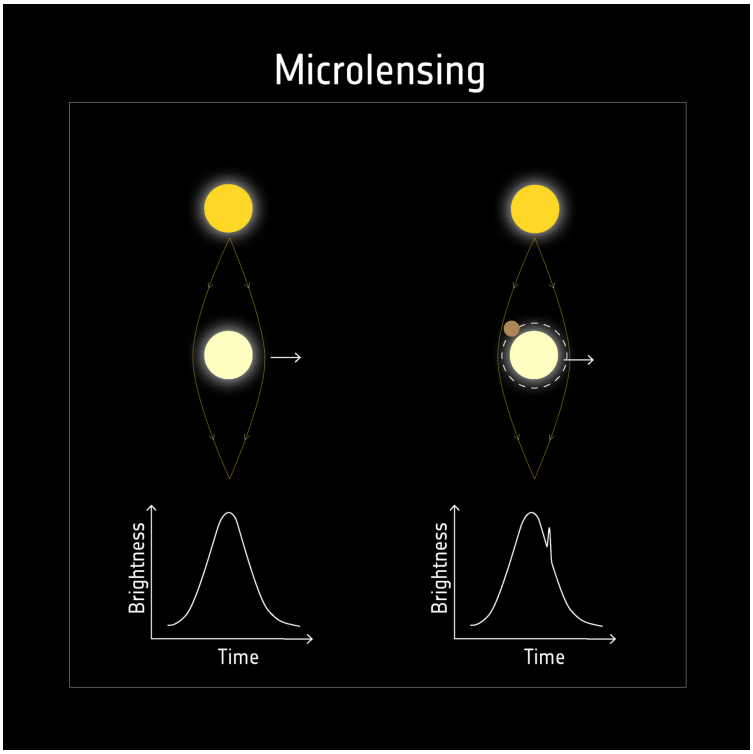

Figure 1.4: Detection of exoplanets thanks to micro-lensing patterns in light curves. © ESA

For completeness, the following sections will focus on the mathematical formalism of strong gravitational lensing and the major lens mass models, as they are key ingredients of my thesis.

1.2.1 Strong lensing formalism

As stated before, gravitational lensing is the deflection of light rays from a background source by a foreground mass called lens or deflector. Figure 1.5 schematically represents this situation. An observer will see a source of light at an angular position $\boldsymbol{\theta}$

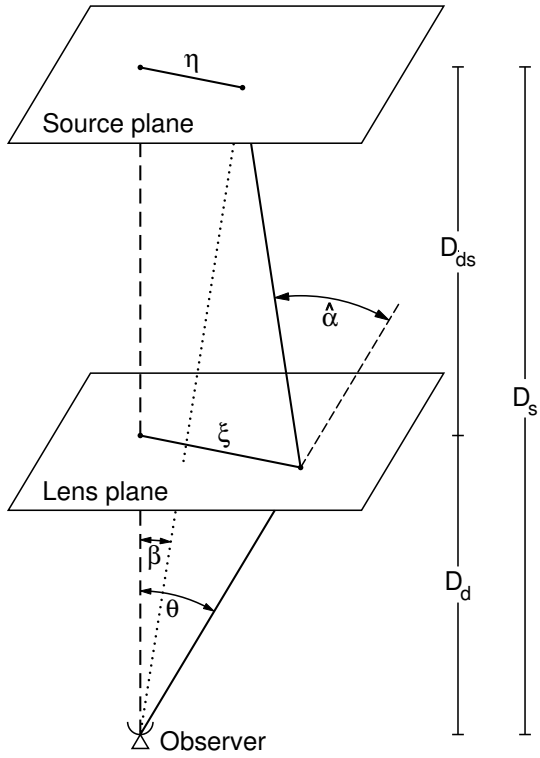

Figure 1.5: Lensing formalism diagram from Bartelmann & Schneider (2001)

Notes. The lens plane is also commonly named the image plane or the deflector plane. The name "image plane" can be seen as a misnomer since the lensed images have the same redshift as the background source they arise from. A 3D view of a lensing system should thus place the images of the source in the source plane and not in the lens plane. Nevertheless, the lens plane is often called the image plane for convenience. Another interpretation of the name "image plane" can be that, since observers retrieve images from CCD cameras on telescopes, the "image plane" can be seen as the plane of the physical picture/image which mostly photographs the lens.

while its intrinsic position is $\boldsymbol{\beta}$. Assuming that the angles are small[2], we have:

$$\boldsymbol{\theta} D_\mathrm{s} = \boldsymbol{\beta} D_\mathrm{s} + \hat{\boldsymbol{\alpha}} D_\mathrm{ds} \,, \tag{1.1}$$

where $\hat{\boldsymbol{\alpha}}$ is the deflection undergone by the light ray due to the mass, D_s is the angular diameter distance[3] between the observer and the source plane, and D_ds is the angular diameter distance between the lens plane and the source plane. The apparent (or reduced) deflection angle $\boldsymbol{\alpha}$ is defined as $\boldsymbol{\alpha} = \frac{D_\mathrm{ds}}{D_\mathrm{s}} \hat{\boldsymbol{\alpha}}$. Re-writing Equation 1.1, we have the well known **lens equation**:

$$\boldsymbol{\alpha} = \boldsymbol{\theta} - \boldsymbol{\beta} \,. \tag{1.2}$$

The reduced deflection angle is thus a very useful and intuitive quantity to use in lensing, as it is simply the difference between the angular position of the observed image of the light source and its intrinsic, not observable, "true" angular position. For simplicity, the reduced deflection angle $\boldsymbol{\alpha}$ will be called the **deflection angle**.

Linking the deflection angle to the mass that triggers such deflection can fortunately be done. In general relativity, we have

$$\hat{\boldsymbol{\alpha}}(\boldsymbol{\xi}) = \frac{4G}{c^2} \int d^2\boldsymbol{\xi}' \Sigma(\boldsymbol{\xi}') \frac{\boldsymbol{\xi} - \boldsymbol{\xi}'}{|\boldsymbol{\xi} - \boldsymbol{\xi}'|^2} \,, \tag{1.3}$$

where $\boldsymbol{\xi}$ is the impact parameter, G is the gravitational constant, c the speed of light, and Σ is the surface mass density. This relation is true provided that the deflector is a "thin lens", i.e. the distances between the source, lens and observer are much larger than the physical extent of the lens, which is generally true and specifically true for all the cases considered in this thesis. Since $\boldsymbol{\xi} = D_\mathrm{d}\boldsymbol{\theta}$, with D_d being the angular diameter distance to the lens, the previous equation can also be written as:

$$\boldsymbol{\alpha}(\boldsymbol{\theta}) = \frac{1}{\pi} \int_{\mathbb{R}^2} d^2\boldsymbol{\theta}' \kappa(\boldsymbol{\theta}') \frac{\boldsymbol{\theta} - \boldsymbol{\theta}'}{|\boldsymbol{\theta} - \boldsymbol{\theta}'|^2} \,, \tag{1.4}$$

with the **convergence**

$$\kappa(\boldsymbol{\theta}) = \frac{\Sigma(D_\mathrm{d}\boldsymbol{\theta})}{\Sigma_\mathrm{crit}} \quad , \quad \text{with } \Sigma_\mathrm{crit} = \frac{c^2}{4\pi G} \frac{D_\mathrm{s}}{D_\mathrm{d} D_\mathrm{ds}} \,. \tag{1.5}$$

We thus now have the link between the deflection angle and the mass which is responsible for it. The convergence κ is also called the dimensionless surface mass

[2] To approximate $\tan i = \frac{y}{x}$ by $i = \frac{y}{x}$, the angle i must be small or equivalently, $\frac{y}{x}$ must be small. In our case, it roughly translates into the condition that the size of a galaxy must be way smaller than the distance to the galaxy, as the effective half-light radius of lensing galaxies is in the same order of magnitude as the radius at which lensed images form. This condition is always satisfied in strong lensing.

[3] In general relativity, different types of distances can be defined. The angular diameter distance is defined as an object's physical size divided by its angular size when observed from Earth (or another origin). This distance is linked to the redshift of the object and is dependent on the assumed cosmology. A more formal definition will be provided later.

density and it can be shown that $\exists \boldsymbol{\theta} : \kappa(\boldsymbol{\theta}) \geq 1$ is a sufficient (not necessary) condition to have at least one position $\boldsymbol{\beta}$ in the source plane at which a light source can be multiply imaged by the lens. In other words, such a condition ensures that there is a source position $\boldsymbol{\beta}$ for which multiple solutions $\boldsymbol{\theta}$ can be found through solving the lens equation (1.2), the deflection angle $\boldsymbol{\alpha}$ being know through the convergence κ. We will later see another condition, which is necessary and sufficient, that ensures having a strong gravitational lens with multiple images.

The deflection angle can also be written as the gradient of the **lensing potential** ψ as

$$\boldsymbol{\alpha} = \boldsymbol{\nabla}\psi \,, \tag{1.6}$$

with

$$\psi(\boldsymbol{\theta}) = \frac{1}{\pi}\int_{\mathbb{R}^2} d^2\boldsymbol{\theta}'\kappa(\boldsymbol{\theta}')\ln|\boldsymbol{\theta}-\boldsymbol{\theta}'| \,. \tag{1.7}$$

The lensing potential thus also satisfies the Poisson equation

$$\boldsymbol{\nabla}^2\psi = 2\kappa \,, \tag{1.8}$$

where $\boldsymbol{\nabla}^2$ is the Laplacian operator. Though using deflection angle is very intuitive as it directly quantifies the amount of angular deviation of a light ray, it still remains a 2-dimensional quantity, and creating maps of deflection angles can be more complicated to visualize. Using the potential or the convergence can be more intuitive for physicists who are used to such quantities[4].

We have already seen that the first derivatives' vector of the lensing potential is the deflection angle. The second derivatives of the potential form the Hessian matrix, with the element (i,j) being $\frac{\partial^2\psi(\boldsymbol{\theta})}{\partial\theta_i\partial\theta_j}$, and is a useful quantity as well as it is linked to the magnification of a source of light through lensing.

Following Liouville's theorem and assuming no emission or absorption of photons occurs during the gravitational light deflection, the surface brightness of a source is conserved through lensing. As the source is lensed, it can thus be deformed and magnified. The Jacobian matrix $\mathscr{A}$ describes the mapping of an image from the lens plane to the source plane:

$$\mathscr{A}(\boldsymbol{\theta}) = \frac{\partial\boldsymbol{\beta}}{\partial\boldsymbol{\theta}} = \mathbb{1} - \boldsymbol{\nabla}\boldsymbol{\nabla}\psi = \left(\delta_{ij} - \frac{\partial^2\psi(\boldsymbol{\theta})}{\partial\theta_i\partial\theta_j}\right) . \tag{1.9}$$

The inverse of this Jacobian matrix, on the other hand, represents the deformation undergone by a source of light due to the gravitational potential of a lens. This inverse is called the magnification tensor $M(\boldsymbol{\theta}) = \mathscr{A}^{-1}$. Indeed, this quantity is $\frac{\partial\boldsymbol{\theta}}{\partial\boldsymbol{\beta}}$, and

[4] My opinion is that both convergence and lensing potential can be intuitive quantities used to visualize in 2D the mass of a lens: the advantage of the convergence being that it is directly proportional to the surface density ; and the advantage of the potential being that its derivatives (that one can intuitively guess by seeing the potential map) are useful quantities in lensing.

answers the question "if my source of light in the source plane has a given extent $d\boldsymbol{\beta}$, how does it appear when it is lensed ?". Since the the surface brightness is conserved through lensing, the ratio of the surface of a light source when lensed compared to its unlensed surface, provided that the source is small[5] is the **magnification** of the source. It is given by the determinant of the magnification tensor:

$$\mu(\boldsymbol{\theta}) = \det M(\boldsymbol{\theta}) = \frac{1}{\det \mathscr{A}(\boldsymbol{\theta})} \,. \tag{1.10}$$

It can be shown that $\exists \boldsymbol{\theta} : \det \mathscr{A}(\boldsymbol{\theta}) < 0$ is a sufficient and necessary condition for a lens to have multiple images of a source of light (provided it is placed in adequate regions in the source plane). In other words, this condition ensures that there is at least one $\boldsymbol{\beta}$ for which several $\boldsymbol{\theta}$ satisfy the lens equation (1.2). In the continuity, after knowing if there are several images created, one would also like to know how many there are and their positions. Different techniques can be used to know how many images will be created by a given lens for a given source position $\boldsymbol{\beta}$.

To find the number of images created in a lensing system for a given source position, one can solve the lens equation. However, another method using regions in the source and lens planes can also be used. One can first define the curves in the lens plane for which the determinant of the Jacobian is null, i.e. $\det \mathscr{A}(\boldsymbol{\theta}) = 0$. Such lines are characterized by infinite magnification, following Equation 1.10, and are called **critical curves**. The mapping of such lines in the source plane are called the **caustics**. For a single elliptical galaxy, the curves typically resemble what is shown in Figure 1.6, in the left panel for critical curves and in the right panel for caustics. The caustics define the areas in which a source is imaged multiple times. For a simple case as displayed at Figure 1.6, it can be shown that a source positioned within the innermost caustic will be imaged five times and a source positioned between the two caustics will be imaged three times (Burke 1981; Schneider et al. 2006). Nevertheless, one of the three or five images, the central one, will generally be highly de-magnified and blended with the lens light. We thus use the words **quads** and **doubles** when speaking of lensing systems which respectively display four or two bright images of the background source, commonly voiding the unseeable image. Depending on the source position compared to the caustic, the images will be displayed in given configurations. Figure 1.7 illustrates the three most encountered configurations in quads.

Another way to predict the images position is to use the arrival-time surface. For this purpose, we first need to define the **Fermat potential**:

$$\tau(\boldsymbol{\theta};\boldsymbol{\beta}) = \frac{1}{2}(\boldsymbol{\theta}-\boldsymbol{\beta})^2 - \psi(\boldsymbol{\theta}) \,. \tag{1.11}$$

[5]The size of the (lensed) source of light must be smaller than the typical scale on which the magnification tensor varies significantly.

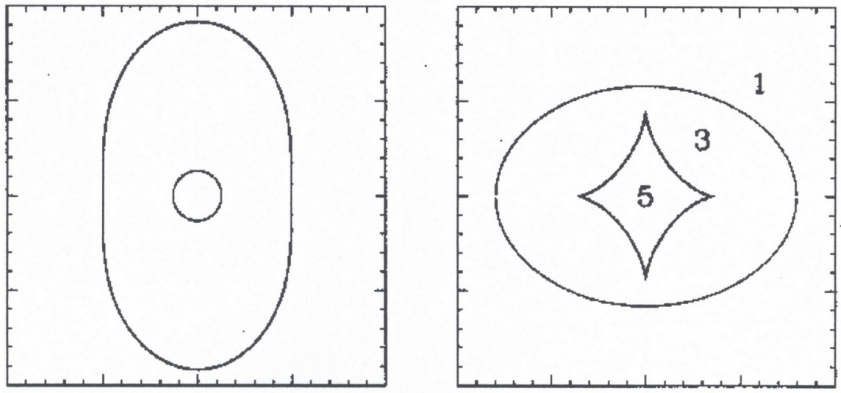

Figure 1.6: Critical curves in the lens plane (left) and caustics in the source plane (right) for a generic elliptical galaxy from Wambsganss (1998).

Notes. The inner critical curve transposes, in the source plane, to the outermost caustic. And reversely, the outermost critical curve transposes, in the source plane, to the innermost caustic. Any source placed inside the innermost caustic will be imaged 5 times. If a source is placed between the two caustics, three images will be created. Finally, if the source is placed outside the caustics, it can be magnified and distorted by lensing but not multiply imaged.

First of all, it can be noted that the Fermat potential is proportional to the excess of light travel time due to lensing compared to an unperturbed path, this excess of time being given by:

$$t(\boldsymbol{\theta};\boldsymbol{\beta}) = \frac{(1+z_\mathrm{d})}{c}\frac{D_\mathrm{d}D_\mathrm{s}}{D_\mathrm{ds}}\tau(\boldsymbol{\theta};\boldsymbol{\beta})\,, \tag{1.12}$$

where z_d is the redshift of the lens. The light rays are bended by the lens, thus covering longer tracks compared to an unperturbed light ray, hence the first term in Equation 1.11 which represents the geometrical delay. Moreover, the space-time is also distorted by the lens gravitational potential and a delay also arises from time dilation, hence the second term in Equation 1.11. It is called the Shapiro delay. On the other hand, we also note that $\nabla\tau(\boldsymbol{\theta};\boldsymbol{\beta}) = 0$ is in fact equivalent to the lens equation (1.2). Solving the lens equation for a given lens and source position is thus equivalent to finding stationary points in $\tau(\boldsymbol{\theta}|\boldsymbol{\beta})$. This surface $\tau(\boldsymbol{\theta}|\boldsymbol{\beta})$ is called **the arrival-time surface**, and it is simply the mapping of the scaled excess of light travel time as a function of $\boldsymbol{\theta}$ for a given source position $\boldsymbol{\beta}$. To predict the number of images of a source, one can calculate the arrival-time surface and the images will appear at any maximum, minimum or saddle point of this surface.

The Fermat potential, as stated above, also helps quantifying the time that a light ray takes to travel from the source to the observer. If variations occur in the source, those variations will travel to the observer through different paths, i.e. the different

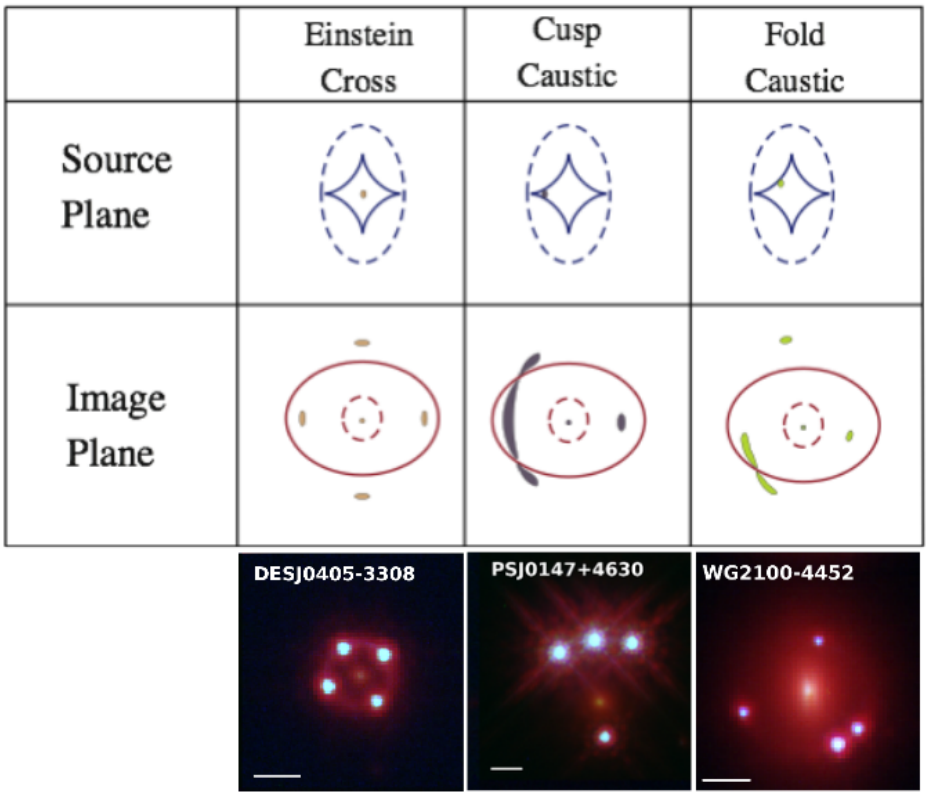

Figure 1.7: Example of quads configurations. © A. Amara, T. Kitching, Schmidt et al. (2022)

Notes. The caustics and the the source position are displayed in the top panels, while the corresponding critical curves and images are drawn in the middle panels. The represented configurations are, from left to right: the cross configuration (source centered in the inner caustic and images in a cross shape); the cusp configuration (source placed close to a cusp of the inner caustic and images positioned as a group of 3 images opposite to the remaining one); the fold configuration (source placed in the fold of the inner caustic and images placed such that two of them are close to each other). Examples of lensing systems with corresponding configurations are shown in the bottom panels. Note that the lensing galaxy covers the fifth image in the latter.

images of the source, and may not be synchronized anymore when arriving at the observer. This difference in time travel is used to constrain the expansion rate of the Universe. Indeed, the **time delay** between two images A and B, at position $\boldsymbol{\theta}_A$ and $\boldsymbol{\theta}_B$ respectively, of the same source of light with intrinsic position $\boldsymbol{\beta}$ is given by:

$$\Delta t_{AB} = \frac{D_{\Delta t}}{c}\left(\tau(\boldsymbol{\theta}_A;\boldsymbol{\beta}) - \tau(\boldsymbol{\theta}_B;\boldsymbol{\beta})\right) , \tag{1.13}$$

where

$$D_{\Delta t} = (1+z_{\mathrm{d}})\frac{D_{\mathrm{d}}D_{\mathrm{s}}}{D_{\mathrm{ds}}} \tag{1.14}$$

is the **time-delay distance**. By modelling the lens system, i.e. constraining the Fermat potential at the images positions, and by measuring the time delays between the images, one can constrain the time-delay distance. As the time-delay distance is inversely proportional to the Hubble constant, constraining $D_{\Delta t}$ allows one to constrain H_0 for a given cosmological model.

Angular diameter distance

In general relativity, using the Friedmann-Lemaître-Robertson-Walker (FLRW) metric, and assuming that the universe is flat (as assumed in the flat ΛCDM), we have:

$$D_A(z_1,z_2) = \frac{1}{1+z_2}\frac{c}{H_0}\int_{z_1}^{z_2}\frac{d\overline{z}}{\sqrt{\Omega_{\mathrm{m},0}(1+\overline{z})^3 + \Omega_{\mathrm{r},0}(1+\overline{z})^4 + \Omega_{\Lambda,0}}} ,$$

where $D_A(z_1,z_2)$ is the angular diameter distance of an object at redshift z_2 observed by an observer located at redshift z_1. $\Omega_{\mathrm{m},0}$, $\Omega_{\mathrm{r},0}$, and $\Omega_{\Lambda,0}$ are respectively the matter, radiation, and vacuum density parameters at our epoch. Note that the term with $\Omega_{\mathrm{r},0}$ is often neglected, as at is believed to be almost null since the radiation density parameter at our epochs is negligible.

To summarize, the strong lensing formalism is built upon general relativity. The light rays of a background source will be deflected by the mass of a foreground object, as the latter deforms the space-time curvature. The object responsible for the deflection is called the lens. One can associate a lensing potential and its derivatives (i.e. deflection angle, convergence, magnification) to the mass of the lens, projected in 2D. With a good observer-lens-source alignment and a massive enough lens, several images of the background source can be observed. A time delay between the images of a variable source is also induced due to the gravitational time dilation and the increased distances to cover because of the deflection. Observing the delays and modelling the lens mass allows one to constrain H_0.

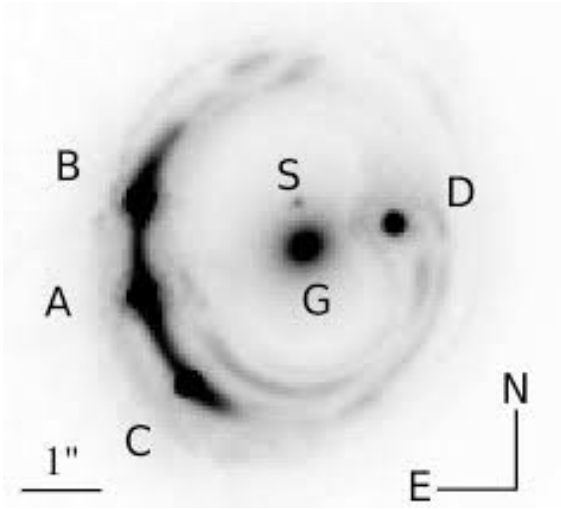

Figure 1.8: Example of an HST image of the lensing system RXJ1131-1231 from Suyu et al. (2014).

Notes. The galaxy G and its satellite S are lensing a source of unknown position and display four images A, B, C, and D in a cusp configuration.

1.2.2 Lensing for time-delay cosmography

Figure 1.8 displays an example of a high-quality HST image, showing the lensing system RXJ1131-1231. To perform a time-delay cosmography analysis on such lensing system, several ingredients are needed. First, a modelling of the lensing system has to be performed. It consists in finding the best light profiles for the source and lens, and the mass profile for the lens to match the imaging data of the lensing system, i.e. Figure 1.8 for instance. In parallel, the kinematic of the lens, i.e. its velocity dispersion, can be measured to independently constrain the modelled mass profile. Moreover, the time delays between the lensed images can be simulated for the retrieved best model assuming a given cosmology. By observing the true time delays, one can compare the truth to the model, and find the cosmological parameters that best match the observations. However, the environment of the lens, i.e. any mass on the line-of-sight, can alter the observables and accounting for them as an external convergence is also needed to accurately constrain the cosmology. Four major parts of the analysis can thus be identified: the modelling of the lens, the observation of the kinematics of the lens, the measurement of the time delay between the images, and the study of the environment. The following paragraphs will discuss each part more precisely.

The **modelling of the lens** requires assumptions on the source light profile, the

lens mass profile, and the lens light profile. The light of the source is generally divided into two components: the light of the quasar, modelled as a point-source, and the light of the host galaxy, often considered as following a Sérsic profile. With high-quality images, details of the source, such as star forming regions, can be identified and various more complex light models can be applied. Having a high signal-to-noise ratio in the arcs, i.e. clear lensed extended features of the source, is essential to accurately constrain the mass model as the arcs provide numerous data points, i.e. pixels, probing a range of angles and radii around the quasar images. The light of the lensing galaxy is generically modelled as Sérsic or Chameleon profiles. The latter is particularly useful when used for both the mass and the light of the lensing galaxy as its lensing potential form is easily computed. The mass of the lens can be described by a single or a combination of mass profiles. Section 1.3.1 will describe the most used family of mass models, the power laws. A generic modelling code repetitively generates fake images of the lens system based on a set of parameters for a given set of mass and light models. The fake images are compared to the true image and the iterative process optimizes the parameters to maximize the likelihood. Note that having an accurate instrumental PSF is fundamental to retrieve an accurate result. When convergence is reached, the best model can be extracted and used for time-delay cosmography.

Convergence and degeneracies

Maximizing the likelihood seems conceptually easy: by comprehensively exploring the parameter space, one should find the set of parameters which best fits the data. However, the likelihood in lensing is generally multi-modal and the parameter space can easily have 40 dimensions. Choosing a well-though method to explore the parameter space is thus crucial to efficiently find the maximum (or maxima) in a limited amount of time (see among others Shajib et al. 2019; Schmidt et al. 2022, Ertl et al. in prep.). When a solution is found, its validity and physical interpretation is still debatable as a modelling solution is often degenerated (1) with other solutions for the same model and (2) with different solutions for different models. One famous degeneracy is the mass sheet degeneracy (MSD) which relates different mass models that are away from each other by a multiplicative factor λ and a mass sheet of constant convergence $(1-\lambda)$:

$$\kappa_\lambda(\theta) = \lambda\kappa(\theta) + (1-\lambda). \tag{1.15}$$

Under such degeneracy, the imaging observables remain the same but the source size and position are re-scaled by a factor λ, and the Hubble constant is similarly scaled while leaving the time-delay ratios invariant (Schneider & Sluse 2013). While this degeneracy can be mitigated thanks to the kinematics of the lens, other degeneracies can also appear. Chapters 3&4&5 will explore more specific situations where the true and modelled mass profiles are different. [a]

[a] Aside, I am also involved in a project whose goal is to explore the degeneracy between the source light patterns and the lens mass patterns by using different modelling codes having different degrees of freedom in the source light and lens mass reconstruction.

Studying the **kinematic of the lens** can be done thanks to precise spectroscopy of the lens. One generally aims at measuring the velocity dispersion of the lensing galaxy. Indeed, the velocity dispersion of an elliptical galaxy can also be simulated for a given mass and light model, assuming specific symmetry, stellar orbit parameters, and de-projection procedure. By comparing the measured velocity dispersion to the one simulated with the solution of the modelling procedure, one can assess the credibility of the mass model and consequently break degeneracies. In current time-delay lensing analyses, this comparison is performed in post-processing [6], i.e. after the modelling. The spherical Jeans model is the most used model to link the gravitational potential to the associated velocity dispersion (Birrer et al. 2020; Shajib et al.

[6] I am currently involved in a project which aims at implementing a joint modelling of the kinematic of the lens at the same time as the imaging data.

2022). But, as its name indicates, this model assumes a spherical symmetry and may become outdated as resolved kinematic data of lensing galaxies start to be available.

To enable measurements of the **time delays**, one has to observe the different images of the same background source. Quasars are particularly suitable sources thanks to their variability, their intense luminosity and their limited spatial extension. Indeed, the lensed images of a quasar are point-like, modulo the PSF, very bright, and hopefully vary with time. The monitoring of the lensed images, which can take up to several years, can thus be done with ground-base telescopes. Once the time series of each lensed image are extracted, one can measure the time shift between the different curves despite the presence of micro-lensing (Millon et al. 2020b,a), and use it to retrieve the time-delay distance $D_{\Delta t}$ necessary to link the observed time delay to the difference of Fermat potential (see Equation (1.13)).

The study of the **environment of the lens** is performed thanks to wide field images that capture the surroundings of the lensing system. The effect of large scale structures is generally twofold: they induce a shear, which is taken into account in the modelling procedure, and a convergence, which needs to be considered as it affects the time-delay distance. By obtaining the position and redshift of all the galaxies in the environment, one can compare the density of the field to simulated line-of-sights to assess if the environment is globally over-dense or under-dense. The time-delay distance, used to assess H_0, can thus be adapted with

$$D'_{\Delta t} = (1 - \kappa_{\text{ext}}) D_{\Delta t}, \tag{1.16}$$

κ_{ext} being the external convergence due to line-of-sight structures. In practice, one will count and weight the galaxies within an aperture (typically of the order of a hundred of arcseconds) and compare this density to the one of simulated line-of-sights using, for instance, the Millenium Simulation (Springel et al. 2005). Each simulated line-of-sight is associated to a convergence and shear. One can choose to only use the weighted number count as the restraining factor to find plausible equivalent line-of-sights, or to use both the modelled shear and the weighted number count to constrain the sample of equivalent line-of-sights. Chapter 6 will further discuss the use of shear to constrain the environment.

By combining the four parts of the analysis described above, one can in principle retrieve an accurate value of H_0 based on a single lensing system, with around 5 to 10 percent uncertainty. Moreover, combining the results from several lenses constrains the inference even more, and allows one to reach a precision of 2.4% (see Wong et al. 2020). Nevertheless, Birrer et al. (2020) recently suggested a new hierarchical framework to better constrain the MSD at a population level, which was before only mitigated by the use of two different mass models and the velocity dispersion of each lens. This methodology uses a sample of non-time-delay lenses to constrain the shape of the mass of lenses at a population level, provided that these lenses have similar mass

profiles as the ones with time delays. In this context, investigating the characteristics of the lensing galaxies becomes even more interesting.

1.3 Massive elliptical galaxies

Massive elliptical galaxies preponderate in the sample of observed lensing galaxy. Indeed, only the most massive galaxies ($M \gtrsim 10^{11} M_\odot$) can deflect the light of a background source with sufficient amplitude to create multiple images which are spatially resolved with nowadays telescopes. Understanding the formation and evolution of elliptical galaxies should consequently help moving a step forward in lensing analyses.

It was originally thought that elliptical galaxies were the progenitors of the spiral galaxies, with a smooth evolution with increasing ellipticity from one to the other. They were accordingly named "early-type" for the elliptical galaxies and "late-type" for the spiral ones. Such representation of a linear evolution from elliptical to spiral galaxies is now outdated but the historical naming convention remains. It is now acknowledged that early-type galaxies are divided into two disjoint categories: the fast and slow rotators (see Figure 1.9). The fast rotators, which also include lenticular galaxies, are similar to spiral galaxies but are dominated by the bulge-like component, with a possible embedded disk. The slow rotators are separated from this sequence and are generally rounder, triaxial and display a cored light profile in their center. Some characteristics of elliptical galaxies are common to both types of early-type galaxies, while others are uncoupled. Here is a description of a few key characteristics of early-type galaxies.

Composition The elliptical galaxies are generally characterized by an old stellar population, rather homogeneous in age and metallicity (Pasquali et al. 2006). Early-type galaxies are usually poor in dust, gas, and star formation. However, blue clumps can sometimes be observed in their light, tracing either young star clusters or dwarf galaxies (Pasquali et al. 2006). Some elliptical galaxies also possess X-ray emitting gas while others do not. Finally, several elliptical galaxies display an α-enhancement.

Isophotal Shape The 2D shape of the isophotes of early-type galaxies is generally conformal ellipses, but deviations from pure elliptical symmetry can be observed (see Figure 1.10). The most visible deviation is the octopolar one: the isophotes of elliptical galaxies can sometimes display discy or boxy shapes (see Chapter 4 and panels (c) & (d) in Figure 1.10). Such deviations are not projection effects (Bender et al. 1989; Chaware et al. 2014) but it can not be ruled out that the intensity of the effect could be enhanced depending on the inclination (Hao et al. 2006; Chaware et al. 2014). The innermost region and outermost regions of a same galaxy can also display different shapes (one region being boxy, the other being discy) (Chaware et al. 2014).

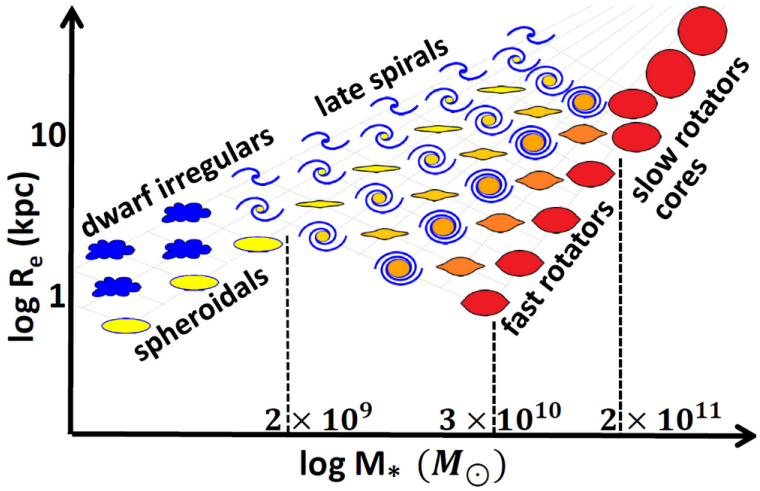

Figure 1.9: Distribution of galaxies on a mass-size diagram from Cappellari (2016).

Notes. $2\times10^{11}M_\odot$ is the critical mass at which the early-type galaxy population switches from a population dominated by fast rotators to one including mainly slow rotators.

The stronger the ellipticity, the stronger the deviation form pure ellipticity. The shape of the isophotes of elliptcical galaxies also seems to be correlated with the other properties of the galaxies: the fast rotators are likely to display discy isophotes, while the slow rotators will exhibit boxy contours. Another deviation in the shape of early-type galaxies which can be pointed out is the evolution of position angle and ellipticity of the isophotes with galacto-centric distance (see among others Bender et al. 1989; Hao et al. 2006; Kormendy et al. 2009) (see Chapter 5 and panel (b) in Figure 1.10). The gradient of ellipticity is stronger for more elliptical early-type galaxies but it is not correlated with other properties of the galaxy or the environment (Hao et al. 2006).

Light Profile The luminosity of elliptical galaxies is generally well modelled by Sérsic profiles. A general form of this profile is:

$$I(R) = I_{\rm eff}\exp\left\{-b_n\left[\left(\frac{R}{R_{\rm eff}}\right)^{1/n}-1\right]\right\}, \tag{1.17}$$

with $I(R)$ the intensity at radius R, $I_{\rm eff}$ the intensity at the half-light radius $R_{\rm eff}$, and b_n the scaling factor chosen such that $R_{\rm eff}$ is the half-light radius for a given Sérsic index n. The most luminous elliptical galaxies ($M_V \lesssim -21.5$) generally have Sérsic index $n \gtrsim 4$, while the "regular" elliptical galaxies ($M_V \gtrsim -21.5$) tend to display light profiles

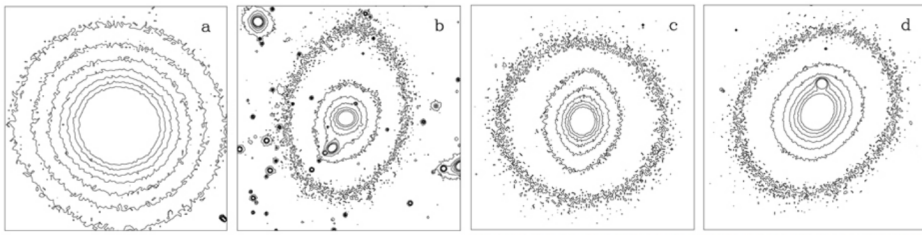

Figure 1.10: Examples of deviations from pure elliptical symmetry. © R. de Jong

Notes. From left to right: (a) Conformal isophotal contours ; (b) Twist and gradient of ellipticity in the isophotal contours ; (c) Discy isophotes ; (d) Boxy isophotes.

with Sérsic index $n \lesssim 3$ (Caon et al. 1993; Cappellari 2016). The giant and luminous elliptical galaxies can also display a core in their light profile, while the regular ones do not. The latter can in fact even display extra-light at the centre of their profiles (Kormendy et al. 2009). We will later summarize the correlations between the light profiles shapes and the other characteristics of the galaxy.

Formation The formation process of elliptical galaxies is not directly observable but studying the properties of the galaxies helped to differentiate two categories of galaxies created through two different processes. The brightest, cored, boxy galaxies are remnants of dry-mergers, while the core-less, discy, and less luminous ellipticals are likely to be remnants of wet-mergers (Kormendy et al. 2009). Khochfar & Burkert (2005) even sub-divided each category: boxy elliptical galaxies can arise from the merging of two bulge-dominated galaxies but also from merging of equal-mass disc galaxies, while discy ellipticals can emerge from unequal-mass mergers (of an elliptical and a disc galaxy for instance) or from a merger remnant which accreted gas and formed a secondary discy component.

Age Most early-type galaxies have been formed at redshifts 2~5 (Pasquali et al. 2006). Moreover, the morphologies of the local elliptical galaxies are similar to the ones of the galaxies at redshift 1 (Pasquali et al. 2006), which should be a signature of the absence of major merging events in the mean time.

Rotation The rotation of elliptical galaxies is diverse: a galaxy can display no rotation, or a complex one, or display a kinematically distinct core (KDC), or feature a counter-rotating disc, or display a regular disk-like rotation (see Figure 1.11). Based on this diversity, two categories of elliptical galaxies can be distinguished: the fast versus slow rotators, which roughly corresponds to regular vs non-regular rotators. In-

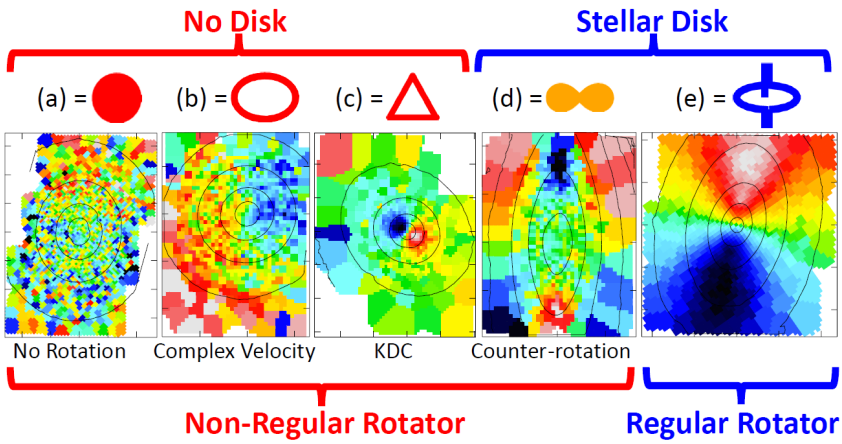

Figure 1.11: Variety of rotation patterns in early-type galaxies from Cappellari (2016).

Notes. From left to right, a galaxy can display no rotation (a), or a complex rotation pattern (b), or display a kinematically distinct core (KDC) (c), or feature a counter-rotating disc (d), or display a regular disk-like rotation (e).

tegral field spectroscopy allowed Cappellari (2016) to assess that these two categories are distinct; there is no smooth transition between them.

The distinction between fast and slow rotators can be made in the (λ_R, ϵ) plane (see Figure 1.12). Similarly to the V/σ, which compares the ordered velocity V to the random one σ (i.e. stellar velocity dispersion), λ_R is a ratio of angular momentum and $V_{\rm rms}$ (more details can be found in Emsellem et al. 2011; Cappellari 2016).

The fast rotators generally display alignment between their kinematics and photometry, which is consistent with the hypothesis that fast rotators are oblate and display discs (Fogarty et al. 2015; Cappellari 2016). The slow rotators are less likely to be aligned, and are thought to be triaxial (Krajnović et al. 2011; Fogarty et al. 2015; Cappellari 2016).

Environment Elliptical galaxies in the Universe can form groups and clusters or be more isolated. The fast rotators are distributed in the Universe like the spiral galaxies. The slow rotators, on the other hand, are more likely to be found in locally dense environment and at centers of clusters and groups (Hao et al. 2006; Cappellari 2016).

As implied in the above descriptions, two distinct categories of elliptical galaxies arise from their different properties. Table 1.1 summarizes the differences. More

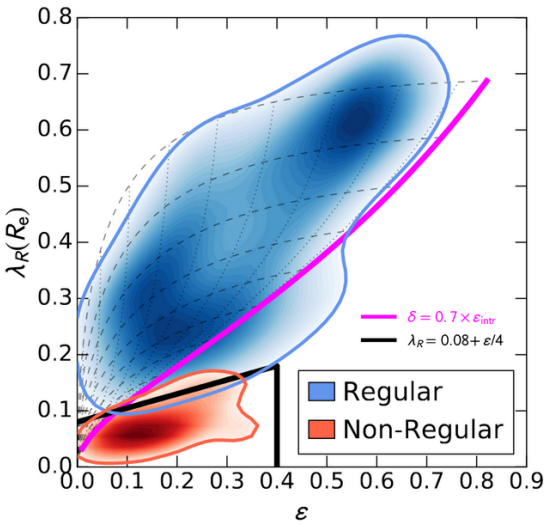

Figure 1.12: Dichotomy in rotation patterns in early-type galaxies from Cappellari (2016).

Notes. ϵ is the apparent ellipticity of the galaxy, and $\lambda_R(R_e)$ is a quantity representing a scaled rotation velocity within the effective radius. The black and purple lines are empirical separations between the slow rotators and the fast rotators: the purple line is an empirical limit of regular rotator population based on the anisotropy δ and deprojected intrinsic ellipticity $\epsilon_{\rm intr}$, while the black line is a refinement of the regular versus non-regular separation in the (λ_R, ϵ) plane, which better represents the dichotomy. The dotted lines are the purple relation assuming different inclinations (the purple line corresponding to being edge-on), and the dashed lines are contours of constant anisotropy.

broadly, different elliptical galaxies can display different features in their light, rotation, and mass profiles. Such differences are generally not taken into account in lensing, and generic mass models for early-type galaxies are used. With the current knowledge of elliptical galaxies and the advent in more precise imaging and resolved kinematics for lensing systems, identifying detailed characteristics of a lensing galaxy and using this information as a prior in the modelling becomes achievable.

1.3.1 Lens mass models

A lot of different mass profiles have been introduced in the literature and used to describe lensing galaxies. Nevertheless, the mass distribution of lensing galaxies is generally modelled with the following main family of mass models: the power-law mass profile and the composite mass profile, with a combination of a baryonic and a

Properties	Characteristics	
Brightness	Bright, $M_V \lesssim -21.5$	Normal, $M_V \gtrsim -21.5$
Mass	$M \gtrsim 2 \times 10^{11} \mathrm{M}_\odot$	$M \lesssim 2 \times 10^{11} \mathrm{M}_\odot$
Isophotal shape	Boxy	Discy
3D shape	Triaxial	Oblate
Ellipticity	Rounder	Flatter
Light profile	Cored, $n_{\mathrm{Sérsic}} \gtrsim 4$	Coreless, $n_{\mathrm{Sérsic}} \lesssim 3$
Star content	Old, α-element enhanced	Old and younger, not α-enhanced
X-Ray emitting gas	Yes	Rarely
Formation	Equal-mass merger of discy galaxies or major merger of early-type galaxies (dry-merger)	Unequal-mass merger or late gas infall (wet-merger)
Rotation	Slow rotators	Fast rotators
Environment	Dense environment, centre of clusters and groups	Less concentrated environment

Table 1.1: Properties of the two main categories of elliptical galaxies.

dark matter component. The power law is the simplest yet appropriate family of mass models. The two-component mass models are more advanced: more radial freedom is allowed in the model and it is common to partially link the lens-light model to the baryonic mass model for physical reasons. For the analysis of specific lenses, both types of models are generally explored and compared (see e.g. Birrer et al. 2019; Rusu et al. 2020; Shajib et al. 2022). Nevertheless, the simple power-law model is often preferred for analysing or simulating a population of lenses (see e.g. Shajib et al. 2019; Park et al. 2021). It is also the usual starting point of perturbative reconstruction of pixelated lens potential or lens mass (see e.g. Suyu et al. 2009; Barrera et al. 2021). Interestingly, Suyu et al. (2009) found that the pixelated deviation from the analytical power-law ellipsoid needed to model the lens system B1608+656, observed with the HST, was of the order of 2%. This result, combined to the fact that power-law profiles are generally sufficient to correctly model the different lensing systems, supported the use of power laws as ground-base model.

The most generic form of the convergence of a **power-law** mass model is the Soft-

ened Power-law Elliptical Mass Distribution (SPEMD), and it is given by:

$$\kappa_{\rm SPEMD}(x,y) = \frac{3-\gamma}{2}\left(\frac{b}{\sqrt{qx^2+y^2/q+s^2}}\right)^{\gamma-1} \tag{1.18}$$

where γ is the power-law slope, b is the scaling factor[7], q is the axis ratio, and s is the core radius. The ellipsoid has its major-axis aligned with the x-axis in this formula. This equation comprehends the whole power-law family of mass model, but sub-categories of this generic power-law model are also used in lensing. First, fixing the power-law slope to 2 is common practice and in such a case, the model is called **isothermal**. Indeed, the 3D density distribution is proportional to r^{-2} and the Keplerian rotation velocities are constant (i.e. flat rotation curves) (Keeton 2001). Most lensing systems are well fitted by such a model. Secondly, even if the SPEMD model yields a core of size s, it is usual in lensing to use **singular** profiles instead of cored ones, i.e. profiles that will diverge at $r \to 0$. In lensing, the presence or absence of the core will mainly impact the brightness of the source image at the center, i.e. the fifth image for quads. As such image is blended with lens light in real cases, it is difficult to assess the cored nature of lensing galaxy masses through lensing[8]. Thirdly, while elliptical galaxies often display elliptical shapes, it can be easier to model them as spheres to narrow down the parameter space, especially if the galaxy is not well resolved or is just a satellite to the main lensing galaxy. In such cases, q is set to one and the mass profiles display **spherical** symmetry in 3D and circular symmetry in projection. Table 1.2 summarizes the main power-law model names which are used in lensing, as function of the different characteristics.

[7]The scaling factor b is equal to the intermediate-axis Einstein radius if the power-law is core-less, i.e. $s = 0$. Otherwise, we can find an analytical approximation for small core radius ($s < 0.1b$): $\theta_{\rm E,i-a} \simeq b - s^{3-\gamma} q^{(\gamma-1)/2}$.

[8]Note that hydro-dynamical simulations such as EAGLE (Evolution and Assembly of GaLaxies and their Environments Crain et al. 2015; Schaye et al. 2015) or Illustris (Genel et al. 2014; Vogelsberger et al. 2014b) often feature such cored profiles in the mass of early-type galaxies. However, such features are mainly due to finite resolution and smoothing of the simulations and the physical nature of the core can not be assessed.

Characteristics			Model name
Isothermal	Singular	Spherical	
No	No	No	Softened Power-law Elliptical Mass Distribution (SPEMD)
No	Yes	No	Power-law Elliptical Mass Distribution (PEMD)
Yes	No	No	Non-singular Isothermal Ellipsoid (NIE)
Yes	No	Yes	Non-singular Isothermal Sphere (NIS)
Yes	Yes	No	Singular Isothermal Ellipsoid (SIE)
Yes	Yes	Yes	Singular Isothermal Sphere (SIS)

Table 1.2: Common names of power-law models used in lensing.

Notes. Some combinations of characteristics, such as a "non-singular non-isothermal spherical" mass profile, do not specifically have a name in lensing analysis, and are thus not introduced in this table. The Softened Power-law Elliptical Potential (SPEP) model also exists but is not introduced in this table. It is similar to the SPEMD (non-isothermal, non-singular, non-spherical) except that the ellipticity is introduced in the lensing potential for the SPEP, instead of being introduced in the mass, as in the SPEMD. Having ellipticity introduced in the lensing potential makes the calculations of the lensing quantities easier. However, the mass distribution of such profile, derived through Equation 1.8, does not display elliptical isodensity contours and even exhibits a peanut (or a donut) shape for high ellipticities (Kassiola & Kovner 1993). Such model is nowadays slightly disfavoured since modelling codes can handle the SPEMD which is more physically motivated.

Einstein radius

The **Einstein radius** is generally defined as the radius encompassing a mean convergence equal to 1.

When the mass profile displays a circular symmetry, such definition is unambiguous. The Einstein radius can even be a parameter, θ_E, of the profile. The convergence of elliptical mass profiles is often a deformed version of its circular equivalent. In such cases, the quoted parameter θ_E often represents the size (semi-major, intermediate[a], or semi-minor axis) of the ellipse that encompasses a mean convergence equal to 1. The intermediate-axis of the ellipse, following the isodensity contours, enclosing a given mean convergence of 1 is not equal to the radius of a circle enclosing the same quantity. The latter is thus referred to as the effective Einstein radius $\theta_{\mathrm{E,eff}}$.

[a] Intermediate-axis being geometrical mean of the semi-minor and semi-major axis of an ellipse $r_{\mathrm{i-a}} = \sqrt{r_{\mathrm{major}} \times r_{\mathrm{minor}}}$

Aside from the mass distribution of the main lensing galaxy, another model one needs to consider in lensing is the **shear**[9]. It can represent the stretching of the lensing potential due to nearby galaxies in the lens plane. It can also be used to account for stretching due to galaxies or clusters more generally in the line-of-sight, i.e. impacting the light rays travelling to us at any point of their path. The lensing potential associated to this model is:

$$\psi_{\text{shear}}(r,\phi) = \frac{1}{2}\gamma_{\text{ext}} r^2 \cos\left(2(\phi-\phi_{\text{ext}})\right) \quad \text{in polar coordinates} \tag{1.19}$$

$$\text{or } \psi_{\text{shear}}(x,y) = \frac{1}{2}\left(\gamma_1 x^2 + 2\gamma_2 xy - \gamma_1 y^2\right) \quad \text{in cartesian coordinates.} \tag{1.20}$$

with $\gamma_1 = \gamma_{\text{ext}}\cos(2\phi_{\text{ext}})$, and $\gamma_2 = \gamma_{\text{ext}}\sin(2\phi_{\text{ext}})$. γ_{ext} is the strength of the shear and ϕ_{ext} is its orientation[10]. Such potential displays a saddle shape. The convergence associated to this model is null, no mass is associated to it.

As discussed earlier in Section 1.3, the shape of elliptical galaxies is more complex than a simple ellipsoid. The isophotes do not necessarily display conformal ellipses and the mass of the lensing galaxies is consequently expected to feature similar degrees of complexity. Therefore, the power-law models + shear may not fully render the complexity of the mass profiles of lensing galaxies, even if they are generally sufficient to model observed lensing systems. Chapter 4 will investigate the impact of the octupolar momentum (i.e. boxyness and discyness) on the lensed images, and Chapter 5 will discuss the effect of twist and ellipticity gradient in lensing analyses.

1.4 Thesis structure

This thesis aims at using simulated lensed systems to investigate the accuracy one can achieve on the cosmological inference from lensing analyses. More precisely, I focused on investigating the impact of the presence of azimuthal structures in lensing galaxies when the latter are modelled as conformal ellipsoids. I first devised a workflow to simulate lensing systems, which is described in Chapter 2. One can choose to either use mass maps or analytical profiles to describe the mass of the lens. One impact of using finite mass maps to create mock lensing galaxies is described in Chapter 3. To further study the impact of azimuthal structures in lensing, I used analytical profiles. The study of the impact of the presence of boxyness and discyness in lensing galaxies is shown in Chapter 4. In Chapter 5, the impact of another kind of lens mass features is studied: the twists and ellipticity gradient of the isodensity contours. Chapter 6 summarizes the findings and discusses their impact in modern time-delay cosmography context.

[9] Also called external shear, as it represents stretching triggered by components exterior to the main lens ; in opposition to the internal shear which is a stretching due to the mass distribution of the main lensing galaxy.

[10] The shear orientation is the direction in which the image of the source will be stretched. It is perpendicular to the direction of a mass distribution that would create it.

CHAPTER 2

SIMULATING LENSING SYSTEMS

This chapter outlines the procedure we have developed to simulate lensing systems. Section 2.1 describes the different ingredients needed to construct mock lensing systems. Section 2.2 explains more precisely the practical input and output of the developed framework.

2.1 The ingredients

A common building block of my work consists in simulating lensing systems, i.e. creating mock images of strongly lensed sources. Indeed, simulating lensing systems allows one to control the input parameters and cosmology. After modelling with standard techniques, the output can be compared to the "truth" to assess the accuracy and the precision of the result.

As introduced in Chapter 1, simulating realistic mock observations of lensing systems with time-delays requires different ingredients: a light source, a lens (mass and light), a cosmology, and an instrumental setting. Indeed, the light source is lensed by the mass of the lens, which creates images and arcs as seen by an observer. The lens light can be superposed on the light from the source. All the light should be convolved by a PSF, and noise must be introduced to create realistic images. Finally, a cosmology has to be assumed to simulate the time delays between the images. The following paragraphs will detail each element needed for the simulation.

To mimic realistic time-delay lenses and enable cosmological inferences, the sim-

ulated systems must include a quasar-like **source**, which is embedded in a host galaxy (see Section 1.2.2 for discussion on the utility of having the light of both the quasar and its host galaxy). The quasars are simulated (and later modelled) as point-sources (PS). Their intense luminosity yields the lensed images to display a very bright PSF pattern. The quasar host galaxies are simulated with simple Sérsic profiles. The source of light, PS + Sérsic, is purposely kept simple to focus on other aspects of the lensing, i.e. the complexity of the lens mass.

In this thesis, different **lens mass** profiles were used to investigate different questions. The impact of using truncated mass maps as lensing mass is studied in Chapter 3. For such purpose, the mass profile is a pixelated 2D map of the unit-less convergence of a NIE mass profile (see Section 1.3.1 for power-law profiles description). With 2D convergence maps, the lensing potential and deflection angles (see Equation 1.7, and 1.4) are calculated with Fast Fourier Transform (FFT) methods, and the second derivatives are then determined by numerically deriving the deflection. When needed, interpolation between the pixels of the created maps is used. In Chapter 4, the impact of the not-modelled presence of boxyness and discyness in lensing galaxies is investigated. Therefore, the mass profiles used are SIEs with analytical multipolar deformations of order 4 and external shear. Such profiles are analytical and virtually extend to infinity. In Chapter 5, twists and ellipticity gradients in lensing galaxies are examined. To create mass profiles that display complex profiles of azimuthal variations, a mass profile constituted of numerous superposed low-mass profiles is used. More precisely, this profile is built as an addition of multiple elliptical slices, each slice displaying a given size, constant surface-density, ellipticity and orientation. The resulting total mass profile resembles a wedding cake with around 60 layers. While the mass exhibits a step-like profile, the lensing quantities (potential, deflection, etc) associated to each slice are known analytically and present a continuous form. The resulting lensing quantities, obtained by summing up the ones of each slice, are thus analytical and virtually extend to infinity as well. The mathematical details of each lens mass profile introduced in this thesis will be detailed in the relevant chapters.

Regarding the **lens light**, a transparent lens is always chosen in this thesis to avoid a blending of the lens and source light. Indeed, the mass of the lens impacts the shape of the light of the lensed source, and a confusion between lens or source light would prevent a thorough study of the impact of mass peculiarities on the light from the source.

As Chapter 3 only serves as warning about spurious artificial shear presence in simulations using truncated mass maps, a realistic **instrumental set-up** is not needed there. We thus chose to use a Gaussian PSF and no noise. On the other hand, realistic populations of observations of lensing systems are emulated in Chapters 4 & 5: the goal is to quantify the realistic impact of deviations from pure ellipticity in current lensing analyses. A PSF typical of the HST with the WFC3 camera in the F160W band is thus adopted, and noise specifications typical for observations of gravitational lenses

with this camera are used.

The input **cosmology** needed to calculate time-delays is chosen to be a standard flat ΛCDM. The cosmological parameters are specified in each chapter. Chapter 3 compares its results with the one from Mukherjee et al. (2018) in which a specific cosmology ($\Omega_\Lambda = 0.693$, $\Omega_m = 0.307$, and $H_0 = 67.77\ \mathrm{km\,s^{-1}\,Mpc^{-1}}$) is adopted. We consistently used the same cosmology. A more neutral set of cosmological parameters ($\Omega_m = 0.3$, $\Omega_\Lambda = 0.7$, and $H_0 = 70\ \mathrm{km\,s^{-1}\,Mpc^{-1}}$) is adopted in Chapters 4 & 5. Those values are neither based on the "early", nor on the "late" Universe measurements (see Section 1.1 for discussion of the different measurements). This choice is arbitrary and does not bias our analysis.

For a given set of cosmological parameters, the theoretical time delays at the images positions are calculated during the simulation and it is assumed that one can observe them and retrieve the true values within a given uncertainty. This uncertainty is assumed to be 2% of the delay with a minimum value of 1 day. A more realistic simulation of the time delays would include a emulation of time series with intrinsic variability of the quasar, micro-lensing, etc. However, the time-dependent level of simulation is not needed in this thesis as our focus is on the mass of the lensing galaxy and not on the time-delay measurements.

2.2 In practice

To create several simulated lens systems efficiently, a framework was developed in Python, in which the strong lensing calculations are carried out through the `lenstronomy` software[1].

Lenstronomy

The `lenstronomy` software is an object-oriented Python package which allows one to simulate as well as model complex lensing systems (Birrer et al. 2015; Birrer & Amara 2018; Birrer et al. 2021).

To develop cutting edge simulations for this work, I implemented new mass models in the software, such as 'ElliSLICE' and 'Multipole'.

A version of this framework designed to create mock images in which the lensing galaxy displays multipolar deformations can be found at cells `In [3]` & `In [4]` of the notebook[2] available at `https://github.com/TDCOSMO/TD_data_public/`

[1] `https://github.com/sibirrer/lenstronomy`

[2] The complete `Jupyter` notebook shows how to create, model, and analyse results of mock images constructed with boxyness/discyness in the lensing galaxy. The three parts of the code are designed to synergise: the information contained in the headers of the simulated mocks is easily read by the modelling

```
#output image
n_pix=131 #output image number of pixels
delta_pix=0.08 #output image pixel size

#lens mass
size=2 #the size of the sample,
angle = np.array([22.*np.pi/180.,22.*np.pi/180.]) #position angle of the SIE
theta_E_lenstro = np.array([2.,2.]) #Einstein radius of the SIE
q = np.array([0.8,0.8]) #axis ratio of the SIE
a_4 = np.array([0.01],0.01) #multipole strength
phi_4 = np.array([45.*np.pi/180.,0.*np.pi/180.]) #position angle of the multipole (w.r.t the SIE main axis):
                                                 #0 is discy; 45 is boxy
shear_strengh = 0.05
shear_angle = 30.*np.pi/180. #w.r.t the SIE main axis

#source light
contrast=1.6 #contrast between host and quasar flux in the source plane
R_sersic=0.1 #source size

#source position
source_pos_list = ['cusp_s','cusp_l','fold','cross'] #'cusp_l','cusp_s','fold','cross','middle_cusp'
                                                     #or a list [x_pos,y_pos]

#fiducial cosmology
H0=70
Om0=0.3
cosmo =  FlatLambdaCDM(H0=H0, Om0=Om0)

#redshifts
z_lens = 0.271
z_source = 2.0

#choose PSF to use
PSF_TDLMC = True
path_psf = os.getcwd()

#specifications for the noise
#those values are typical of WFPC3 camera with F160W filter
mag_zeropoint = 25.96
back_mag = 22.3 #mag/arcsec**2
exp_time = 5400.
exp_num = 1
ron = 21. #https://hst-docs.stsci.edu/hsp/past-hst-proposal-opportunities/the-hubble-space-telescope-primer-
res_in_arcsec=delta_pix

#specifications for the mask to be above a noise threshold
threshold=2.
num_real=150

#place to save your created mocks
path_out = os.getcwd()
name_out = path_out + '/sie_multipole_highsnr_a4001_'
```

Figure 2.1: Example of input needed to simulate mock images of lensing systems.

Notes. This input is meant to create 8 output images, with 2 different lensing galaxies (one boxy, one discy) and 4 different source positions. Note that this input is dedicated to a version of the framework which works with boxyness and discyness. This set-up part is slightly different for other study cases.

blob/master/TDCOSMO_VII/multipole_project_core_code_public.ipynb. An example set-up for the mock creation with this version is shown at Figure 2.1.

In essence, the developed framework inputs the characteristics of:

code to initialise the fit, and the files saved after the modelling procedure contain organised sequences that are used by the analysing part.

- the resulting-image: number of pixels, pixel size;
- the lens mass model: (list of) Einstein radius, (list of) type of mass model and associated parameters, shear specifications;
- the source light: host-galaxy radius, contrast between the host-galaxy brightness and the quasar brightness;
- the source position: either a specific location (in ra-dec), or a random position inside the innermost caustic, or a (list of) specific configuration (fold, cusp on either major or minor axis, and cross);
- the fiducial cosmology: type and associated cosmological parameters;
- the redshifts: source and lens redshifts;
- the PSF: either Gaussian, or pixelated from a file;
- the noise: zero-point of the instrument, read-out-noise, background magnitude, exposure time;
- the mask: number of realisations of the noise used to create the mask, threshold (in $\sigma_{\rm bck}$ unit);
- the file path to save the images.

Note on masks

It is common practice in lensing analyses to use masks on the images in the modelling procedure, to remove flux from unmodelled companions and only focus on the relevant flux from the lensing system.

In the developed framework, an automated mask generation is implemented to mask pixels under a given threshold, compared to the background noise level. In order to have a robust mask, i.e. without random patterns linked to a specific realisation of the noise, the mask creation process is repeated with different noise realisations and a median mask is calculated. Having a coherent method to create masks also ensures retrieving reduced χ^2 consistent between different lensing systems: it avoids an over-representation of non-informative pixels when the lensing system does not span on the whole image.

One particularity of my code is that it was developed to generate populations of lenses. Its design thus allows one to enter lists of specifications, such as a list of Einstein radius, a list of source configurations, a list of mass models, etc.

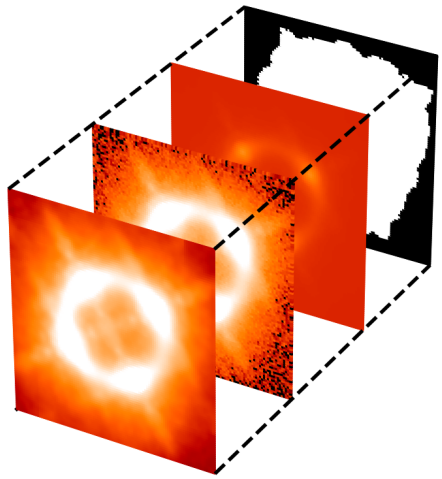

Figure 2.2: Example of data cube created using the developed framework.

Notes. The first slice of the cube is the noise-less image. The associated header contains information about the lens, source, and point-sources characteristics, as well as time-delays with associated uncertainties, pixel size, pixel grid specifications, and PSF characteristics. The second slice is the same image with a given realisation of the noise. No specific header is associated. The third slice is the general noise map from which the noise realisation is drawn. The associated header saves information about the instrument zero point, the background magnitude, the exposure time, the number of exposures, the read-out noise, and the pixel size. The fourth slice is the mask which can be used in the modelling, the threshold and the number of noise realisations used to create the mask are saved in the header.

Once the settings are defined, the code runs and several images are created and saved. Every resulting image of the simulation is output as a cube including four slices: the noise-less image, the image with a noise realisation, the noise map (i.e. σ at each pixel from which a noise realisation is drawn), and the associated mask. An example of such cube is shown at Figure 2.2. Headers are associated to the different slices, keeping track of the input parameters of the framework.

The simulations of lensing systems created with this framework are easily readable, and enable a smooth modelling procedure. As the headers contain the input characteristics, it is possible to automatically read the information and choose to ini-

tialize the modelling accordingly or not. The modelling procedure used in this thesis is standard but was designed to synergise with the simulated lensing systems, hence reducing the need of user input to a few key arguments.

CHAPTER 3

MASS MAP TRUNCATION

This chapter is based on Van de Vyvere et al., *The impact of mass map truncation on strong lensing simulations*, A&A 644, A108 (2020). Sections 3.1 and 3.2 have been condensed compared to the paper as they were partially redundant with Chapter 1. Minor adjustments have also been made to refer to the equations, sections and chapters of the thesis when needed. Section 3.7 has been added to discuss related results in the literature posterior to the publication of Van de Vyvere et al. (2020).

As introduced in Chapter 1, strong gravitational lensing is a powerful tool to measure cosmological parameters and to study galaxy evolution mechanisms. However, quantitative strong lensing studies often require mock observations. A powerful approach used to capture the full complexity of lensing galaxies is to draw them from high resolution, dark matter only or hydro-dynamical simulations. The latter have their own limitations, but the way we use them to emulate mock lensed systems may also introduce significant artefacts. In this chapter, we identify and explore the specific impact of mass truncation on simulations of strong lenses by applying different truncation schemes to a fiducial convergence profile with conformal iso-density contours. Our main finding is that improper mass truncation can introduce undesired artificial shear. The amplitude of the spurious shear depends on the shape and size of the truncation area as well as on the slope and ellipticity of the lens density profile. Due to this effect, the value of H_0 or the shear amplitude inferred by modelling those systems may be biased by several percent. However, we show that the effect becomes negligible provided that the lens projected map extends over at least 50 times

the Einstein radius.

3.1 Introduction

The time-delay cosmology technique, which uses multiply-imaged strongly lensed quasars to measure H_0, offers a poweful means of obtaining the H_0 measurement independent of the local distance ladder (see Section 1.1). The accuracy of this technique relies on our understanding of galaxies and on assumption(s) on their total mass density profiles (e.g. Schneider & Sluse 2013; Birrer et al. 2016, 2020). An important way to validate the technique consists in using simulated lensed systems with various levels of complexity. The Time Delay Lens Modelling Challenge has recently been used to test the accuracy of the H_0 measurement using mock images of strongly lensed quasars with Hubble Space Telescope (HST) image quality (Ding et al. 2021b). Mock gravitationally lensed systems based on 'numerical' galaxies have been used for various other applications, including the validation of analysis frameworks, the training of lens-finding algorithms, and studies of galaxy and dark matter properties (e.g. Xu et al. 2015, 2016; Despali et al. 2018; Mukherjee et al. 2018, 2021; Metcalf et al. 2019; Denzel et al. 2020; Enzi et al. 2020).

The most commonly used technique to create a mock lens system from simulated galaxies is to extract a mass map from a particle-based simulation and use it to calculate lensing quantities (i.e. lensing potential and its first and second derivatives) needed to emulate the gravitationally lensed images. For this purpose, galaxies from high-resolution hydrodynamical simulations, including, for example, EAGLE (Evolution and Assembly of GaLaxies and their Environments, Schaye et al. 2015; Crain et al. 2015) or Illustris (Vogelsberger et al. 2014b,a), have been widely used. Different types of software, such as `lenstronomy` (Birrer & Amara 2018) and `GLAMER` (Gravitational Lensing Simulations with Adaptive Mesh Refinement, Metcalf & Petkova 2014), can handle the inference of lensing quantities from mass maps using fast Fourier transform convolution. Fast Fourier is a commonly used technique to speed up the calculation of lensing quantities, which imply computationally expansive numerical integration, but it remains a demanding procedure (Metcalf & Petkova 2014; Plazas Malagón 2020). One could wonder what mass-map resolution should be used and what size of map is relevant to be sufficiently precise in the mock creation while minimising the computational time. One generally considers that a strongly lensed system is determined by the projected mass inner to the lensed images. This would suggest that a region extending over a few Einstein radii (θ_E) is sufficient for the simulations. However, this consists in effectively ignoring any source of shear, and/or perturbations caused by substructures and/or anisotropy in the mass distributions. Moreover, depending on the symmetry of the problem, cutting the mass distribution at a given radius not only automatically removes the mass beyond that radius, but it may also introduce numerical artefacts that could wrongly be attributed to prop-

erties of the examined lens mass distribution. In this chapter we focus on this latter point and quantify the impact of the shape (and size) of the integration domain on the lensing quantities inference.

We used a smooth analytical cored power-law model, including the isothermal case, with conformal iso-density contours, that is, isocontours all having their axis aligned with each other. We discretised this analytical model on a grid to emulate mass maps from numerical simulations. Such a cored density profile was chosen to mimic galaxy mass profiles from numerical simulations (e.g. Mukherjee et al. 2021; Du et al. 2020). We then truncated those maps and, applying masks spanning a broad range of shapes and extent, used a standard pipeline to create mock lens systems and subsequently modelled them. We find that an 'artificial' shear is created during the mock contruction if the truncation does not follow iso-density contours of the input conformal power-law lens distribution.

In Section 3.2, we explain how a strongly lensed system can be built from a convergence map (i.e. surface mass density normalised by critical density). In Section 3.3, we explain our methodology, and synthesise the results in Section 3.4. We discuss our results and the potential existence of artificial shear in other works in Section 3.5. We finally summarise and conclude in Section 3.6. Section 3.7 was added to further discuss the presence of artificial shear in recent literature posterior to the paper publication.

Calculations presented in this chapter assume the following cosmological parameters $\Omega_\Lambda = 0.693$, $\Omega_\mathrm{m} = 0.307$, and $H_0 = 67.77$ km s^{-1} Mpc^{-1}. This cosmology is the same as the one used in the EAGLE simulations (Schaye et al. 2015; McAlpine et al. 2016).

3.2 From convergence maps to lensed images

We have seen in Section 1.2 that to generate an artificial lens system, we need to know the lensing potential ψ, its first derivatives (the deflection), and its second derivatives. However, the gravitational potential is generally not directly accessible from the numerical simulations, but instead one has access to the surface mass density of the lensing galaxy. Once the source and lens redshifts are chosen, a convergence map can be calculated by normalising the surface mass density by the critical surface density, following Equation (1.5), that is:

$$\kappa \equiv \frac{\Sigma}{\Sigma_{cr}} \quad \text{with} \quad \Sigma_{cr} = \frac{c^2}{4\pi G}\frac{D_s}{D_l D_{ls}}.$$

Fortunately, retrieving the potential and deflections is possible through Equations (1.4) & (1.7), that is:

$$\begin{aligned}\boldsymbol{\alpha}(\boldsymbol{\theta}) &= \frac{1}{\pi}\int_{\mathbb{R}^2} d^2\boldsymbol{\theta}'\,\kappa(\boldsymbol{\theta}')\,\frac{\boldsymbol{\theta}-\boldsymbol{\theta}'}{|\boldsymbol{\theta}-\boldsymbol{\theta}'|^2},\\ \psi(\boldsymbol{\theta}) &= \frac{1}{\pi}\int_{\mathbb{R}^2} d^2\boldsymbol{\theta}'\,\kappa(\boldsymbol{\theta}')\,\ln|\boldsymbol{\theta}-\boldsymbol{\theta}'|.\end{aligned}$$

Those integrations are generally performed by means of convolution using a fast Fourier transform (FFT): They both are a convolution of the κ map with a kernel and $\kappa \otimes kernel = \mathrm{FT}^{-1}(\mathrm{FT}(\kappa) * \mathrm{FT}(kernel))$.

The second derivatives ($\nabla\nabla\psi$) cannot be obtained the same way as the potential and the deflection. This Hessian matrix is thus constructed through a discrete derivation of the deflection $\boldsymbol{\alpha}$.

3.3 Practical specifications

To quantify the impact of the truncation on the lensing observables, we used a known analytical density profile, and we discretised and truncated it at different radii and for different shapes of the truncation region. This has allowed us to compare $\boldsymbol{\alpha}$ and ψ, which were derived numerically (Section 3.2), to their expected values derived analytically. Based on the discretised κ map and inferred lensing quantities, a mock lensed system can also be generated and modelled. This modelling step allowed us to quantify the impact of introduced artefacts on model parameters (e.g. external shear).

We used an analytical non-singular isothermal ellipsoid (NIE, Keeton & Kochanek 1998) mass distribution and discretised its convergence on a grid. The NIE with its major axis oriented along the x-axis has the following analytical expressions for κ, ψ, and $\boldsymbol{\alpha}$:

$$\kappa(x,y) = \frac{b}{2}\left(q^2(s^2+x^2)+y^2\right)^{-1/2} \tag{3.1}$$

$$\psi(x,y) = x\,\alpha_x + y\,\alpha_y - bs\frac{1}{2}\ln\left((\phi+s)^2+(1-q^2)x^2\right) \tag{3.2}$$

$$\alpha_x(x,y) = \frac{\partial\psi(x,y)}{\partial x} = \frac{b}{\sqrt{1-q^2}}\arctan\left(\frac{\sqrt{1-q^2}\,x}{\phi+s}\right) \tag{3.3}$$

$$\alpha_y(x,y) = \frac{\partial\psi(x,y)}{\partial y} = \frac{b}{\sqrt{1-q^2}}\mathrm{arctanh}\left(\frac{\sqrt{1-q^2}\,y}{\phi+q^2 s}\right), \tag{3.4}$$

where b is the scale radius of the convergence (it is equal to the Einstein radius if $s=0$), q is the axis ratio, s is the core radius, and $\phi^2 = q^2(x^2+s^2)+y^2$. To ease the discussion with literature results, we decided to mimic a galaxy with a morphology and redshift similar to a galaxy extracted from an EAGLE hydro-simulation (Schaye

et al. 2015; McAlpine et al. 2016). More specifically, we chose the fiducial parameters $b = 2''$, $s = 0.2''$, $q = 0.7522$, and $PA = -22.5°$. In addition, we set the lens redshift to $z_l = 0.271$.

We used different grid sizes ranging from $16.1'' \times 16.1''$ to $88.5'' \times 88.5''$. To emulate the truncation, we multiplied the κ map with a numerical mask. We considered three different shapes: squared (i.e. taking the κ map as it is); circular (i.e. multiplying with a circular mask whose diameter has the size of the κ map); and elliptical (i.e. multiplying with an elliptical mask whose major-axis has the size of the κ map). We used a grid with a pixel size of $0.025''$. This resolution is half the typical HST sampling for drizzled images, and it corresponds to 0.1 kpc/pixel in the lens plane. This resolution is high enough so as to not impact our tests: Increasing the resolution by a factor of two yields an offset on the image positions by less than 1 milli-arcsecond, and on relative time delays by less than 1 milli-day.

With this set-up, we implemented the numerical integration[1] discussed in Section 3.2. This allowed us to create, within `lenstronomy`, a model internally labeled 'INTERPOL' [2].

In order to create mock lensed images, we needed to chose a source luminosity profile. We decided to emulate a system similar to those used for time-delay cosmography, namely a lensed quasar. More specifically, we considered a source at redshift $z = 2.0$ constituted of a point source and a circular Sérsic host, and we simulated a cross configuration image without lens light. To avoid introducing artefacts with a complex point spread function (PSF), we chose to convolve the image with a Gaussian PSF with FWHM = $0.15''$. The image was constructed on a 161×161 pixels map with a pixel size equal to $0.05''$.

This system (see left panel of Figure 3.1) may then be modelled in a standard way (e.g. Millon et al. 2020c). To avoid introducing biases due to degeneracies between source and lens parameters (e.g. Unruh et al. 2017), we fixed the image positions and the scale radius of the Sérsic source. The only varying parameters during the modelling step are the lensing galaxy parameters, the source centre, and the time delay distance.

In addition, during the modelling, we also introduced an analytical shear model (also introduced at Equation (1.20)), defined as $\boldsymbol{\gamma} \equiv \gamma_1 + i\gamma_2$. The associated lensing

[1] Within `lenstronomy`, the convolution between the κ map and the $kernel$ having twice the κ map size is performed using `scipy.signal.fftconvolve`, a standard FFT convolution algorithm with zero-padding to reach sizes that are a power of 2.

[2] The 'INTERPOL' model works the following way: It takes the maps (potential and its first and second derivatives) and interpolates between the points if needed using a bivariate spline approximation of order 3 over a rectangular mesh as implemented in `scipy`.

quantities are:

$$\psi(x,y) = \frac{1}{2}\left(\gamma_1\, x^2 + 2\,\gamma_2\, xy - \gamma_1\, y^2\right) \quad (3.5)$$

$$\alpha_x(x,y) = \gamma_1\, x + \gamma_2\, y \quad (3.6)$$

$$\alpha_y(x,y) = \gamma_2\, x - \gamma_1\, y \quad (3.7)$$

$$\boldsymbol{M}^{-1} = \begin{pmatrix} 1-\gamma_1 & \gamma_2 \\ \gamma_2 & 1+\gamma_1 \end{pmatrix} \quad (3.8)$$

$$\kappa(x,y) = 0. \quad (3.9)$$

3.4 Results

Figure 3.1 shows our fiducial mock system (see Section 3.3) created with a κ map of $40''$ and a circular mask. One can see that modelling the mock system with our fiducial model leaves substantial residuals (see upper panel of Figure 3.1). In addition, the fitted model parameters, such as the Einstein radius and the ellipticity, are biased compared to the fiducial ones at a level of a few percent. If a shear is fitted in addition to the NIE, we recover the fiducial NIE parameters and a non-zero shear (amplitude of 0.007 in our example). In this case, residuals are compatible with zero (see lower panel of Figure 3.1). Since this modelled shear does not have any physical meaning (it is an artefact created in the mock process), we dub it 'artificial shear'.

By modifying the characteristics of our mock lensed systems, we find that the amplitude of this artificial shear depends on (i) the ellipticity of the lens; (ii) the slope of the density profile; (iii) the size of the masking region; and (iv) the shape of the mask. To characterise this external shear, we varied those parameters in a systematic way. More specifically, we (i) compared the axis ratio of 0.7522 and 0.5590 (i.e. doubling the complex ellipticity module defined as $|e| = \frac{1-q}{1+q}$, where q is the minor/major axis ratio); (ii) varied the slope of the density profile; (iii) varied the size between $16.1''$ and $88.5''$; and (iv) compared the shear dependence on the truncation size for circular and squared masks. The results of these systematic tests are summarised below:

i The artificial shear has an amplitude proportional to the ellipticity module of the input NIE: Doubling the ellipticity module doubles the shear.

ii The amplitude of the shear is found to decrease when the density profile is steeper (see Figure 3.2).

iii The bigger the mask is, the lower the shear is. We empirically find that $\log(\gamma_{\rm art}) = a + b\log(size)$, where $\gamma_{\rm art}$ is the artificial shear amplitude and $size$ is the mask size (see Figure 3.2). A least square regression through this relation for each power-law slope γ' shows that $b \approx (1-\gamma')$, in other words, the artificial shear amplitude decreases as $size^{-(\gamma'-1)}$.

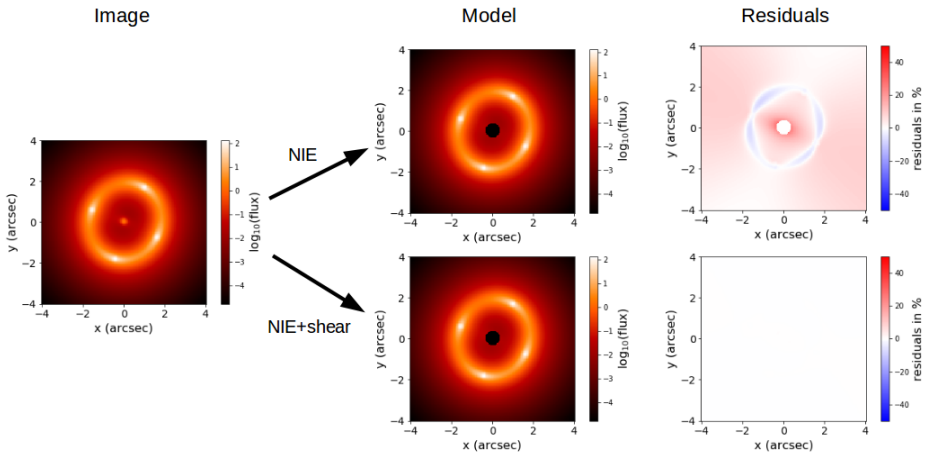

Figure 3.1: Sketch of the method followed to unveil the artificial shear arising due to truncation of the κ map.

Notes. Mock lens system (left) created with a pure NIE κ map truncated with a circular mask of diameter $40''$ – i.e. corresponding to a truncation radius of $10 \times \theta_E$ – and modelled (middle) using an NIE profile (upper) and NIE+shear (bottom) with associated residuals expressed in the percentage of the input flux (right).

iv The dependence of the shear with the size is the same for the square and circular mask (see Figure 3.2).

We also note the following properties of the artificial shear:

- The artificial shear combines vectorialy with a true external shear: $\boldsymbol{\gamma}_{\rm tot} = \boldsymbol{\gamma}_{\rm art} + \boldsymbol{\gamma}_{\rm real}$.
- Using the mock time-delays as an additional constraint in the likelihood used in lens modelling does not modify the fitting results.

In all the cases shown, not accounting for the shear in the modelling yields a biased H_0 value. For our fiducial NIE with a mask size of $40''$, that is, truncation at $10 \times \theta_E$, the bias is typically 4-5% depending on the mask shape. This bias can decrease to 2% with a mask of $80''$. There is, however, no bias when the shear is included in the model.

Finally, if an elliptical mask, which has an ellipticity module and position angle identical to one of the underlying NIE, is used instead of a squared or circular truncation, no artificial shear is produced. This is true even for small mask sizes (e.g. size = $10''$).

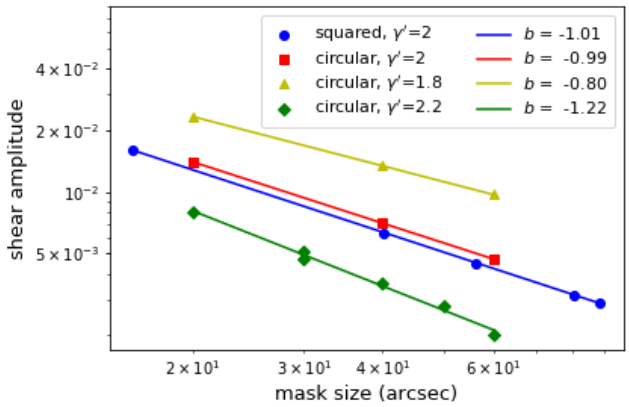

Figure 3.2: Artificial shear amplitude as a function of the mask size for a given ellipticity module $|e| = 0.14$.

Notes. The different markers are for different truncation shapes (circular or squared) and for different slopes of the input cored power-law model γ'. The solid lines represent the logarithmic linear fits ($\log(y) = a + b\log(x)$). The best-fit values of the slope b are written in the legend.

3.5 Discussion

The previous section demonstrates that to first order, the lensed images are sheared when the truncated κ region considered to calculate $\boldsymbol{\alpha}$ and ψ is small and does not follow an iso-density contour. Specifically, a quadrupole (or higher order) contribution, which arises from mass beyond the last complete iso-density contour but is enclosed within the truncation area, is artificially added in the calculation of $\boldsymbol{\alpha}$ and ψ, hence producing an artificial shear.

We have shown numerically that this 'artificial shear' is effectively a shear term by calculating the lensing quantities associated to a convergence map $\Delta\kappa = \kappa_{mask} - \kappa_{iso}$, that is to say resulting from the difference between a truncated NIE and the same NIE truncated following an iso-density contour. Figure 3.3 shows that the deflection created with such a $\Delta\kappa$ map is identical to the one produced by a shear. In the case of the squared mask, the deflection created by $\Delta\kappa$ is only approximately the one of a shear in the region where lensed images are located (see Figure 3.4) due to the contribution of higher order terms to the deflection.

We have seen that artificial shear could remain unnoticed in simulated lensed systems as it is mostly identical to a real shear. We identify and discuss hereafter two applications of gravitational lensing simulations where artificial shear has a spurious impact if it is not properly anticipated.

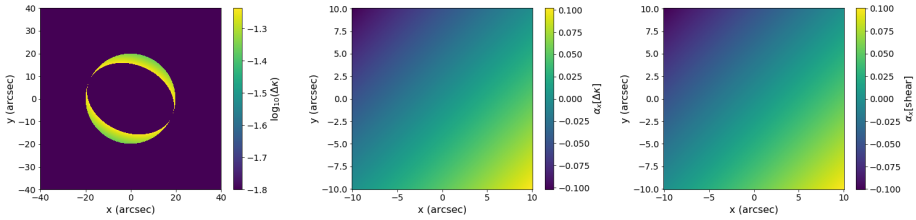

Figure 3.3: Comparison of the excess deflection appearing for a circular truncation with the deflection associated to a shear.

Notes. Left: $\Delta\kappa$ map for a circular truncation and underlying NIE density profile. Middle: α_x map (first component of the deflection $\boldsymbol{\alpha}$ vector) created using FFT convolution for Equation (1.4) using $\Delta\kappa$. Right: α_x map for a pure shear (Equation (3.6)).

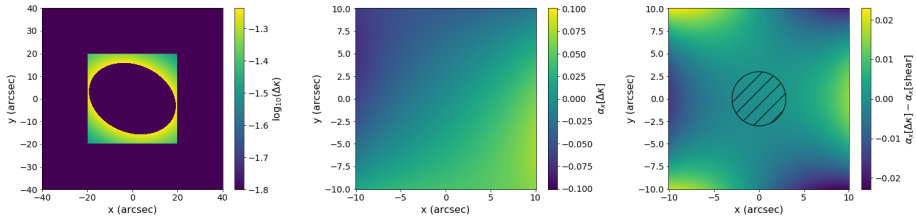

Figure 3.4: Comparison of the excess deflection appearing for a squared truncation with deflection associated to a shear.

Notes. Left: $\Delta\kappa$ map for a squared truncation and underlying NIE density profile. Middle: α_x map created using FFT convolution for Equation (1.4) using $\Delta\kappa$. Right: difference between α_x map created using $\Delta\kappa$ (middle) and α_x map from a shear ; the hatched region is the $3''$-radius region where the lensed images are formed.

3.5.1 Mocks from simulation to test H_0 inference

When mock lensed systems are created from simulations for the H_0 inference, the artificial shear modifies both the image position and the lensing potential, potentially biasing the H_0 inference if it is not accounted for. If shear is not fitted when modelling a mock system, we have seen that a bias as large as 2% exists for a κ map truncated at 20 θ_E for our fiducial NIE. We have observed that this bias is also accompanied by substantial residuals, but a common interpretation of the latter would often be to blame the simplicity of the mass model. Residuals might also remain acceptable depending on the signal-to-noise ratio (S/N) added to the mock system, on the contrast between the quasar and its host galaxy as well as on the lens modelling strategy (i.e. point-source only versus full image). We are aware of a few published works where numerical simulations were used to investigate the robustness of strong lens mod-

elling on the H_0 inference.

The time delay lens modelling challenge (TDLMC, Ding et al. 2021b) has invited the community to test their lens modelling techniques on an ensemble of mock lensed systems with time delays. In their so called Rung3, they used lensing galaxies from Illustris (Vogelsberger et al. 2014b) and zoom-in (Frigo et al. 2019) hydro-dynamical simulations. Half of the systems that were produced for Rung3 were built using a custom code (Xu et al. 2009) and cross-checked with the mesh-based FFT algorithm of the `GLAMER` software (Metcalf & Petkova 2014); each time matter distribution up to R_{200} was considered (i.e. the radius at which the average density is equal to 200 times the critical density of the Universe). The other half were built using a ray-tracing code developed by Hilbert (Hilbert et al. 2007, 2009) based on convergence maps extending up to 2 virial radii. Since the truncation occurs at typically more than $100\theta_E$, one can therefore be confident that a negligible amount of artificial shear is included in those mocks, with a potential impact on H_0 below the percent level.

Tagore et al. (2018) used EAGLE (Schaye et al. 2015) hydro-dynamical simulations to measure the H_0 bias from strong lensing and galaxy dynamics. They calculated the deflection and potential using Equation (1.4) & (1.7) in their discretised form with a convergence map going up to R_{200} (see Appendix A2 of Tagore et al. 2018). This work should thus not be affected by artificial shear as described in this analysis.

3.5.2 Mocks from simulation to infer galaxy properties

When mock lensed systems from simulation are used to infer galaxy properties, a systematic shear linked to the galaxy properties may arise. We identify a few published works where a spurious shear may be present.

The mock lensed systems created as part of the SEAGLE project (Mukherjee et al. 2018) may be affected by artificial shear. SEAGLE aims to study galaxy formation through gravitational lensing using the EAGLE simulation (Schaye et al. 2015; McAlpine et al. 2016; Mukherjee et al. 2018). As strong lensing galaxies, Mukherjee et al. (2018) used EAGLE galaxies at redshift z=0.271, sampled over a 161×161 pixels grid with a spatial resolution on the sky of 0.05″ per pixel, that is, a squared truncation of $8'' \times 8''$. With such a set-up, we estimate the amplitude of the artificial shear to be $\gamma_{\rm art} \sim 0.23 \times |e|$ in the case of an isothermal mass distribution. In SEAGLE–I, Mukherjee et al. (2018) find that their lens models require a shear that is proportional to 0.226 $\times|e|$. They attribute this relation to a degeneracy between shear and ellipticity in lens mass modelling. We rather suggest that most of the effect they unveil is in fact caused by an artificial shear. We note that their modelled density profiles should be correctly retrieved and not affected by this issue since shear is included in their mass modelling.

In another work, Denzel et al. (2020) aimed to find ensembles of free-form mass distributions reproducing SEAGLE-simulated lens data and to compare each ensem-

ble to the true input mass profile. The SEAGLE mocks suffer from artificial shear but a shear is allowed in Denzel et al. (2020) modelling. Thus, the retrieved shear should be biased, while the other parameters characterising the mass distribution should be correctly retrieved.

3.6 Conclusion

Mass profiles from hydro-dynamical simulations can be used to emulate realistic gravitationally lensed systems. This generally requires deriving the lensing potential, the deflection, and magnification through the integration of the numerical mass distribution. Depending on the size and resolution of the numerical mass density profile, this process can become time-consuming, so that one may consider truncating the mass distribution to a region which encloses the lensed images, that is to say soon beyond the Einstein radius. However this truncation, which has been routinely carried out in a circular aperture, would generally introduce numerical artefacts, such as artificial shear, that may be wrongly attributed to intrinsic properties of the mass distribution.

To quantify the biases introduced by truncation, we used elliptical cored power-law models with conformal iso-density contours. When the truncation does not follow an iso-density contour, for example when a circular aperture truncation is used, an artificial shear can be created. Its amplitude depends on the truncation size as well as on the slope and ellipticity of the lens mass density profile. Mukherjee et al. (2018), having used a squared truncation of $8'' \times 8''$, that is, $\theta_{\rm trunc} = 3\text{-}4 \times \theta_E$, report on the existence of a correlation between external shear and ellipticity (see Equation (8) therein) when modelling lensed systems from EAGLE hydro-dynamical simulations. While most of the relation they found should be attributed to spurious shear, the rest of their analysis remains unaffected.

We discourage truncating κ maps at low radius, although this procedure may benefit from minimising the computation needs. Our fiducial isothermal mass distribution, which is characterised by an axis ratio $q \sim 0.75$, can serve as a practical guideline regarding the artificial shear introduced by truncation. Based on our fiducial mass distribution, we recommend a minimum truncation radius of $50 \times \theta_E$ which corresponds to a maximal spurious shear of 0.001. While this seems to be conservative, we stress that not accounting for a shear when modelling such a mock may yield a systematic error on the time-delay as large as 1%. For a galaxy profile that decreases more steeply or is rounder than this fiducial case, truncation can be performed at smaller radii (see Figure 3.2). Conversely, truncation should take place farther away for shallower density or galaxies with a smaller axis ratio.

This work has focused on numerical artefacts introduced by the truncation. However, one should not ignore that truncation also means that some of the mass at the outskirts of the lensing galaxy halo gets removed in the lensing calculation. This mass generally contributes to the lensing plane through a (constant) convergence and (in-

ternal) shear (e.g. Keeton et al. 1997). The impact of internal shear on, for example, the H_0 inference is beyond the scope of this work and will be presented in a forthcoming paper.

3.7 Further discussion at the light of recent literature

In recent literature posterior to the article publication, other works might have been effected by an improper truncation of mass maps. I discuss here Adam et al. (2022), in which a neural network possibly captures the artificial shear effect, hence reaching high performances on simulated data but potentially damaging the use of such network on real data.

Adam et al. (2022) aim at automatically modelling mass distribution of lens systems using machine learning. For this purpose, they used pixelated convergence maps and light source maps, and created the associated lensing image using FFT (following Equations (1.4) & (1.7)). The neural network was trained using the convergence and light maps as inputs and the resulting images as outputs. After training, they find that they can accurately recover the mass distributions in the test set. I believe one of the main constraints that allows one to achieve such a nice performance is the presence of the artefact due to the truncation. Indeed, the convergence maps they used are truncated at 1.5–4 $\theta_{\rm E}$. The subsequent artificial shear is expected to display a strength ranging from 0.01 to 0.1, depending on the Einstein radius, the ellipticity, and the slope of the mass profile. Such shear strengths significantly impact the lensed images. As no shear is explicitly included in the training or test set (as it has no corresponding convergence), the only way to account for the shear contribution is to have a similar cropping of the mass map, i.e. having a mass profile displaying the same ellipticity, with the same radial slope, and which will be truncated at the same size. Let us note that this reasoning with shear is also valid if the truncation creates an artifact more sophisticated than a shear, which can be expected as the squared truncation happens at rather small radii and the mass profile can be more complex than a single elliptical profile. The neural network in Adam et al. (2022) is thus partially trained to identify the correct truncation of the mass profile, which helps constraining the convergence maps and artificially helps breaking degeneracies like the mass sheet degeneracy. If such network were used on real data, the true shear of the system would potentially force the neural network into retrieving a biased ellipticity and mass profile.

CHAPTER 4

MULTIPOLAR COMPONENTS

This chapter is based on Van de Vyvere et al., *TDCOSMO. VII. Boxyness/discyness in lensing galaxies: Detectability and impact on H_0*, A&A 659, A127 (2022). Section 4.1 has been shortened to avoid redundancy with Chapter 1. Minor adjustments have been made to refer to this thesis sections, and the layout of tables has been adapted to be suitable for this thesis format. Section 4.6 was added to further discuss the subject at the light of literature posterior to Van de Vyvere et al. (2022a).

As introduced in Chapter 1, the density profile of lensing galaxies is often considered to be perfectly elliptical. Potential angular structures are generally ignored, except to explain flux ratios of point-like sources (i.e. flux ratio anomalies). Surprisingly, the impact of azimuthal structures on extended images of the source has not been characterised, nor has its impact on the H_0 inference. We address this task by creating mock images of a point source embedded in an extended source and lensed by an elliptical galaxy on which multipolar components are added to emulate boxy or discy isodensity contours. Modelling such images with a density profile free of angular structure allows us to explore the detectability of image deformation induced by the multipoles in the residual frame. Multipole deformations are almost always detectable for our highest signal-to-noise ratio (S/N) mock data. However, the detectability depends on the lens ellipticity and Einstein radius, on the S/N of the data, and on the specific lens modelling strategy. Multipoles also introduce small changes to the time delays. We therefore quantify how undetected multipoles would impact H_0 inference. When no multipoles are detected in the residuals, the impact on H_0

for a given lens is in general less than a few $\mathrm{km\,s^{-1}\,Mpc^{-1}}$, but in the worst-case scenario, combining low S/N in the ring and large intrinsic boxyness or discyness, the bias on H_0 can reach 10-12 $\mathrm{km\,s^{-1}\,Mpc^{-1}}$. If we now look at the inference on H_0 from a population of lensing galaxies with a distribution of multipoles representative of what is found in the light profile of elliptical galaxies, we find a systematic bias on H_0 of less than 1 %. A comparison of our mock systems to the state-of-the-art time-delay lens sample studied by the H0LiCOW and TDCOSMO collaborations indicates that multipoles are currently unlikely to be a source of substantial systematic bias on the inferred value of H_0 from time-delay lenses.

4.1 Introduction

The main lensing galaxy mass distribution is often assumed to follow an elliptical power-law density profile or to be the sum of a baryonic component and dark matter elliptical density component. The role of the assumption of a radial density profile in the time-delay distance inference has been extensively discussed in the literature (Schneider & Sluse 2013, 2014; Xu et al. 2016; Kochanek 2020; Birrer et al. 2020; Kochanek 2021). Less attention has been given to quantifying the impact of an angular change of the density profile on the distance inference. Suyu et al. (2010) quantified the impact of angular structures on H_0 for the time-delay lens system B1608+656 by allowing for a pixelized perturbation of an elliptical density profile. These authors showed that, for that system, perturbations of $< 2\%$ of the lens potential were required, yielding a change in H_0 of less than 1%. This result motivated the use of mostly elliptical mass distribution in subsequent time-delay studies by the H0LICOW and STRIDES collaborations. Nevertheless, a more generic investigation of the role of angular structure on H_0 is still missing. In the present work, we focus on specific angular structures: Fourier-like/multipole perturbations to the elliptical shape of the density profile. The study of early-type galaxies shows that their isophotes are well described by ellipses with Fourier deviations, also called multipoles, of orders three and four (e.g. Rest et al. 2001; Hao et al. 2006; Pasquali et al. 2006; Krajnović et al. 2013; Mitsuda et al. 2017). While the third-order components are generally of small amplitude, those of order four can be substantial, giving rise to clear discy or boxy shapes of the light profile. To our knowledge, the imprint left by multipoles present in the lensing galaxy on extended lensed images has not been discussed in detail in the literature, nor has its impact on H_0.

Due to lensing cross-section, massive early-type galaxies constitute the vast majority of the lens population discovered so far. They are commonly well modelled with density profiles that are perfectly elliptical. Apart from nearby galaxies explicitly included in the model, the only source of angular perturbation generically considered is tidal perturbation —also known as external shear— caused for example by other galaxies along the line of sight towards the lens. Those perturbations of the gravita-

tional potential ψ are quadrupolar, of the form $\psi \propto \cos(2\chi)$, where χ is the azimuthal angle (Trotter et al. 2000; Kochanek 2006; Chu et al. 2013). Higher order multipoles, corresponding to $\psi \propto \cos(m\chi)$, are often ignored as they are expected to displace lensed image positions by $\Delta\theta < 0.003''$ (Section 4 in Kochanek 2006). This forecast however relies on a rather small multipole amplitude ($a_4/\theta_E \sim 0.01$, where θ_E is the Einstein radius of the considered lens), and on the assumption that the light provides a good proxy of the perturbation existing in the total mass.

Only a few studies have included an investigation of the constraints offered by lensing observables on those multipoles. Trotter et al. (2000) used very long baseline interferometry (VLBI) observations of multiple structures in MGJ0414+0534 to constrain high-order multipoles (m=3, 4) in that system. Claeskens et al. (2006) also used the compact star formation regions observed in J1131-1231 to constrain m=3, 4 terms of the multipole expansion. In both cases, the physical meaning of those multipoles was undetermined as either their amplitude or direction could hardly fit any reasonable physical model. The role of multipoles in introducing scatter around the fundamental surface of quad lenses (Gomer & Williams 2018) was recently investigated, revealing that the multipoles may not be sufficient to explain the observed deviation of lensed quasar positions from this surface. The presence of high-order multipoles can also modify flux ratios between quasar images (e.g. Möller et al. 2003; Winn et al. 2003; Keeton et al. 2003, 2005). Those perturbations to the flux ratios introduced by macro-structures in the density profile need to be accounted for when using flux ratio anomalies to constrain the halo mass function (e.g. Mao & Schneider 1998; Xu et al. 2015; Gilman et al. 2019; Hsueh et al. 2020; Gilman et al. 2021). Observational constraints on the amplitude of the high-order multipoles associated to the total mass distribution would therefore be highly valuable, as they could be used to quantify the impact of low-amplitude boxyness and discyness on flux ratio anomalies.

With the advent of deep, high-angular-resolution images of lensed systems, as achievable with the Hubble Space Telescope (HST) or with adaptive optics systems, it is now possible to detect extended images of distant lensed galaxies, even those hosting a quasar (e.g. Bolton et al. 2006; Lagattuta et al. 2012; Suyu et al. 2017). The Einstein rings are known to provide numerous constraints on the mass model and the extended source shape (Kochanek et al. 2001). The only systems for which the shape of the Einstein ring has been used to constrain the amplitude of multipoles are SDSS J0924+0219, HE 0435-1223, B1938+666, and PG 1115+080 (Yoo et al. 2005, 2006). For each galaxy, the deviation of the mass density from ellipsoidal shape because of fourth-order multipoles was found to be consistent with zero, and only upper limits on a_4 could be derived. Extended lensed images are now commonly reproduced by lensed models down to the noise, even when the density profile of the lensing galaxy is modelled as an elliptical power-law density profile (Birrer et al. 2016; Shajib et al. 2019).

The primary aim of this Chapter is to assess the detectability of multipolar com-

ponents, and our second goal is then to quantify the extent to which they modify the H_0 inference. By quantifying the detectability of multipoles in high-resolution lensed images, we intent to find out if multipole-component-induced deformations are effectively negligible in those systems or have been absorbed by the model. In the latter case, we quantify the deviation of the time-delay distance induced by the fitted elliptical model. While this is the main motivation of this work, the presence of multipoles in the total mass profile is also important for our general understanding of galaxies and of the ability of interactions between baryons and dark matter to shape the galaxy density profile. It is also relevant for dark matter studies based on flux ratio anomalies (Hsueh et al. 2017, 2020; Gilman et al. 2020a,b; Nierenberg et al. 2020; Gilman et al. 2021): the ability to constrain the presence of (dark) multipole-like structures in the lens from the analysis of the lensed images would enable further tightening of the constraints on the dark matter properties inferred from flux ratio anomalies.

In Section 4.2, we introduce our general methodology, the mathematical definitions of the main lens mass profiles used in our analysis, and explain mock-image creation and fitting procedure. In Section 4.3, we systematically test the detectability of multipoles depending on different parameters and discuss their detectability in real cases. In Section 4.4, we then quantify the effect of the presence of multipoles on H_0 inference at a single-galaxy level and at a population level, and assess their potential influence in cosmological lensing analyses. We summarise and conclude in Section 4.5. Section 4.6 was added to compare the detectability assessed in this work to the one found in an other study posterior to the article publication.

For all calculations presented in this Chapter involving non-angular quantities, we assume a flat ΛCDM cosmological model with $\Omega_\mathrm{m} = 0.3$, $\Omega_\Lambda = 0.7$, and $H_0 = 70$ $\mathrm{km\,s^{-1}\,Mpc^{-1}}$.

4.2 Methodology

To quantify the detectability of multipoles from strongly lensed images, we designed a controlled set of simulated lensed systems containing multipoles and modelled them using state-of-the-art techniques. Specifically, we emulate mock HST-like data of a quasar and its host lensed by a singular isothermal ellipsoid (SIE) with fourth-order multipoles and shear. Those multipoles are the dominant non-zero multipole contributions that control boxyness or discyness of galaxies (see Figure 4.1). We then fit the mock images with an SIE and shear (i.e. without fourth-order azimuthal structures).

With this setup, we then analyse the effect of different factors on the quality of the retrieved fit. A good fit means that the multipoles remain unnoticed in imaging data of a lens system. This is the situation where multipoles may introduce unnoted systematic errors into the analysis, especially into the H_0 inference. Conversely, a poor fit would be an indication of modelling inadequacy. We assume that any structure

detected in the residuals[1] would be identified as a need to include multipoles in the lens mass model. However, we do not explore the ability of macro-models to effectively recover the input multipoles. Instead, we seek the limit at which visible residual patterns become present over the noise. This depends on the mass and source model assumptions and on the data quality. Specifically, we explore the role of the shear, the lens axis-ratio, the additional freedom granted by relaxing the slope constraint in the fit —and the influence of the radial mass profile in that case—, the signal-to-noise ratio (S/N), the multipole strength, and the freedom allowed in the quasar host galaxy morphology during the fit.

We finally look at the impact of unnoticed multipolar components on time-delay cosmography. Focusing on our previous mock systems in cases where multipoles remain undetected, we first explore the H_0 recovery for those specific systems. We then extend the study by constructing a sample of lenses that emulates a realistic population of lenses and look at the combined H_0 inference for different S/N levels.

4.2.1 Lens mass profile

To construct mock images, one needs to assess a lensing mass profile. As we are interested in the effect of azimuthal structures such as boxyness and discyness in the lensing galaxy, we first select a radially simple mass profile. The density profile of lensing galaxies is generally well approximated by a mass distribution that follows a power-law density profile and some external shear (Suyu et al. 2009, 2010; Treu & Marshall 2016; Yıldırım et al. 2020; Wong et al. 2020). The mean slope of the profile has been found to be close to isothermal (Courbin & Minniti 2002; Koopmans et al. 2003; Suyu et al. 2010), such that the singular isothermal ellipsoid (SIE) provides a simple but realistic choice of density profile for the lens[2]. In addition, we add a multipole perturbation to the ellipticity and include a shear term to account for the tidal perturbation of the potential, such as the one due to line-of-sight mass distribution. Below, we describe the lensing potential associated to each of these components. The deflection angle and Hessian matrix can be found analytically by differentiation of the potential.

Following Keeton & Kochanek (1998), the potential of our SIE is given by the potential of a non-singular isothermal ellipsoid (NIE, see Equations (3.1)–(3.4)) with a virtually null core size. This translates into a potential —for an SIE aligned with the x-axis— at position $\boldsymbol{\theta} = (x, y)$:

$$\psi_{\rm SIE}(\boldsymbol{\theta}) = x\,\alpha_x + y\,\alpha_y, \tag{4.1}$$

[1] We show in Section 4.3 that multipoles have rather characteristic imprints on the arc images, such that their origin may be easy to identify.

[2] In Sections 4.3.3 & 4.3.4, more complex mass profiles are considered. The mathematical details of those profiles are given in Appendix 4.B.

with

$$\alpha_x(\boldsymbol{\theta}) = \frac{b}{\sqrt{1-q^2}} \arctan\left(\frac{\sqrt{1-q^2}x}{\sqrt{q^2x^2+y^2}}\right), \tag{4.2}$$

$$\alpha_y(\boldsymbol{\theta}) = \frac{b}{\sqrt{1-q^2}} \operatorname{arctanh}\left(\frac{\sqrt{1-q^2}y}{\sqrt{q^2x^2+y^2}}\right), \tag{4.3}$$

where q is the axis ratio, and b is the scale radius and is equal to $\theta_E\sqrt{q}$, where θ_E is the Einstein radius. The difference in potential between two SIEs with different ellipticities is a quadrupole moment.

The multipole has several definitions in the literature. We chose to use the same convention as Xu et al. (2015) and Keeton et al. (2003). The lensing potential at a position $\boldsymbol{\theta} = (x, y) = (\theta\cos\phi, \theta\sin\phi)$ is given by:

$$\psi_{\text{multipole}}(\boldsymbol{\theta}) = \theta \frac{1}{1-m^2} a_m \cos\left(m(\phi-\phi_m)\right), \tag{4.4}$$

where m is the order of the multipole, a_m is the multipole strength, and ϕ_m is the main axis orientation angle. The fourth-order multipole is an octupolar moment of the potential. It introduces a 'discy' shape when $\phi_4 = 0$ and a 'boxy' shape when $\phi_4 = 45°$ (see Figure 4.1). In the sample studied by Hao et al. (2006), 70% of elliptical galaxies display a multipole $a_4 < 0.02$ (see Figure 4.2). We note that other authors (e.g. Bender et al. 1988, 1989; Hao et al. 2006; Penoyre et al. 2017; Frigo et al. 2019) prefer the normalised a_4 and b_4 convention, using $(a_4/a)_{\text{conv}}$ and $(b_4/a)_{\text{conv}}$ where a is the length of the semi-major axis of the reference ellipse, $(a_4/a)_{\text{conv}}$ represents the cosine deformations of that ellipse, and $(b_4/a)_{\text{conv}}$ represents the sine deformations. This normalised convention is more appropriate when dealing with specific isophotes at different radii, while our a_4 convention is particularly useful for the creation of a general lens density profile that can be defined independently of the main lens shape. Conversion between the two conventions is explained in Appendix B2 of Xu et al. (2015) and is summarised here :

$$a_4 = \sqrt{(a_4/a)^2_{\text{conv}} + (b_4/a)^2_{\text{conv}}} \times \frac{\theta_E('')}{\sqrt{q}} \tag{4.5}$$

$$\phi_4 = \frac{1}{4} \times \arctan\left(\frac{(b_4/a)_{\text{conv}}}{(a_4/a)_{\text{conv}}}\right). \tag{4.6}$$

As we only consider pure boxyness and discyness in the following analysis (i.e. we always have $(b_4/a)_{\text{conv}} = 0$), the backward conversion is simply

$$(a_4/a)_{\text{conv}} = \frac{\pm a_4 \times \sqrt{q}}{\theta_E('')}, \tag{4.7}$$

which is positive in the discy case and negative in the boxy case.

The shear is defined by the lensing potential at position $\boldsymbol{\theta} = (x, y)$ by Equation (1.20), that is,

$$\psi_{\rm shear}(\boldsymbol{\theta}) = \frac{1}{2}\left(\gamma_1 x^2 + 2\gamma_2 xy - \gamma_1 y^2\right),$$

where γ_1 and γ_2 are the components of the complex shear. The shear strength $\gamma_{\rm ext} = \sqrt{\gamma_1^2 + \gamma_2^2}$ and its orientation $\phi_{\rm ext} = \frac{1}{2}\arctan(\gamma_2/\gamma_1)$. The shear is a quadrupole moment of the potential.

For our baseline model, we consider $\theta_E = 2''$ and $q = 0.8$ for the SIE. We orient the SIE with an angle of 22° with respect to the x-axis. The orientation of the multipole ϕ_4 is equal to either 0° or 45° in a reference frame aligned with the main lens, and this will create either discy or boxy mass profiles. The strength of the multipole is $a_4 = 0.01$ by default. We fix the shear amplitude to 0.05 and its orientation to 30° with respect to the SIE main axis. The shear is therefore neither oriented on a multipole axis nor on the SIE main axis. No spurious artificial shear due to truncation of pixelated mass maps is introduced (Van de Vyvere et al. 2020, i.e. Chapter 3) because we have an analytical description of each component of the lens mass profile.

While one can argue that using an Einstein radius of $2''$ is on the upper edge of the distribution of Einstein radii in observed lensing systems, it is particularly relevant to use such an θ_E in our study to highlight the effect of multipoles. As explained in Section 4.3.8, for a fixed exposure time and source magnitude and shape, a smaller Einstein radius would yield a smaller signal-to-noise ratio in the ring and therefore reduce our ability to explore the lens properties that most impact the multipole detectability.

4.2.2 Mock images creation

The modelling of extended lensed images requires high-spatial-resolution data, which in general are provided by space-based or by ground-based AO systems (e.g. Lagattuta et al. 2010; Chen et al. 2016; Suyu et al. 2017). In this work, we chose to emulate mock[3] HST images observed with the WFC3 camera through the filter F160W. This choice is guided by the data used in many time-delay cosmography studies (Suyu et al. 2017), and in other studies using high-quality mock lens images (e.g. Ding et al. 2021b; Park et al. 2021; Wagner-Carena et al. 2021). The near-infrared (NIR) band confers the advantage that, in general, it provides the highest host brightness (see e.g. Ross et al. 2009), and is *a priori* the most favourable band with which to analyse extended lensed features. In addition, we also consider a transparent lens, which is equivalent to assuming that the lens light is perfectly subtracted and provides a negligible contribution to the photon noise in the ring. Due to the lack of lens light, this setup slightly increases the S/N in the ring compared to a real NIR HST image. On the other hand,

[3]Notebook link: https://github.com/TDCOSMO/TD_data_public

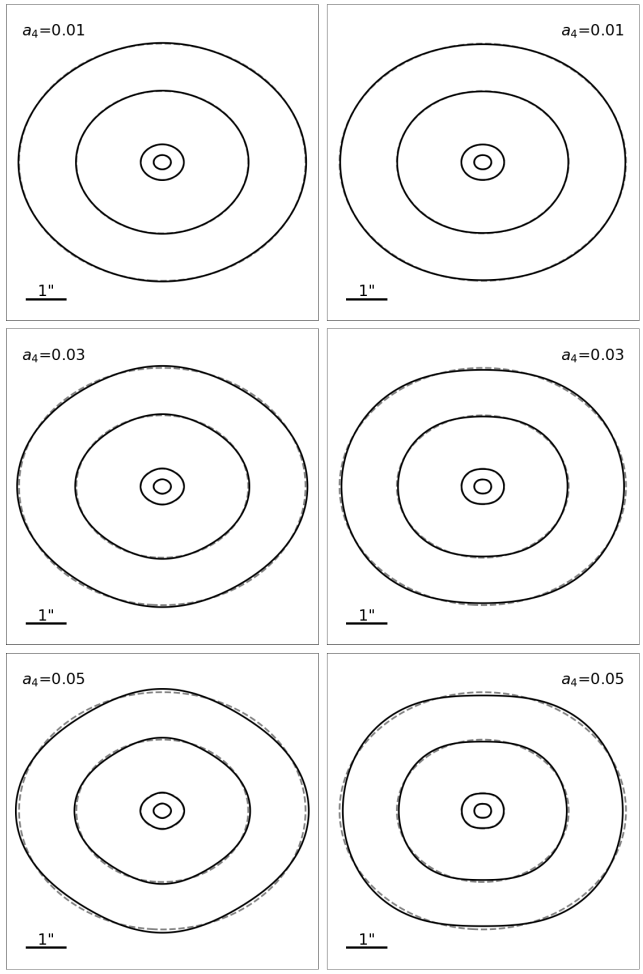

Figure 4.1: Comparison of isodensity contours for an SIE mass profile and an SIE + fourth-order multipole mass profile.

Notes. Isodensity contours for an SIE mass profile (grey dashed line) and an SIE + fourth-order multipole mass profile (black plain line). The multipole component has a strength $a_4 = 0.01$ (top), $a_4 = 0.03$ (middle), or $a_4 = 0.05$ (bottom) and is oriented along the SIE main axis to create a discy profile (left), or at 45° to the SIE main axis to create a boxy profile (right).

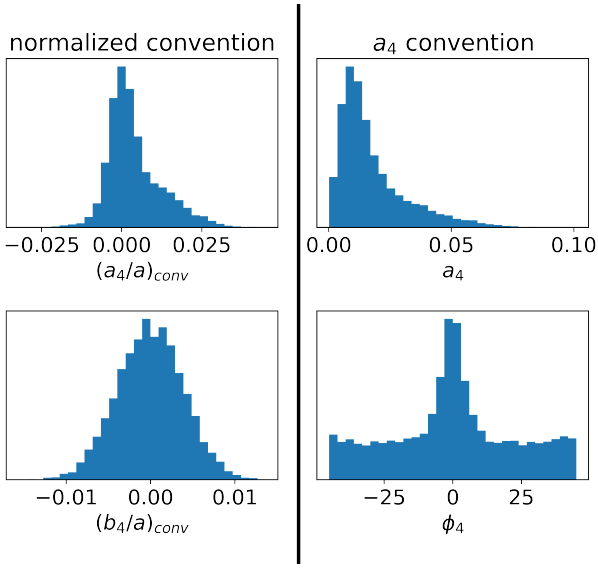

Figure 4.2: Distribution of fourth-order multipoles in the light of local elliptical galaxies from Hao et al. (2006).

Notes. The two panels display the distribution for the normalised $(a_4/a)_{\rm conv}$ and $(b_4/a)_{\rm conv}$ convention (left) and our a_4 convention used in this Chapter (right), for $\theta_E = 2''$ and $q = 0.8$ (see Equations (4.5) & (4.6)).

state-of-the-art lens modelling is based on multi-band HST data. This increases the effective signal in the ring. Moreover, the bluer bands have higher angular resolution and better sampling of the PSF due to smaller pixels, even if they are not able to fully balance the lack of host flux at those wavelengths. The relative advantage of the bluer bands is also that the lens light drops off more quickly, and therefore blends less with the ring. This last benefit is counterbalanced in our setup by the use of a transparent lens. Therefore, our single-band setup should, at least partially, compensate for the lack of bluer bands and give a reasonable indication of the detectability of multipole-induced deformation of the ring.

We used the same PSF as the one used in the Time Delay Lens Modeling Challenge (TDLMC, Ding et al. 2021b) for the Rung 2 and 3, created from the drizzling of eight PSFs extracted from real HST images. We use a pixel size of $0.08''$, typical of drizzled NIR HST images. We include photon and read-out noise (RON). The zero-point in the AB system is 25.96 mag. Our baseline setup corresponds to an exposure of 5400s. The 'sky' brightness, that is zodiacal light and Earth shine, is fixed at 22.3 mag/arcsec^2 and the RON is set to 21 e$^-$. Those values are based on the WFC3 documentation (Dressel

2012) and concur with other works creating typical HST WFC3/F160W images (Ding et al. 2021b; Park et al. 2021; Wagner-Carena et al. 2021).

We consider a simple source light distribution constituted from an AGN on top of a circular host following a Sersic profile. The choice of a circular source is based on the fact that using a more complicated source with a principal axis may produce results that will be highly dependent on its orientation, while the goal of this analysis is to create mock systems where the azimuthal structure of the lens is the only source of potential bias. We set the contrast between the QSO and its host based on the work of Dunlop et al. (2003) and Jahnke & Wisotzki (2003). This corresponds to a host that is brighter than the QSO by 0.5 mag. For our baseline model, the unlensed quasar apparent brightness is set to 21 mag and the unlensed host is set to 20.5 mag. This yields a mean magnitude of the lensed QSO of 18.5 mag. The host galaxy morphology is a circular Sersic with a half-light radius $R_{\rm sersic} = 0.1''$ and a Sersic index $n_{\rm sersic} = 3$. The source is placed at a redshift $z_s = 2$.

The lensing galaxy density profiles are described in the previous section. The lens redshift is $z_l = 0.271$. For each mock lens density profile, we only consider quad configurations. We focus on four-lensed-images configurations for two reasons: first, cosmographic studies prioritise such systems as they provide multiple delays. Second, dark matter investigations based on flux ratio anomalies currently only rely on samples of quads. More specifically, we consider four quad configurations of lensed images by positioning the source at various locations with respect to the inner caustic. The four sources and associated image positions are illustrated in Figure 4.3. The source is either close to the long axis cusp (*cusp_l*), close to the short axis cusp (*cusp_s*), close to a *fold* caustic, or centred (*cross* image configuration). Specifically, we locate the source at 80% of the distance between the centre and the cusp and fold caustics. The source for the cross-configuration is at a 5% distance from the centre in the direction of the long axis cusp. The `lenstronomy` software is used to compute the mock images (Birrer & Amara 2018).

The time-delays are calculated within `lenstronomy`. We fix the time-delays to the 'ground truth' from the macro model but we consider a 2% uncertainty on the delay with a lower boundary of 1 day when performing the lens modelling.

4.2.3 Modelling setup

Once the mock image is created, we model it with a standard modelling technique constrained by the pixels inside a mask which omits all pixels that are below twice the background noise level. We use `lenstronomy` and its particle swarm optimisation (PSO, Kennedy & Eberhart 1995; Shi & Eberhart 1998) to find the model parameters that maximise the likelihood. The likelihood contains terms associated to the image residuals, to the time-delays, and to the position of the four ray-traced back point-source positions in the source plane (see Birrer & Amara 2018). This last likeli-

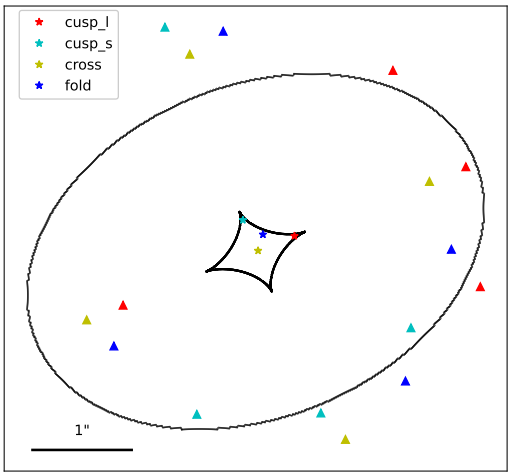

Figure 4.3: Illustration of the four lensing configurations used in this work.

Notes. The inner caustic (bold) and associated critical curve are represented in black. The four different source positions are shown with star symbols and the corresponding image positions are drawn with triangles. Each configuration is displayed in a single colour (see legend).

hood term allows efficient sampling by relaxing the constraint that all point sources should ray-trace back to the exact same position whilst still demanding a sufficiently accurate matching of the lens equation. The model considered is identical to the input mass profile except that no multipoles are included: the lens model is an SIE + shear, the source model is a circular Sersic, and the four point-sources are modelled in the image plane with their positions in the source plane matching the source centre. After the PSO has converged, a Markov Chain Monte Carlo (MCMC) using `emcee` (Goodman & Weare 2010; Foreman-Mackey et al. 2013) is performed to sample the posterior probability distribution.

4.3 Multipole detectability

We first study the base case described in the previous section. We set the multipole to $a_4 = 0.01$ and $\phi_4 = 0°$ with respect to the SIE main axis for discy cases and $\phi_4 = 45°$ with respect to the SIE main axis for boxy cases; see top panel of Figure 4.1. This multipole level of boxyness and discyness is typical of what is observed in the light profile of elliptical galaxies (Figure 4.2). The resulting fits are shown in Figure 4.4. The

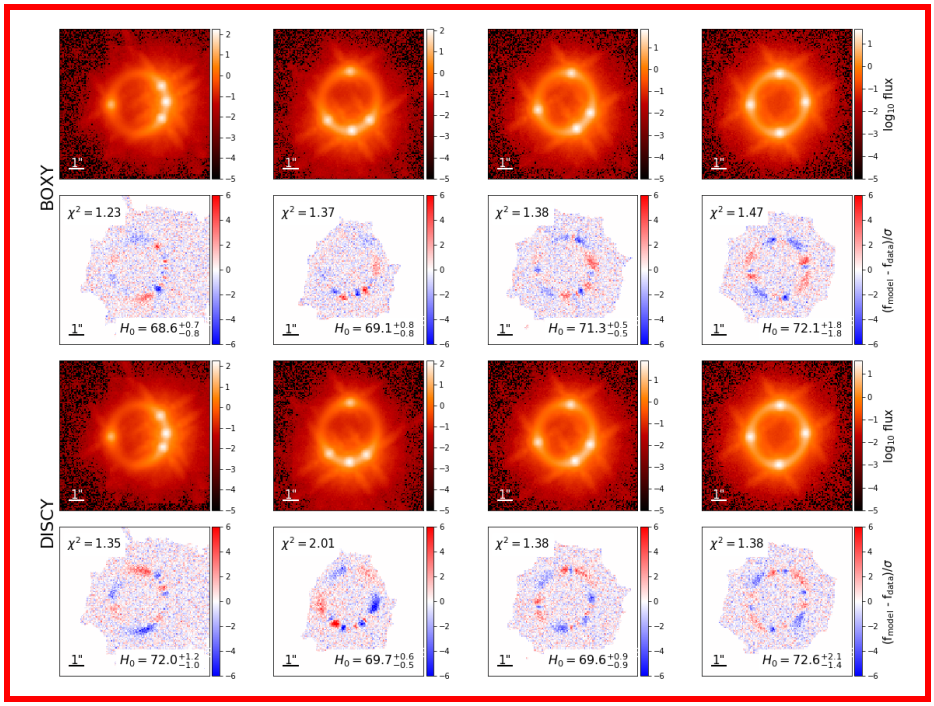

Figure 4.4: Results of the base case mock images created and fitted as described in Section 4.2.

Notes. Those systems are also displayed in red in Table 4.1. Top 2 rows: Mock images made from one boxy galaxy for four configurations and residuals associated to the fit for each image with χ^2 and H_0 inference. Bottom 2 rows: Same as in the top rows but for the discy lensing galaxy.

residuals and χ^2 displayed are for the best model, that is, the model with the highest likelihood. The H_0 results are the median value of the MCMC sampling with the error corresponding to the 0.16 and 0.84 quantile. Regardless of the image configuration and multipole angle, we see an alternation of positive and negative residuals beyond the 3σ level when running azimuthally along the ring. Those correlated structures are sufficiently large and numerous to yield a reduced χ^2 much larger than 1. The impact on H_0 inference is discussed in Section 4.4.

Our baseline setup shows that the imprint of multipoles on lensed images would be ubiquitous. We now systematically investigate how deviation from the baseline assumption impacts those results. We quantify the influence of the following parameters:

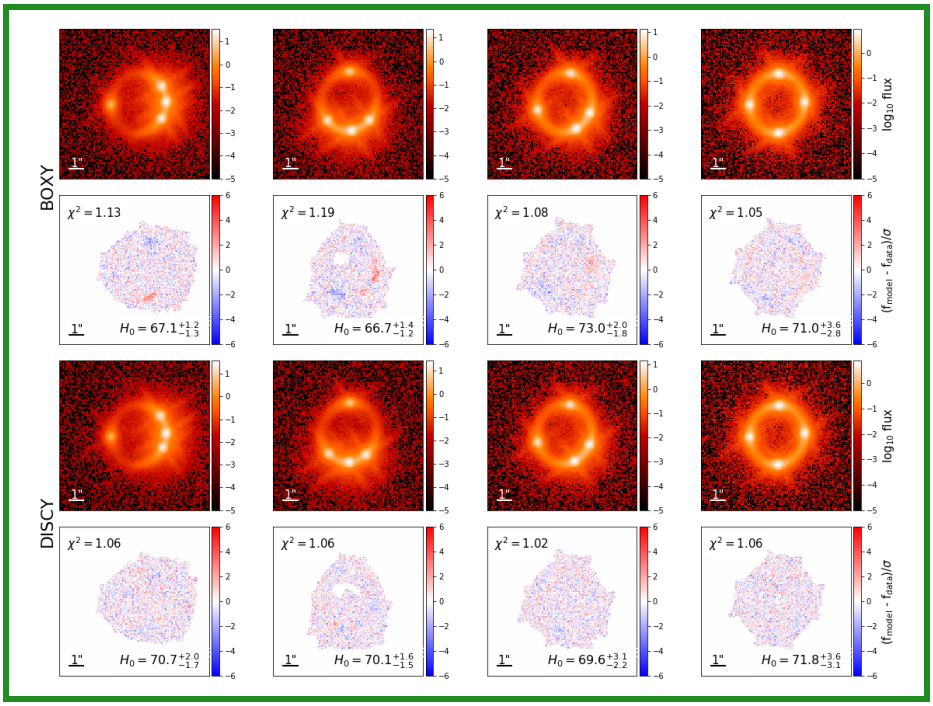

Figure 4.5: Same as Figure 4.4, but with an exposure time of 3000s instead of 5400s and the unlensed quasar and extended source fainter by 1.75 mag.

Notes. Those results are also displayed in green in Table 4.1. We note that the mask, which is defined by a threshold of twice the background noise, may sometimes have holes inside the Einstein ring due to the lack of lensed signal at those locations.

- Shear: we investigate the extreme case where the shear amplitude of the mock system is equal to zero.

- Lensing galaxy ellipticity: we consider three values representative of existing lensing galaxy samples, $q = (0.7, 0.8, 0.9)$.

- Assumption on the fitted lens mass profile: we allow the power-law slope to deviate from the isothermal case in the modelling while keeping the input slope isothermal.

- Assumption on the fitted lens mass profile when the mock lensing galaxy is not a SIE: we extend the previous point by using a mock lensing galaxy with varying

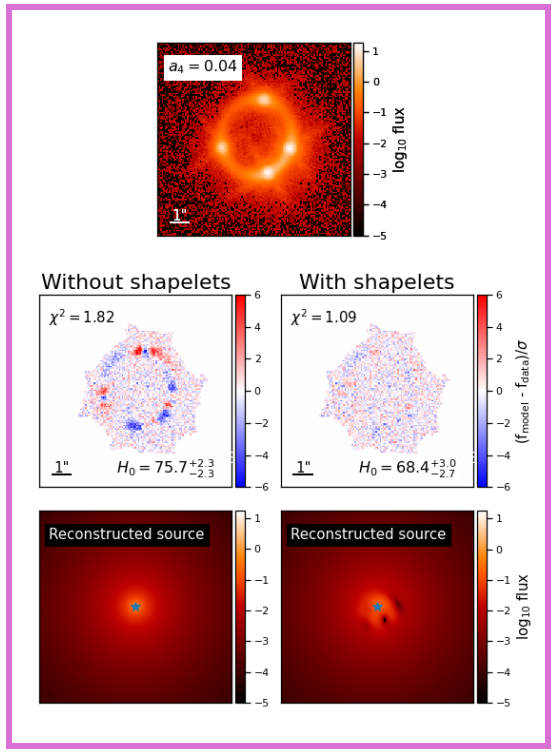

Figure 4.6: Illustration of the influence of complexity in the modelled source.

Notes. Top: Mock image created for 3000s exposure time and a bright source. The lens has the same characteristics as for the base case (see Section 4.2.1), but is discy with $a_4 = 0.04$ in a fold configuration. Bottom: Fit of the above image with (right) and without (left) adding shapelet reconstruction for the source during the fitting process. These results are also displayed in purple in Table 4.1.

profile slope with radius, following a baryon + dark matter prescription, and allow the fitted power-law slope to deviate from the isothermal case.

- S/N: we test three different S/Ns by varying the exposure time and/or the source and quasar brightness.
- Multipole strength: we vary a_4 between 0.01 and 0.05. We note that comparison of those values to multipole amplitudes found in the literature may require the use of Equation (4.7).
- Assumption of the source morphology: we include shapelets in the source reconstruction during the modelling.

The following sections discuss the results obtained for each setup change. Table 4.1 summarises the main results of those tests, providing for each case the value of the reduced χ^2 for the best model and inferred value of H_0 from the MCMC sampling (median, 0.16 quantile, and 0.84 quantile). Two subsamples of mock systems appear multiple times in the table: our baseline case (red) and a lower S/N (3000 s exposure time with a bright source) case with $a_4 = 0.01$ (green). Our base case is the ideal case for which multipoles would leave ubiquitous imprints in the lensed images (see Figure 4.4); it is used as the starting point to compare the influence of different parameters such as the shear, the galaxy ellipticity, and the S/N. Because imprints from multipoles are ubiquitous with the fiducial case, we have built a lower S/N system to study other factors (see Figure 4.5). This lower S/N setting is afterwards used for studying the influence of the multipole strength and the addition of source structure (i.e. shapelets) in the modelling. A specific pair of tests illustrating how the source can absorb perturbations introduced by multipoles is shown in Figure 4.6. The corresponding cases are outlined in purple in Table 4.1.

		cusp_l		cusp_s		fold		cross	
		Boxy	Discy	Boxy	Discy	Boxy	Discy	Boxy	Discy
with shear	χ^2	1.23	1.35	1.37	2.01	1.38	1.38	1.47	1.38
	H_0	$68.6^{+0.7}_{-0.8}$	$72.0^{+1.2}_{-1.0}$	$69.1^{+0.8}_{-0.8}$	$69.7^{+0.6}_{-0.5}$	$71.3^{+0.5}_{-0.5}$	$69.6^{+0.9}_{-0.9}$	$72.1^{+1.8}_{-1.8}$	$72.6^{+2.1}_{-1.4}$
without shear	χ^2	1.22	1.03	1.35	1.03	1.34	1.31	1.31	1.38
	H_0	$69.9^{+0.8}_{-0.9}$	$70.2^{+0.8}_{-0.6}$	$71.8^{+1.1}_{-1.0}$	$70.4^{+0.6}_{-0.7}$	$69.8^{+1.5}_{-1.4}$	$73.3^{+1.0}_{-1.1}$	$66.3^{+1.1}_{-1.1}$	$75.3^{+1.6}_{-1.6}$
$q = 0.7$	χ^2	1.09	1.04	1.32	1.31	1.15	1.16	1.11	1.09
	H_0	$71.2^{+1.1}_{-1.2}$	$71.1^{+1.1}_{-1.1}$	$69.7^{+1.0}_{-0.8}$	$71.0^{+0.7}_{-0.6}$	$71.7^{+0.8}_{-0.8}$	$70.8^{+0.7}_{-0.9}$	$70.6^{+2.1}_{-2.5}$	$73.7^{+1.5}_{-1.5}$
$q = 0.8$	χ^2	1.23	1.35	1.37	2.01	1.38	1.38	1.47	1.38
	H_0	$68.6^{+0.7}_{-0.8}$	$72.0^{+1.2}_{-1.0}$	$69.1^{+0.8}_{-0.8}$	$69.7^{+0.6}_{-0.5}$	$71.3^{+0.5}_{-0.5}$	$69.6^{+0.9}_{-0.9}$	$72.1^{+1.8}_{-1.8}$	$72.6^{+2.1}_{-1.4}$
$q = 0.9$	χ^2	1.17	1.42	1.62	1.28	1.82	2.00	2.65	2.69
	H_0	$70.4^{+0.8}_{-0.7}$	$72.6^{+2.2}_{-2.8}$	$74.1^{+0.8}_{-0.8}$	$69.4^{+0.7}_{-0.8}$	$73.2^{+1.1}_{-0.9}$	$70.4^{+1.0}_{-0.7}$	$75.9^{+0.9}_{-1.2}$	$71.0^{+1.1}_{-1.0}$
slope fixed	χ^2	1.23	1.35	1.37	2.01	1.38	1.38	1.47	1.38
	H_0	$68.6^{+0.7}_{-0.8}$	$72.0^{+1.2}_{-1.0}$	$69.1^{+0.8}_{-0.8}$	$69.7^{+0.6}_{-0.5}$	$71.3^{+0.5}_{-0.5}$	$69.6^{+0.9}_{-0.9}$	$72.1^{+1.8}_{-1.8}$	$72.6^{+2.1}_{-1.4}$
slope free	χ^2	1.20	1.23	1.33	1.63	1.38	1.35	1.41	1.28
	H_0	$63.3^{+1.6}_{-1.7}$	$80.0^{+2.3}_{-2.4}$	$65.1^{+1.1}_{-1.1}$	$79.3^{+1.4}_{-1.3}$	$74.6^{+2.2}_{-2.5}$	$75.7^{+2.8}_{-2.3}$	$79.7^{+4.8}_{-3.9}$	$84.4^{+4.5}_{-4.2}$
5400s, very bright source	χ^2	1.23	1.35	1.37	2.01	1.38	1.38	1.47	1.38
	H_0	$68.6^{+0.7}_{-0.8}$	$72.0^{+1.2}_{-1.0}$	$69.1^{+0.8}_{-0.8}$	$69.7^{+0.6}_{-0.5}$	$71.3^{+0.5}_{-0.5}$	$69.6^{+0.9}_{-0.9}$	$72.1^{+1.8}_{-1.8}$	$72.6^{+2.1}_{-1.4}$
3000s, bright source	χ^2	1.13	1.06	1.19	1.06	1.08	1.01	1.05	1.06
	H_0	$67.1^{+1.2}_{-1.3}$	$70.7^{+2.0}_{-1.7}$	$66.7^{+1.4}_{-1.2}$	$70.1^{+1.6}_{-1.5}$	$73.0^{+2.0}_{-1.8}$	$69.6^{+3.1}_{-2.2}$	$71.0^{+3.6}_{-2.8}$	$71.8^{+3.6}_{-3.1}$
3000s, faint source	χ^2	1.04	1.04	1.06	1.03	1.03	1.00	1.08	1.03
	H_0	$64.6^{+1.7}_{-1.3}$	$70.3^{+2.2}_{-1.8}$	$66.1^{+1.4}_{-1.3}$	$70.3^{+1.5}_{-1.5}$	$71.2^{+2.4}_{-2.4}$	$70.2^{+2.3}_{-2.4}$	$72.1^{+4.0}_{-3.8}$	$73.7^{+3.1}_{-3.6}$

Table 4.1: Summary table of χ^2 and H_0 results for the cases tested in Section 4.3.

		cusp_l		cusp_s		fold		cross	
		Boxy	Discy	Boxy	Discy	Boxy	Discy	Boxy	Discy
3000s bright,	χ^2	1.13	1.06	1.19	1.06	1.08	1.01	1.05	1.06
$a_4 = 0.01$	H_0	$67.1^{+1.2}_{-1.3}$	$70.7^{+2.0}_{-1.7}$	$66.7^{+1.4}_{-1.2}$	$70.1^{+1.6}_{-1.5}$	$73.0^{+2.0}_{-1.8}$	$69.6^{+3.1}_{-2.2}$	$71.0^{+3.6}_{-2.8}$	$71.8^{+3.6}_{-3.1}$
3000s bright,	χ^2	1.36	1.15	1.83	1.18	1.32	1.16	1.31	1.17
$a_4 = 0.02$	H_0	$59.6^{+1.9}_{-1.4}$	$70.1^{+1.7}_{-1.9}$	$64.7^{+1.3}_{-1.6}$	$71.7^{+1.3}_{-1.3}$	$74.6^{+1.9}_{-1.7}$	$69.9^{+2.7}_{-2.2}$	$73.8^{+3.2}_{-3.3}$	$77.8^{+5.8}_{-4.9}$
3000s bright,	χ^2	1.64	1.27	2.87	1.29	1.64	1.45	1.77	1.29
$a_4 = 0.03$	H_0	$55.7^{+0.9}_{-0.8}$	$71.9^{+2.3}_{-2.1}$	$69.5^{+1.6}_{-1.3}$	$73.3^{+1.4}_{-1.1}$	$77.3^{+2.0}_{-1.5}$	$71.6^{+2.2}_{-2.5}$	$78.9^{+5.4}_{-4.4}$	$76.7^{+4.9}_{-4.4}$
3000s bright,	χ^2	1.87	1.34	4.36	1.66	1.97	1.82	2.32	1.57
$a_4 = 0.04$	H_0	$49.1^{+1.1}_{-1.0}$	$69.2^{+2.1}_{-1.5}$	$73.2^{+1.5}_{-1.1}$	$75.3^{+1.7}_{-1.3}$	$79.4^{+2.4}_{-2.5}$	$75.7^{+2.3}_{-2.3}$	$84.3^{+4.4}_{-3.9}$	$79.3^{+4.2}_{-3.1}$
3000s bright,	χ^2	3.39	1.51	6.02	1.84	2.50	2.45	3.17	1.89
$a_4 = 0.05$	H_0	$47.7^{+1.4}_{-1.3}$	$71.3^{+2.0}_{-1.9}$	$81.4^{+1.6}_{-2.0}$	$75.5^{+1.6}_{-1.5}$	$83.7^{+2.8}_{-2.7}$	$77.2^{+2.9}_{-2.4}$	$90.1^{+4.2}_{-4.4}$	$82.7^{+5.0}_{-4.1}$
3000s bright,	χ^2	1.03	1.02	1.07	1.00	1.02	0.98	1.01	1.04
a_4=0.01, **shapelet**	H_0	$66.2^{+1.8}_{-2.0}$	$71.1^{+2.5}_{-2.1}$	$62.8^{+1.3}_{-1.5}$	$71.0^{+1.6}_{-1.7}$	$72.9^{+3.3}_{-2.8}$	$69.7^{+2.9}_{-3.1}$	$68.5^{+3.4}_{-3.2}$	$71.6^{+7.4}_{-5.0}$
3000s bright,	χ^2	1.07	1.07	1.18	1.10	1.11	1.04	1.14	1.10
a_4=0.02, **shapelet**	H_0	$62.3^{+2.0}_{-1.8}$	$71.6^{+2.0}_{-1.9}$	$58.2^{+1.3}_{-1.3}$	$71.9^{+1.5}_{-1.8}$	$72.1^{+2.6}_{-2.3}$	$69.1^{+3.0}_{-2.6}$	$66.0^{+3.3}_{-2.6}$	$77.2^{+5.7}_{-6.1}$
3000s bright,	χ^2	1.13	1.10	1.22	1.16	1.21	1.18	1.31	1.16
a_4=0.03, **shapelet**	H_0	$59.1^{+1.1}_{-1.0}$	$73.1^{+2.4}_{-1.9}$	$63.9^{+1.4}_{-1.6}$	$75.3^{+2.0}_{-1.4}$	$72.3^{+2.6}_{-2.4}$	$68.9^{+3.3}_{-2.6}$	$41.3^{+3.1}_{-3.3}$	$72.8^{+4.4}_{-4.0}$
3000s bright,	χ^2	1.21	1.13	1.50	1.13	1.17	1.09	1.62	1.14
a_4=0.04, **shapelet**	H_0	$54.7^{+0.8}_{-0.7}$	$67.4^{+2.3}_{-2.1}$	$61.3^{+1.6}_{-1.6}$	$77.0^{+1.9}_{-2.1}$	$69.6^{+2.1}_{-2.6}$	$68.4^{+3.0}_{-2.7}$	$73.2^{+2.4}_{-2.1}$	$77.2^{+6.2}_{-5.2}$
3000s bright,	χ^2	1.47	1.19	1.63	1.44	1.26	1.12	2.25	1.47
a_4=0.05, **shapelet**	H_0	$42.2^{+1.1}_{-1.2}$	$69.4^{+2.0}_{-1.9}$	$44.2^{+1.4}_{-1.2}$	$75.8^{+2.1}_{-2.1}$	$69.1^{+2.9}_{-2.4}$	$67.3^{+3.3}_{-2.4}$	$62.7^{+2.5}_{-2.3}$	$75.4^{+5.1}_{-4.3}$

Table 4.1 (*Continued*): Summary table of χ^2 and H_0 results for the cases tested in Section 4.3.

Table 4.1 (*Continued*): Summary table of χ^2 and H_0 results for the cases tested in Section 4.3.

Notes. The base case has $\gamma_{\rm ext} = 0.05$, $q = 0.8$, 5400 s exposure time, a very bright source ($\langle m_{\rm QSO}\rangle$=18.5 mag), and $a_4 = 0.01$ and is fitted without shapelets in the source. This setup appears at different places in the table; the corresponding rows are coloured in red and the results are also shown in Figure 4.4. The differences between the base case and the others are indicated in the first column, the rows list the different modifications applied to the base case. The specifications in **bold** are changes made with respect to the model, while the other changes are specific to the mock-image creation. The 3000 s exposure time and bright source ($\langle m_{\rm QSO}\rangle$=20.25 mag) setup with a_4=0.01 is displayed at two rows in green, the related residuals are shown in Figure 4.5. The same setup with $a_4 = 0.04$, with and without shapelet reconstruction is displayed in purple. The associated residuals are shown in Figure 4.6. The uncertainties on H_0 are calculated using the 0.16 and 0.84 quantiles and the main value is the median of the MCMC H_0 sampling.

4.3.1 Influence of the shear

We compare the modelling of our base case, which is characterised by $\gamma_{\rm ext} = 0.05$ and an orientation of 30° with respect to the SIE major axis, with systems generated without shear. We find that the absence of shear does not significantly change the goodness of the fit, apart from in two specific cases.

As shown in Table 4.1, the general trend is the inability of the shear to absorb deformations introduced by multipoles. This is expected as a fourth-order multipole (i.e. $m = 4$) is an octupolar moment while the shear is a quadrupolar one. However, two mock systems stand out: the discy ones with cusp configurations. For those two cases, we find that good residuals can be achieved. This may be explained by the specific symmetry: the multipole, the SIE, and the source position are aligned, thus creating images in a relatively narrow region with conserved axial symmetry (for the potential, magnification, and deflection). It is thus easier to mimic the effect of input multipole with an SIE+shear in this small symmetric region. In addition, for those two systems, we observe that the fit of an SIE on an SIE+multipole is not equivalent to fitting an SIE+shear on SIE+shear+multipole. The former is not presented in the table but is a good fit, while the latter is a poor fit. This result may appear surprising at first sight as the same additional component (the shear) is added to the mock system and to the model. However, while the lensing potential, deflection, and convergence of the different components sum up linearly, the magnification is not linearly changed, thus explaining the difference between sheared and shearless cases.

4.3.2 Influence of the lens ellipticity

Early-type lensing galaxies generally have axis ratios in the range $q \in$ [0.65-0.95] (e.g. Sluse et al. 2012; Rusu et al. 2016; Shajib et al. 2019). We therefore tried three different axis ratios for the lensing galaxy: a more elliptical galaxy with $q = 0.7$, the base case with $q = 0.8$, and a rounder galaxy with $q = 0.9$. We find that the rounder the galaxy, the poorer the fit (see Table 4.1). This means that the detectability of multipoles is increased when the galaxy is rounder.

The main cause of this effect may be the following: as the ellipticity increases (i.e. q decreases), the size of the inner caustic increases, such that the magnification of a source located at the same relative position with respect to the caustic gets smaller. For a fixed exposure time, this yields a lower effective S/N in the ring, reducing our ability to detect multipole imprints in the lensed host images.

Apart from this general trend, a careful look at Table 4.1 shows that for a small number of cases the fit slightly improved with the increase in q. This may be due to the specific realisation of the noise, and the slight dependence of the results on the position of the source with respect to the caustics. We note that to test the impact of q, we compared systems holding the value of a_4 to 0.01. According to Equation

(4.7), this implies a different value of a_4/a for the different q. Keeping a_4/a constant instead of a_4 constant does not change the increase in χ^2 with the axis ratio q.

4.3.3 Influence of a relaxed slope constraint

Above, we model the lens with an isothermal mass model, which is our fiducial lensing galaxy profile. However, a power law with a free slope is often used in the modelling of real lensing systems. We therefore followed the same fitting procedure using a power-law elliptical mass density profile (PEMD; Barkana 1998) with an additional step in the fitting that allows the slope to be free to vary. A PEMD is characterised by a 3D density profile $\rho(r) \propto r^{-\gamma'}$. This model is equivalent to an SIE for a power-law index γ'=2. See Appendix 4.B.1 for more details.

As can be seen in Table 4.1, a slightly lower χ^2 is obtained when relaxing the slope. However, changing the slope of the modelled profile is not sufficient to absorb the residual patterns due to the multipole. There is therefore no evidence for a degeneracy between the modelled mass density slope of the lens and the input fourth-order multipoles.

The impact of input angular structures on a fitted monopole was recently discussed by Kochanek (2021). He explains how angular structures impact the Einstein ring and, if fit with too simple a model, can either produce large χ^2 or drag the radially fitted model to an incorrect slope. Here we have a true lens mass profile that displays boxyness or discyness and fit it with an elliptical power law and shear. Because the multipoles only weakly change the mass within the Einstein radius, and octupole perturbations of the potential cannot be mimicked by a combination of quadrupolar components (i.e. ellipticity and shear), the freedom allowed to the fitted slope of the power law is not sufficient to absorb the multipole effects.

4.3.4 Influence of a relaxed slope constraint when the mock lens follows a composite mass profile

While we observe in the previous section that relaxing the constraint on the fitted slope does not significantly improve the fit, one may wonder whether or not this is due to the fact that the same family of models, i.e. power law, is used for both the mock image creation and the fit, thus not allowing any possible degeneracy linked to the slope. To test this hypothesis, we created mock lensing galaxies with a composite mass profile comprised of a baryonic Chameleon (Dutton et al. 2011) profile and a Navarro-Frenk-White (NFW Navarro et al. 1996) dark matter component. The Einstein radius of these new lensing galaxies is chosen to be $2''$, as used for our fiducial mock systems. We parameterized our mass profiles such that the lensing galaxy is similar to those observed in massive ellipical lensing galaxies, with a dark matter fraction of 0.32 within the Einstein radius, with an axis ratio $q = 0.8$ constant with

radius, and a slope close to isothermal at the Einstein radius. The complete set of characteristics of our mock profile is given in Appendix 4.B.2 & 4.B.3.

This experiment being mainly an expansion of Section 4.3.3, we display the results of this test separately in Table 4.2. The first row of Table 4.2 contains the results when no multipole is present in the composite lens mass; this is used as a fiducial case to ensure the reference χ^2 is close to one [4]. As already observed, when the input mass profile follows a SIE, the freedom allowed in the fitted slope only slightly improves the χ^2. On the other hand, we also observe that the typical χ^2 obtained with the power-law model is similar when the truth is a composite (Table 4.2, rows 2-3) or a SIE (Table 4.1, rows 6-7).

The ability of the power-law model to fit the composite mock system when a_4=0 demonstrates that the two models are degenerate. The addition of multipoles to the mock lenses leaves the radial profile and Einstein radius unchanged, such that the same region of the radial profile is probed by the host galaxy images. The similarity of the χ^2 obtained with the composite and power-law mock mass profiles is consistent with that interpretation. On the other hand, the similarity between the χ^2 for both the composite and SIE mock systems (with and without multipoles) informs us that the role of the radial mass profile is less important for χ^2 than effects such as modelled source shape freedom (Section 4.3.7) or other input characteristics such as the S/N (Section 4.3.5).

We note that for more complex azimuthal structures, the choice of the radial profile may not be ignored. For example, if we consider a varying ellipticity with radius but the multipole kept constant, we do not exclude the possibility of greater interplay between the radial profile and the azimuthal structures: the imprint of the multipoles on the lensed ring gets stronger for a rounder galaxy, as seen in Section 4.3.2. As a consequence, a mock galaxy displaying varying slope and ellipticity with radius could potentially behave differently from what we have seen here under multipolar perturbations. However, this level of complexity is beyond the scope of this thesis.

4.3.5 Influence of signal-to-noise ratio

Summarising the S/N of images of a lensed system with a single number is a difficult task, as the point source and the extended images need to be accounted for. We therefore opted for a more qualitative criterion based on the exposure length and the brightness of the source. Our base case has an exposure time of 5400s and a very bright source which has an intrinsic brightness of 20.5 mag for the host and 21 mag for the quasar. This translates into integrated lensed magnitudes around 17 (17) mag

[4] We note that the recovered value of H_0 in the absence of multipole is not centred on 70 km s^{-1} Mpc^{-1}. This is mostly due to the mass sheet degeneracy (MSD, Schneider & Sluse 2013). Without kinematics information and modelled light of the lensing galaxy, such degeneracy cannot be broken (Birrer et al. 2020; Birrer & Treu 2021; Chen et al. 2021).

for the four images of the host (quasar). Considering each image separately, the typical mean lensed image magnitude is 18.5 mag. We then reduce the exposure time to 3000 s to match the exposure obtained typically with one orbit of HST. For that exposure time, we consider two intrinsically fainter sources: a first source that has a mean observed magnitude of typically 20.25 mag and another one of 21 mag. Those systems with lower S/N correspond to unlensed quasar brightnesses of respectively 22.75 mag and 23.5 mag, and are referred to as 'bright' and 'faint' source cases below. While this latter case corresponds to a particularly faint quasar image, the corresponding host brightness is sometimes observed in lensed systems (Ding et al. 2021a).

From Figures 4.4 & 4.5 and Table 4.1, we see that there is a clear decrease in the prevalence of the residuals as the data quality decreases. Indeed, the highest S/N fits (our base case, in red in the table) display ubiquitous patterns in the residuals and the χ^2 is always above 1.2. For the 3000s exposure time and bright source case (green in the table), we predominantly see cases for which the multipole imprint is hidden in the noise, but there are a few systems with χ^2 close to 1.2 with light imprints. This is no longer the case for the faint source cases, for which the χ^2 is consistently lower than 1.1.

The exposure time and source brightness are not the only factors that control the S/N, but they provide a reasonable observation-based proxy of the data quality. Other factors, such as the Einstein radius, the contrast between quasar and host, and so on, also influence the S/N, as discussed in Sections 4.3.8 & 4.6.

		cusp_l		cusp_s		fold		cross	
IN: composite,	χ^2	1.00		1.02		1.02		1.04	
no multipole,	H_0	$61.8^{+2.5}_{-1.8}$		$64.8^{+1.9}_{-1.6}$		$65.1^{+2.6}_{-2.1}$		$65.4^{+5.6}_{-4.6}$	
MOD: **free slope**	slope	1.94		1.96		1.97		1.96	
		Boxy	Discy	Boxy	Discy	Boxy	Discy	Boxy	Discy
IN: composite,	χ^2	1.46	1.24	1.61	1.43	1.45	1.28	1.42	1.29
MOD: **fixed slope**	H_0	$62.0^{+2.1}_{-2.2}$	$64.2^{+1.9}_{-2.0}$	$63.6^{+1.4}_{-1.4}$	$65.5^{+1.3}_{-1.4}$	$65.0^{+2.6}_{-2.8}$	$64.8^{+2.6}_{-2.8}$	$62.5^{+4.8}_{-4.6}$	$68.1^{+5.8}_{-5.4}$
IN: composite,	χ^2	1.44	1.18	1.52	1.35	1.43	1.25	1.38	1.22
MOD: **free slope**	H_0	$49.4^{+1.7}_{-2.2}$	$83.5^{+2.5}_{-2.5}$	$50.1^{+1.2}_{-1.3}$	$85.6^{+1.8}_{-2.0}$	$60.0^{+2.1}_{-2.3}$	$73.9^{+3.0}_{-2.9}$	$53.8^{+4.8}_{-4.3}$	$84.0^{+6.6}_{-5.2}$

Table 4.2: Results of the experiments performed in Section 4.3.4.

Notes. The mock systems follow the base case with $\gamma_{\rm ext}$ = 0.05, q = 0.8, 5400 s exposure time, and a very bright source ($\langle m_{\rm QSO}\rangle$=18.5 mag), but differ by the main lens mass profile which is a composite mass profile made of a baryonic component and a dark matter component, instead of being a SIE. The case represented in the first row is multipole free while the two bottom rows display a multipole $a_4 = 0.01$, either in discy or boxy orientation. The mock images are fitted with a power-law model (hence the **bold** characters to differentiate it from the base SIE modelling, following the conventions of Table 4.1) with either a free slope or a fixed slope. In the latter case, the fixed value is the value retrieved in the no multipole case for each configuration.

4.3.6 Influence of the multipole strength

To characterise the dependence of the fit on the input multipole strength, we created mock mass profiles for four additional values of $a_4 \in [0.01, 0.05]$. Figure 4.1 provides a visual representation of the induced deviation from a pure elliptical profile. As the residuals for $a_4 = 0.01$ for our baseline setup have already been detected, we chose to vary the strength of the multipole for our second setup corresponding to an exposure time of 3000s and a bright source (see Section 4.3.5). The latter case with $a_4 = 0.01$ is shown above in Figure 4.5 and by the green line in Table 4.1. If we convert the multipole convention of Hao et al. (2006) (Equation (4.7)) to our notation, we see that 70% of the galaxies of their sample have $a_4 < 0.02$ and only 4% of their sample have $a_4 > 0.05$ (see Figure 4.2). The low multipole cases ($a_4 \leq 0.02$) are therefore the most likely to be representative of a real sample of galaxies, while the case $a_4 = 0.05$ should be seen as a rare extreme situation that could plausibly happen in a large sample (typically 100) of time-delay lenses. We may note that boxy and discy galaxies are not evenly distributed, with 64% of the sample by Hao et al. (2006) being discy. However, the relative rate of boxyness or discyness is also found to depend on the galaxy mass or brightness (Hao et al. 2006; Kormendy et al. 2009; Mitsuda et al. 2017).

As one would expect, it is less easy to achieve a good fit as the multipole strength increases (see Table 4.1). More precisely, if we assume a threshold of $\chi^2 = 1.2$ to distinguish between poor and good residuals, multipoles get detected above a_4=0.03 for discy galaxies while $a_4 = 0.02$ is the detection limit for boxy galaxies.

4.3.7 Influence of complexity in the modelled source

When modelling real systems, the extended source is hardly ever modelled as one simple light profile (e.g. Birrer et al. 2016, 2019). Most of the time, the source is either pixelised with regularisation applied (Brewer & Lewis 2008; Suyu & Halkola 2010; Nightingale & Dye 2015; Galan et al. 2021) or analytical with a main simple profile plus a set of basis functions, such as shapelets, that are designed to capture morphological host complexity beyond axisymmetry (Birrer et al. 2015, 2016; Birrer & Amara 2018; Birrer et al. 2019; Shajib et al. 2019). Above, we model the source with a circular Sersic profile because we know that this is its true input profile. However, more flexibility in the source should be allowed, as in state-of-the-art modelling of strongly lensed quasars. Due to our choice of modelling software, we chose to add shapelets to the source (as e.g. Birrer et al. 2016, 2019; Shajib et al. 2019). We performed an extra step in the fitting procedure of all the systems presented in the previous sections, adding shapelets to the source with maximal polynomial order $n_{\max} = 5$.

As shown in Table 4.1, the improvement when shapelets are added in the source is ubiquitous. When the fit is already good without shapelets, that is, typically cases with $a_4 = 0.01$ for the bright source, there is only a slight improvement of the χ^2. When the fit without shapelets displays large residual features, that is, typically when $\chi^2 > 1.2$,

the improvement introduced by shapelets is more significant, as illustrated in Figure 4.6. The retrieved source is generally more structured than the input circular one but is not unphysical (e.g. the source surface brightness remains positive).

The approximate degeneracy between the source morphology and the main lens potential is likely an expression of the source position transformation (SPT; Schneider & Sluse 2014; Unruh et al. 2017; Wagner 2018; Wertz et al. 2018). Additional complexity in the source can compensate for complexity in the lensing potential, which has further-reaching effects in general than the specific exploration of multipoles in this work. In practice, the complexity of the source is unknown, but it could be informed using a sophisticated prior that emulates the known morphologies of host galaxies. As an example, the dark spots in the source reconstructions for our fits may be mathematically acceptable (in the sense that they have non-negative brightness values), but the human eye can recognise them as being unusual and may suspect that they are instead absorbing the complexity of the potential. With no straightforward way to quantify and implement this human intuition (or certainty as to whether it can always be trusted), identification of whether or not the source reconstruction corresponds to the intended quantity is a difficult task.

With our tests, we find that shapelet reconstruction can absorb some of the multipole complexity. However, one could also wonder whether or not allowing even more freedom in the source could absorb any additional imprint of lens complexity. While answering this question is not the main purpose of this work, we concisely explored two different ways of allowing more complexity in the source: allowing ellipticity in the Sersic source, and allowing shapelets with a maximal polynomial order of eight instead of five (both maximal orders were investigated in Birrer et al. (2019)). After testing a few 'extreme cases' with $\chi^2 > 1.3$, we found that the ellipticity in the source cannot compensate the lensing potential complexity. The improvement of the fit thanks to this new degree of freedom is negligible. On the other hand, shapelets up to order $n_{\max}$ =8 yield a substantial improvement of the χ^2 compared to the fits obtained with $n_{\max} = 5$. Indeed, for the last row of Table 4.1, five of the eight mock images can be fitted with $\chi^2 < 1.2$ with $n_{\max} = 8$, while only two of the eight good fits can be obtained with $n_{\max} = 5$. This improvement in the image residuals comes at a cost in the source plane, namely the appearance of clumpy structures in the source that may hopefully be identified as unrealistic (see Appendix 4.A). In summary, the freedom in the source reconstruction helps to absorb some of the multipole complexity, but it seems that the associated distortion of the source may not systematically mimic structures that exist in real galaxies. Future work is needed to more thoroughly explore the constraining power and limitations of an arbitrary number of shapelets.

4.3.8 Other influences

Apart from the factors explored in the previous sections, there are yet other ingredients that could influence the detectability of multipoles, such as the Einstein radius, the source intrinsic shape, and the lens light contamination. We did not systematically quantify their impact, but we explain their influence qualitatively.

As the Einstein radius gets smaller, the different images of the same background source are brought closer together and can easily overlap, especially in cusp cases. The extended source images consist of fewer pixels and the quasar images, with the PSF spreading their light and covering the ring, dominate most of the flux. As the multipolar component is visible in residuals mainly thanks to the host flux, having less host pixels reduces the ability to detect imprints from multipole perturbations. This effect can even be stronger than a change of S/N as performed in Section 4.3.5. However, precisely quantifying the role of the Einstein radius remains difficult as the detectability of multipolar structures in the ring becomes much more dependent on the lensed-images configuration, source shape, PSF extension, and contrast for smaller Einstein radii.

Similarly, if the contrast increases between the extended host flux and the quasar flux (i.e. the host is fainter for a given quasar magnitude), the multipolar components are less detectable at fixed exposure time. In addition, the source radial profile also plays a role: as the host displays a shallower profile (decrease of $n_{\rm sersic}$), the total brightness is the same but the host is more rapidly lost in the noise. This therefore decreases the total S/N in the host flux and the multipole is less detectable. Following the same lines, if a source is larger (i.e. increase of $R_{\rm sersic}$) and keeps the same magnitude in the source plane, the host image spreads over more pixels with less flux in each, also decreasing the S/N in the ring. A concrete example of the influence of the source radial shape on the S/N is given in Section 4.6. We did not explore the influence of the source azimuthal shape (e.g. an elliptical source). We expect the effect to be less straightforward than a change in $n_{\rm sersic}$ or $R_{\rm sersic}$. We anticipate a complex dependence of the multipole detectability on the orientation of the source relative to the caustics.

In our analysis, we considered a transparent lens (i.e. no lens light). However, the presence of the lens light may have two different effects. First, the lens light and the source images can be blended, making it difficult to resolve the two components: part of the flux attributed to the lens might in fact come from the host images perturbed by multipoles in the lens mass. To avoid blending issues between source and lens light, it is common to use images of the same lens system in different spectral bands (Shajib et al. 2019). We did not simulate any lens light in our analysis and therefore did not test the efficiency of multiband imaging to mitigate the potential issue arising from blending either. Second, the lens light in itself could potentially help in detecting multipole presence as multipolar components in the mass are linked to those in the light. The detectability of multipole in the lens light profile is discussed in more detail

in Section 4.3.9. The above list may not be exhaustive, but encompasses the main sources of effects that could affect the results presented in this work.

4.3.9 Detectability in real lens systems

We see in the previous sections that several factors influence the goodness of the fit of our mock images. For the highest quality data, the imprint of the multipole on the lensed images is ubiquitous. However, there are circumstances where the multipole imprint can remain hidden, such as if shear is absent and the main axes of both the ellipticity and multipole are aligned with the source position. Multipole perturbations are also more difficult to detect in galaxies with a higher ellipticity (i.e. small axis ratio). Leaving the mass profile slope to vary improves the residuals but only slightly, even when the true input mass profile slope varies with radius. The S/N on the other hand is crucial for detecting multipoles: with low S/N, the multipole contribution can be totally concealed in the noise. Of course, it also depends on the strength of the multipole contribution and on the freedom allowed in modelling the source, for example using a shapelet basis on top of an analytical model. Other factors such as the contrast, the source radial profile, or the Einstein radius also add more complexity to the problem.

Overall, the different factors that can increase or decrease the detectability of multipoles combine together and create a unique lensing system each time. It is not possible to characterise each system with a single number that would reflect its robustness to multipole detectability because it depends on so many parameters. However, it is possible to compare a system to our three different S/N levels. For our three S/N levels as defined by exposure time and source brightness, we essentially find three tiers of multipole detectability: 1. multipole will never go unnoticed in the residuals, 2. multipole can go unnoticed if it is at a low level or absorbed through freedom in the source structure, and 3. multipole will nearly always go unnoticed. However, exposure time alone is not a complete descriptor of these thresholds, because a lens with for example a lower exposure time but a brighter extended source relative to the quasar (or larger Einstein radius, as another example) will mimic a higher level of multipole detectability. Consequently, in order to accurately quantify the detectability of multipoles in a given system, the system must be precisely emulated so as to classify it in one of the described tiers.

A complementary path that can be followed to assess the role of multipoles in the model is to search for evidence of Fourier modes in the luminosity profile of the lens. Mitsuda et al. (2017) and Pasquali et al. (2006) demonstrated that multipolar perturbation of the light profiles can be measured in elliptical galaxies at redshifts similar to those of lensing galaxies. It is *a priori* less clear whether or not such a measurement is feasible in lensing galaxies for which the lens light is blended with the light from the lensed images. To assess the feasibility of such a measurement in lensed systems, we

used $F814W$ HST and K-band AO images of the lensed quasar QSO J1131-1231 (Sluse et al. 2003; Suyu et al. 2013; Chen et al. 2016). While the large Einstein ring ($\theta_E \sim 1.8''$) and bright lensing galaxy may ease the detection of multipoles in the lens, the lensed images are particularly bright with features extending down to the very inner region of the lens (see e.g. Figure 4 of Claeskens et al. 2006). This makes this system a good test case. We performed multipole measurements on the images subtracted from the best ring model published by Suyu et al. (2013) and Chen et al. (2016) using two different techniques. First, we fitted ellipses with fourth-order Fourier components using the Python package `photutils`. The results obtained on HST and AO data are compatible with each other for radii $0.4 < \theta < 0.9''$. They suggest a mean value of $a_4 < 0.02$. At radius $\theta < 0.4''$, there is an insufficient number of pixels to enable any sensible measurement. At radius $\theta > 0.9''$, the residuals from the PSF and/or lower S/N in the lens prevented the algorithm from converging. For AO data, measurements were possible up to $\theta = 2''$, confirming $a_4 \leq 0.02$. We used a second method consisting in fitting the full lens intensity profile with a Sersic model using `galfit` (Peng et al. 2010), but including a fourth-order Fourier mode to describe the azimuthal profile of the lens. While the fit of a single Sersic profile provides a poor description of the profile in the inner regions of the lens (see e.g. Claeskens et al. 2006), the amplitude $a_4 = 0.01$ agrees for the two data sets. However, the same is not true for ϕ_4 which is offset in the two data sets by 30 deg. We may note that these values of a_4 do not appear unrealistic from visual inspection of the images, as $a_4 > 0.04$ are easily detectable by eye in good S/N data, but no deviation from a perfect ellipse is apparent. In summary, this test demonstrates that a measurement of a_4 in the light of lensing galaxies may be feasible in high-resolution images, but more work is required to assess the amplitude of systematic errors in such a measurement.

Finally, we note that we did not test the inclusion of multipoles in the lens mass model. This is an alternative path that could also be explored, but is beyond the scope of this thesis.

4.4 Impact on H_0 inference.

We show in the previous section that azimuthal perturbations of the potential, if present, could remain unnoticed in lensed images. Importantly, those perturbations can be absorbed in the lens and/or source parameters, which then differ from their true values. In this section, we quantify their impact on the value of H_0 inferred from those (biased) models. While the goodness of the fit was the main topic of the previous section, we discuss here those results in terms of the H_0 inference.

4.4.1 At a single-galaxy level

During our systematic tests shown in Table 4.1, the inferred H_0 values range typically between 60 and 80 $\mathrm{km\,s^{-1}\,Mpc^{-1}}$ while the fiducial value is 70 $\mathrm{km\,s^{-1}\,Mpc^{-1}}$. We disregard the results obtained for models yielding a poor χ^2, as we consider that those models would not be included in a subsequent analysis. We also disregard the tests from Table 4.2 because the results are redundant with those of Section 4.3.3 already present in Table 4.1. Figure 4.7 summarises the inferred H_0 values obtained for $\chi^2 < 1.2$. All the cases listed in Table 4.1 fulfilling this criterion are included but we exclude duplicates. Specifically, we consider only once the coloured rows that appear multiple times in the table and only the shapelet reconstruction for the cases with 3000s exposure time and a bright source. In our sample, the discy and boxy galaxies do not behave in the same way: the discy galaxy models display values of H_0 of around 70 $\mathrm{km\,s^{-1}\,Mpc^{-1}}$ and above; while the boxy ones show H_0 values with an extended tail below the fiducial H_0. If we consider only fits with $\chi^2 < 1.1$, the same trends are observed. As our sample is neither homogeneous nor highly representative of a galaxy population, Figure 4.7 is not the distribution of H_0 we would have derived if the value of a_4 of the lensing galaxies were randomly drawn from the distribution observed in a population of elliptical galaxies. However, each H_0 inference is representative of a possible elliptical galaxy.

We may now wish to quantify the impact of multipoles on H_0 when considering a population of lens systems. For this purpose, we first need to quantify the probability of having lensing galaxies deviating from a pure elliptical profile. For this purpose, we need first to identify if there is any evidence for a dependence on a_4 on the galaxy luminosity, mass, environment, and/or whether a_4 varies as function of the galactocentric radius and of the redshift. We look at those various aspects in the following (Sections 4.4.2 & 4.4.3).

4.4.2 The a_4 distribution for elliptical galaxies

Hao et al. (2006) studied the light of 847 galaxies at redshift $z < 0.05$. They found that boxy galaxies tend to be bigger and brighter than discy ones and that discy galaxies are more abundant, with abundance ratios depending on the magnitude cutoff. The boxy galaxies are also more likely to be found in denser environments compared to discy ones. This corroborates the findings of Bender et al. (1988, 1989) in several ways, except that the latter found equivalent abundances of boxy and discy galaxies. A search for a redshift evolution of a_4 was performed by Pasquali et al. (2006) and Mitsuda et al. (2017). Pasquali et al. (2006) studied a small sample of 18 galaxies with $0.5 < z < 1.0$ and found more discy galaxies but suggested that this might be due to their limited sample. They corroborate previous findings that discy galaxies have higher ellipticities while boxy galaxies are more luminous, wider, and less elliptical in general. Pasquali et al. (2006) also found that the galaxies in their sam-

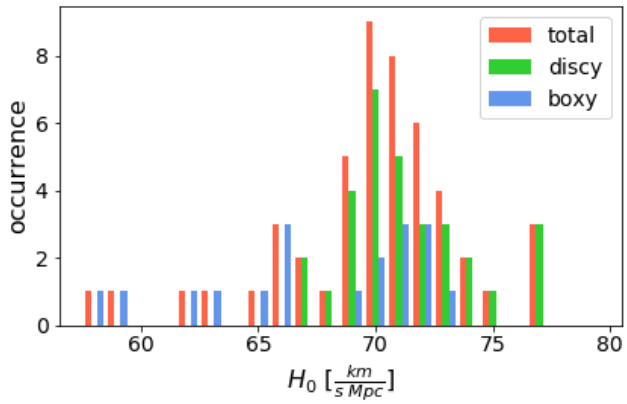

Figure 4.7: Median H_0 inference for mock systems from Table 4.1 with $\chi^2 < 1.2$ (see text for more information).

Notes. The histogram for boxy galaxies is displayed in blue, that for discy ones is in green, and the sum of both is in red. The histograms are representative of the retrieved H_0 values obtained in our systematic tests that encompass multipole amplitudes of plausible lenses. However, this does not represent an inferred H_0 distribution from a realistic population of lenses (see Figure 4.9).

ple are similar to the ones at $z = 0$ and only a possible trend in a_3 with redshift was observed. Mitsuda et al. (2017) extended this work by studying 130 galaxies at $z \sim 1$ and 355 at $z \sim 0$. These authors found, independently of the redshift, that galaxies showing a_4 contributions are very common and that discy shapes are favoured for galaxies with $log(M_*/M_\odot) < 11.5$, while the boxy galaxies start to dominate at higher masses. Mitsuda et al. (2017) also looked at the a_4 radial profile of the disc-shaped NGC4697 in more detail: in the innermost region, the a_4 parameter is more uncertain and in some filters switches to a boxy profile. For the other parts of the galaxy, the a_4 is more or less constant with radius. The change of a_4 with galacto-centric radius has been studied more extensively by several authors (e.g. Rest et al. 2001; Kormendy et al. 2009; Krajnović et al. 2013). The first two authors studied the largest sample of elliptical galaxies. They find a great diversity in a_4 variation with radius. A profile can be boxy in the centre and discy in the outskirts, or be relatively constant or even display a monotonic increase or decrease. Discyness or boxyness can therefore exist at the regions encompassed by typical Einstein rings, that is mostly the region within 1 - 2 effective radii. In summary, at redshifts, masses, and ellipticities of galaxies considered for lensing, the presence of galaxies with nonzero boxyness or discyness is common.

As the mass is not directly observable, we need to rely on numerical simulations to quantify the presence of such structures in the mass distribution. No authors have yet reported the presence of a_4 components in the total mass distribution, that is both stars and dark matter. However, the stellar mass dominates at radii $\lessapprox R_{Ein}$, and the studies focusing on multipolar components in the sellar mass are thus relevant for our purpose. Penoyre et al. (2017) studied stellar mass distribution in the Illustris simulations (Vogelsberger et al. 2014b) and found a few galaxies with clear boxyness and discyness but could not conclude on precise a_4 measurements due to too low spatial resolution. Frigo et al. (2019) presented 'zoom' simulations and studied the boxyness and discyness of their sample more thoroughly. They did not find clear boxyness in their sample. They found systematic discyness if the galaxies are viewed edge-on. When seen at random orientations, the galaxies are still systematically discy but with lower a_4 values. The AGN feedback in their simulations tends to create less azimuthal structures at $z = 0$ while the AGN influence is not predominant at $z = 1$ where both AGN and no-AGN cases presented discyness, especially for more elliptical galaxies.

In summary, we do not find any evidence for multipoles to be less prominent in galaxies characteristic of lensing galaxies, namely galaxies with high mass and z > 0.2, than in close-by galaxies. In conjunction, we see that for a single galaxy, realistic amplitudes of the multipoles can introduce a bias on H_0 (Figure 4.7). In the following section, we quantify the impact of multipoles on H_0 derived from a population of lensing galaxies.

4.4.3 At the population level

In this section, we use our mock systems and a plausible distribution of a_4 to quantify their influence on the inferred distribution of H_0 from an ensemble of lens systems. First, we repeat the H_0 inference for values of a_4 in the range $[0.00, 0.05]$ [5], a fixed axis ratio q=0.8, and the three different levels of S/N obtained by modifying the exposure time and source brightness (see Section 4.3.5). This way, we expect to cover a representative range of S/N achievable in observations. As explained in Section 4.3.9, those three S/N levels are more broadly representative of three tiers of multipole detectability (almost always detectable; sometimes detectable; almost never detectable).

We then proceed to the fit of those mock systems with an SIE+shear model, as outlined in Section 4.2.3. When the fit is not good enough, that is when $\chi^2 > 1.2$, we add shapelets in the source light. Results are displayed in Figure 4.8 (considering only cases with $\chi^2 < 1.2$). As already seen in the previous section, poor fits are generally obtained for the highest S/N considered, such that only a few cases appear on the figure. The inferred value of H_0 tends to be underestimated when the galaxy is boxy and overestimated when discy. Moreover, the lower the S/N, the larger the spread in

[5] We note that systems with $a_4 = 0.00$ are only created once instead of twice for different ϕ_4: they are valid for both discy and boxy statistics.

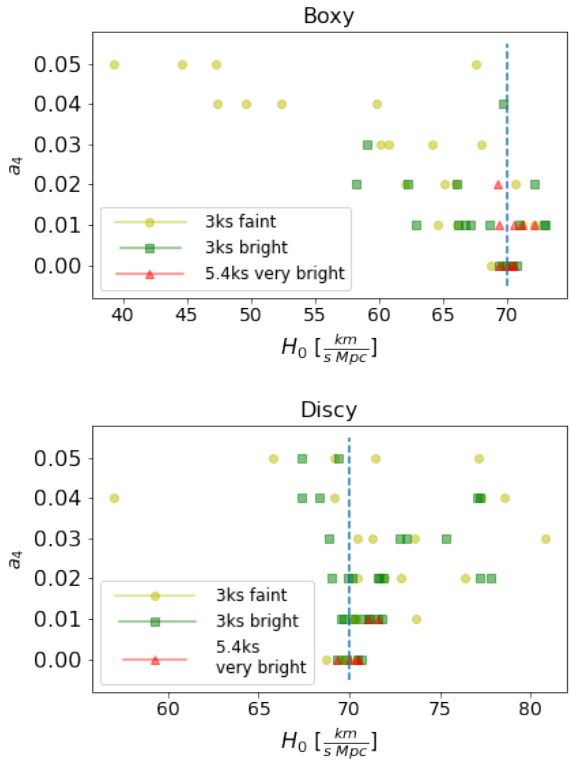

Figure 4.8: H_0 inference from mock systems created with different a_4 and different S/N

Notes. yellow circles : 3000s faint source ; green squares: 3000s bright source ; red triangles : 5400s very bright source. The boxy and discy cases are in the top and bottom panels, respectively. The typical uncertainties representing the 0.16 and 0.84 quantiles are displayed in the legend. The fiducial H_0 is 70 $\mathrm{km\,s^{-1}\,Mpc^{-1}}$ and is represented with the blue dashed line.

the H_0 inference. We note that the typical uncertainties reported in Figure 4.8 being the mean of the 68% credible intervals, not only strongly depend on the S/N but also on the configurations: cross configurations yield uncertainties roughly twice as large compared to the other configurations. Thus, having more (less) good fits for crosses will lengthen (shorten) the final typical error bars.

To forecast the distribution of values of H_0 for a population of discy and boxy galaxies similar to known early-type galaxies, we combine the results from Figure 4.8, weighting each data point based on the distribution of a_4 derived by Hao et al.

(2006) (Figure 4.2). The distribution of a_4 is discretized into six bins: the bin with $a_4 \leq 0.005$ contains 10% of the sample, the $0.005 < a_4 \leq 0.015$ bin contains 46%, the $0.015 < a_4 \leq 0.025$ bin takes 21%, the one with $0.025 < a_4 \leq 0.035$ contains 10%, the $0.035 < a_4 \leq 0.045$ bin contains 6%, and the $0.045 < a_4 \leq 0.055$ bin contains 3%. We neglect the rare systems with a_4>0.055. For each bin, the probability density function (PDF) is the average of the different PDFs associated to each point on the graph showing a_4 versus H_0 (Figure 4.8) for a given type (boxy or discy) and a given a_4 value. Those PDFs are then weighted with the probability of encountering the a_4 value and by the fraction of discy and boxy galaxies assumed in the sample. The final PDF is thus

$$\mathrm{PDF}(H_0) = \sum_{i=1}^{6} \mathrm{PDF}(i) \times \mathrm{w}(i), \tag{4.8}$$

where i is the index corresponding to the a_4 bin, PDF(i) is the associated PDF for each a_4 bin and type (boxy or discy), and w(i) is the weight associated to each a_4 bin multiplied by the relative fraction of boxy and discy galaxies. In Hao et al. (2006), discy galaxies represent 64% of the sample while 36% of it are more boxy. However, Mitsuda et al. (2017) show that the fraction of boxy/discy galaxies depends on the stellar mass of those galaxies. When $\log(M_*/M_\odot) > 11.5$, boxy and discy galaxies are equally observed. The results for the two relative distributions of boxy and discy galaxies are reported in solid lines in Figure 4.9 and the median and 68% credible intervals are written in Table 4.3 in the H_0 columns. Those distributions correspond to the underlying H_0 distributions from which samples are drawn. In other words, from a sample of n lensing galaxies, one is expected to infer n independent measurements of H_0 that would follow the observed distribution.

Because boxy and discy galaxies have opposite impacts on the inferred value of H_0, the final distribution is overall unbiased at the subpercent level. This result is independent of the value of the S/N considered. However, by increasing the fraction of boxy galaxies, we see that the distribution is slightly driven to lower values of H_0 by less than 1%. The larger scatter on H_0 when the S/N decreases is mainly due to the larger uncertainty for a fixed value of a_4 which is stronger for lower S/N, especially for high multipolar deformations.

Beyond bias, a noise term due to multipole presence is expected. If we consider that a multipole introduces an uncertainty on the measurement of H_0 that is independent from the other sources of uncertainty, that is when no multipoles are present in the lensing galaxy, we can calculate the multipole contribution to the total uncertainty budget. Indeed, we have

$$\sigma^2_{\text{multipole}} = \sigma^2_{\text{tot}} - \sigma^2_{\text{no multipole}}, \tag{4.9}$$

where σ_{tot} is the total uncertainty quoted in Table 4.3, $\sigma_{\text{multipole}}$ is the contribution from the multipoles, and $\sigma_{\text{no multipole}}$ is the uncertainty when modelling images with a multipole-free lensing galaxy.

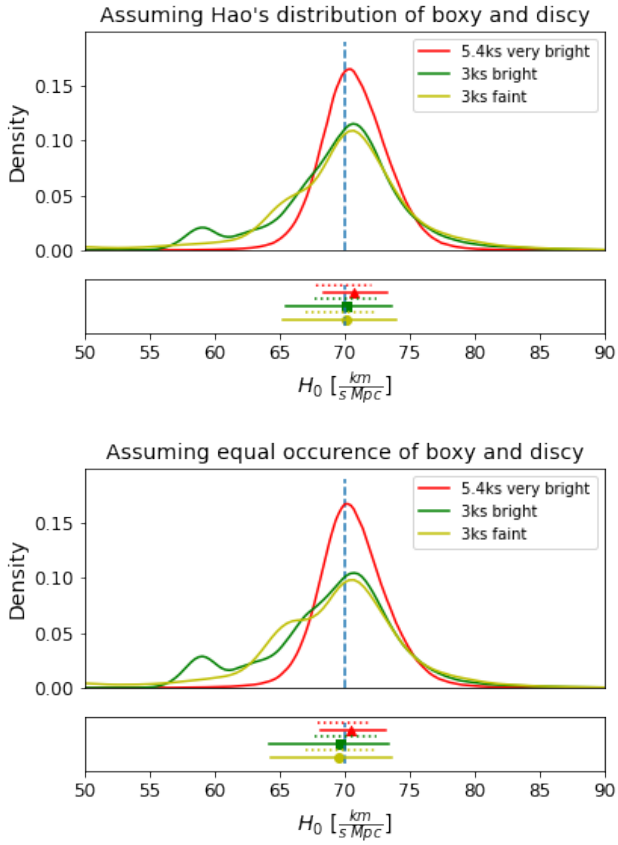

Figure 4.9: Underlying distribution of H_0 for different S/N.

Notes. H_0 distributions for our base case (5400s, very bright source) (red), and for 3000s bright (green) and faint (yellow) sources. Each panel corresponds to two different fractions of boxy and discy galaxies (top: 36% boxy, 64% discy, as reported in Hao et al. (2006) ; bottom: 50% boxy, 50% discy). The corresponding median and 68% credible interval are displayed below in solid lines. The dotted lines are the 68% credible interval for the multipole-free distribution. It can be seen in this figure, as well as in Table 4.3, that the presence of multipoles becomes a significant source of uncertainty for lower S/N.

	Hao's ditribution			50/50 distribution		
	H_0 [$\mathrm{km\,s^{-1}\,Mpc^{-1}}$]	$\sigma_{\text{multipole}}$ [$\%H_0$]	$\sigma_{\text{no multipole}}$ [$\%H_0$]	H_0 [$\mathrm{km\,s^{-1}\,Mpc^{-1}}$]	$\sigma_{\text{multipole}}$ [$\%H_0$]	$\sigma_{\text{no multipole}}$ [$\%H_0$]
5400s very bright	$70.7^{+2.6}_{-2.4}$	1.7%	3.0%	$70.5^{+2.7}_{-2.3}$	2.0%	2.9%
3000s bright	$70.1^{+3.5}_{-4.6}$	4.7%	3.4%	$69.7^{+3.7}_{-5.5}$	5.6%	3.4%
3000s faint	$70.2^{+3.8}_{-4.9}$	4.9%	3.8%	$69.6^{+4.0}_{-5.2}$	5.4%	3.9%

Table 4.3: H_0 distributions from Figure 4.9

Notes. H_0 distributions for the different S/Ns and the two different fractions of boxy and discy galaxies. left: 36% boxy, 64% discy, following Hao et al. (2006) ; right: 50% boxy, 50% discy. For each distribution, the median H_0 and its 68% credible interval are given in $\mathrm{km\,s^{-1}\,Mpc^{-1}}$ on the left, the specific contribution from the multipole to the error budget calculated as in (4.9) expressed as a percentage of the median H_0 is displayed in the middle, and that from multipole-free lensing galaxies is displayed on the right. More specifically, the $\sigma_{\text{multipole}}$ and $\sigma_{\text{no multipole}}$ are the mean values of the two sides of the 68% credible intervals.

The $\sigma_{\text{no multipole}}$ is obtained by summing the PDFs of the $a_4 = 0.00$ case with the different configurations weighted by the occurrence of each lens configuration in the calculation of the total PDFs (in Table 4.3 or Figure 4.9). As a cross would have an uncertainty larger than a cusp or a fold, it is important to weight the configurations to calculate a multipole-free PDF that mimics the one with multipoles because, for example, for the highest S/N, not all configurations yield a sufficiently good fit. We find, for equal occurrence of boxyness and discyness (right panel of Figure 4.9 and Table 4.3), that the multipoles introduce around 2% random uncertainty on the H_0 distribution (i.e. $\sigma_{\text{multipole}}/H_0 = 0.02$) for the highest S/N considered, and above 5% for the lower S/N. If instead we consider a distribution of multipole values similar to Hao et al. (2006) (left panel of Figure 4.9 and Table 4.3), the relative uncertainty on H_0 due to multipoles drops below 2% in the highest S/N case, and is between 4.5% and 5% for the two other S/N cases. In the lower S/N cases, multipoles constitute the dominant source of uncertainty on H_0 (i.e. $\sigma_{\text{multipole}} > \sigma_{\text{no multipole}}$).

We note that we did not weight our sample by the occurrence of the different configurations in real lensing systems. By systematically trying to fit the four configurations, that is the two cusps, the fold, and the cross, we aim at encompassing all possibilities. However, in real cases, some configurations might be more likely than others, and those occurrences may also change from one sample to another. We did not take into account this effect but we are confident that the effect is negligible in terms of systematic bias at a population level. However, it may modify the exact value of the uncertainty on H_0.

4.4.4 Impact for the TDCOSMSO analysis

The TDCOSMO/H0LiCOW collaboration combined the results of seven lenses to make their H_0 inference (Wong et al. 2020; Birrer et al. 2020). Those seven lenses were imaged in one or more spectral bands, usually including the F160W/WFC3 HST band with exposure times varying between 2000s and 26000s. Those NIR images are *a priori* the most favourable for analysing extended lensed features (see discussion in Section 4.2.2), which are the most prone to deformation from boxyness or discyness. Their Einstein radii range between $0.8''$ and $2''$ (Birrer et al. 2020). The host galaxies are sometimes significantly brighter than the quasar (e.g. the contrast in RXJ1131, whose host is brighter than the quasar by 0.9 mag, which is stronger than what we considered in this study, i.e. a 0.5 mag difference) and sometimes the quasar dominates the source flux (e.g. WFI2033 with its quasar being 1.5 mag brighter than the host; Ding et al. 2021a). Overall, the TDCOSMO systems are generally very bright, with very high-quality data. For most of the TDCOSMO lenses, we expect large-amplitude multipoles to be detectable if present, and thus to have an unbiased H_0 inference already at a single-galaxy level. However, a detailed analysis for each lens is needed to assess the exact detectability of multipoles and its potential impact on the H_0 inference for

a given lens. Doing so is possible by creating a mock of each system with increasing values of a_4, as done in Section 4.2, to see the multipole threshold at which patterns in the residuals are detectable. By combining this with an analysis of the light of the lensing galaxy, it is possible to assess a range of plausible values of a_4, and to quantify how they may impact the H_0 inference.

As a population, the seven lenses should yield an unbiased combined inference of H_0: their sample is drawn from distributions centred on the true H_0 at a subpercent level (see Figure 4.9 and Table 4.3). Indeed, considering the TDCOSMO data quality, we conceive that for most lenses, the multipoles are detectable (typically, red or sometimes green curve in Figure 4.9). Hypothetically, assuming the worst-case scenario —that the multipole were not ever detectable (yellow curve in Figure 4.9)— as long as the lenses are typical of the elliptical population (i.e. with balanced quantity of boxy and discy galaxies and with a typical distribution of a_4 as in Hao et al. (2006)), the bias on H_0 would still be below the percent level (albeit with increased scatter).

We note that in the TDCOSMO sample, the different single-galaxy inferences are combined by multiplying their PDFs to find the underlying true H_0 and the error on this measurement. The distributions we present in this work (Figure 4.8) are the underlying distributions of H_0 from which a sample will be drawn. Thus, the uncertainties reported in Table 4.3 are the underlying distribution width, not the error one would get by combining x independent H_0 inferences from x lenses (the combined inference being increasingly precise as more lenses are included). The uncertainties on the combined H_0 inference quoted in the TDCOSMO analysis (Wong et al. 2020; Birrer et al. 2020) already take into account any broadening due to the possible presence of multipoles.

4.5 Conclusion

State-of-the-art lens modelling generally assumes that the projected mass density of lensing galaxies follows a perfect ellipse or a combination of elliptical baryonic and dark components. However, boxy or discy isophotal profiles, also referred to as fourth-order multipoles, are observed in massive elliptical galaxies. While the amplitude of those multipoles is unknown for the total mass distribution, lensing galaxies are baryon-dominated in their inner regions. It therefore seems reasonable to assume that the results of studies investigating boxyness and discyness in the light of galaxies are also applicable to the mass of lensing galaxies.

In this Chapter, we investigated how deviations in galaxy morphology from a pure ellipse modify extended lensed images and become detectable when considering full lens image information. For this purpose, we built an ensemble of mock lensed images of a quasar and its host galaxy quadruply imaged due to strong lensing by a galaxy that is almost a singular isothermal ellipsoid (SIE): to mimic discy or boxy mass density distributions, we perturbed this density profile by adding fourth-order multi-

poles with amplitudes matching those detected in the light. Image quality typical of the one achieved with the WFC3 camera on board the Hubble Space Telescope was considered. We then fitted the mock images without any multipolar components.

As our base case, we create a mock image of a very bright QSO+host source with a long exposure time similar to what has been achieved for time-delay cosmography lensed systems. The source we consider is a circular Sersic lensed by an SIE with an Einstein radius of $2''$, with moderate ellipticity ($q = 0.8$) and small multipole perturbation $a_4 = 0.01$. This multipole amplitude is barely detectable by eye, and is typical of what is generally measured in the light profile of elliptical galaxies (a_4 <0.02 is expected for 70% of the systems according to Hao et al. (2006)).

The fitting of this base case showed substantial residuals, suggesting that multipoles, when present, leave ubiquitous imprints in extended strongly lensed images. However, we show that various parameters may influence that detection:

- When the SIE, the multipole, the source position, and the shear are aligned, the imprint of the multipoles on the ring can be absorbed in the modelling by a combination of ellipticity and shear.
- Rounder lensing galaxies will create images that are more sensitive to the presence of multipoles.
- The freedom allowed in the lens mass model with a varying power-law slope only slightly decreases the patterns present in the residuals, independently of the family of models used for the input mass profile.
- Allowing for a structured source luminosity by means of shapelets can absorb substantial residuals coming from the multipoles.
- Naturally, the S/N plays a role: the lower the S/N, the more easily patterns in the residuals are hidden.
- Other parameters, such as the Einstein radius and the host–quasar brightness contrast, may decrease(increase) the detectability of multipoles depending on the host–quasar image blending.

We looked at the impact of the multipole on the H_0 retrieval when the model residual is compatible with the noise. We see that boxy and discy galaxies do not have the same impact on H_0: the boxy galaxies tend to bias H_0 low, while the discy galaxies mostly bias H_0 high. In both cases, H_0 can be biased by several percent for a given system. However, if we consider a sample of lenses with multipolar contributions drawn in a way that is representative of what is observed in the light of galaxies, high multipolar contributions are less probable and the mix of both boxy and discy galaxies tends to reduce the bias to a level of below 1%. However, we note that a specific

selection of lenses may bias the final H_0 inference if for example only boxy galaxies are used. The S/N of the images will mainly broaden the final H_0 distribution.

On a lens-by-lens basis, an upper limit on the bias on H_0 cannot be given without performing a simulation that thoroughly emulates the specific characteristics of a given lens. For a given modelled lensing system meant to be used for cosmological inference on its own, this can be performed by following the methodology presented here, creating a mock of the system and adding multipoles to it in order to assess the threshold at which multipoles are detectable in the residuals. In addition, one can also look at the lensing galaxy light profile. Multipoles in the light can in principle be used as a proxy to the presence of multipoles in the total mass, with the caveat that the presence of multipoles in the dark matter is unsettled.

However, instead of looking at the bias for each system individually, one can consider a population approach. If using a wide sample of lensing galaxies displaying multipolar distribution representative of what is observed in the light of elliptical galaxies, we show that the combined H_0 should not be biased by the presence of multipole structure. This is also true for the TDCOSMO data. Our results suggest that thanks to the high quality of those data, and the ability of the models to reproduce them down to the noise, the bias on the combined H_0 inference from the seven lenses of TDCOSMO is expected to be below the 1% level. Furthermore, the uncertainties quoted in published analyses already take into account any slight broadening caused by to multipolar components.

Beyond the cosmology inference, this study also shows that, with high-S/N data, the multipoles have an imprint on the image of the extended source. Those observational constraints may be instrumental to better quantifying the contribution of multipoles to flux-ratio anomalies in lensed quasars (Mao & Schneider 1998; Kochanek & Dalal 2004; Gilman et al. 2019). This work might therefore help in extending existing studies of multipolar-like azimuthal perturbation as the source of flux ratio anomalies (e.g. Keeton et al. 2003; Xu et al. 2015) by calculating the effective contribution of the multipoles to the flux-ratio anomalies based on the perturbations seen in the ring. However, the accuracy with which multipoles can be recovered from the lens models has not yet been tested, and is left for future work.

4.A Source reconstruction with shapelets

In Section 4.3.7, we model mock images with additional freedom in the source shape model. We present in Figure 4.10 the source reconstruction obtained when modelling mock systems created with $a_4 = 0.05$ (last row of Table 4.1) with a source more complex than a smooth circular Sersic. For this purpose, we added shapelets to the source light distribution. We present the results obtained with two different maximal polynomial orders $n_{\max}$ of the shapelets. We see that more complex clumpy structures appear in the source with the increase of $n_{\max}$. Those complex structures create lensed

images that mimic those produced by multipoles, sometimes even achieving a reasonably good fit. The change in the source morphology may however hardly mimic structures seen in real galaxies. Models that predict such a source morphology would probably be considered as a symptom of a shortcoming in the macro-model of the lensing galaxy. We suggest that in the future, a machine-learning-based strategy could help to identify such features as artefacts caused by an incorrect macro model in an objective manner.

4.B Other mass profiles

In Sections 4.3.3 & 4.3.4, mass models deviating from the base setup are used. A power-law model is used in the fitting procedure in Sections 4.3.3 & 4.3.4. In addition, a composite model made of a baryonic component represented by a Chameleon profile and a dark matter component emulated with a NFW profile are used to create the mock lensing galaxy in Section 4.3.4. Hereafter, we specify the equations associated to those mass profiles.

4.B.1 Power-law model

The convergence of an elliptical power-law profile is given in Equation (1.18) and is reminded here:

$$\kappa(\theta_1,\theta_2) = \frac{3-\gamma'}{2}\left(\frac{\theta_E}{\sqrt{q\theta_1^2+\theta_2^2/q}}\right)^{\gamma'-1},$$

where (θ_1,θ_2) are the coordinates in a reference frame oriented along the main axis of the power-law ellipsoid, γ' is the slope of the profile ($\gamma'=2$ corresponds to the isothermal case), θ_E is the Einstein radius, and q is the axis ratio.

4.B.2 Chameleon model

The Chameleon mass model (Dutton et al. 2011; Suyu et al. 2014; Gomer et al. 2022) is a profile with finite mass equal to the difference between two non-singular isothermal ellipsoids (NIEs) with the same normalisation but different core radii. It also mimics a Sersic profile for Sersic indexes roughly between 1 and 4. This profile is mostly used to represent baryonic matter in mass as well as in light. One formulation of convergence of the Chameleon profile is the following:

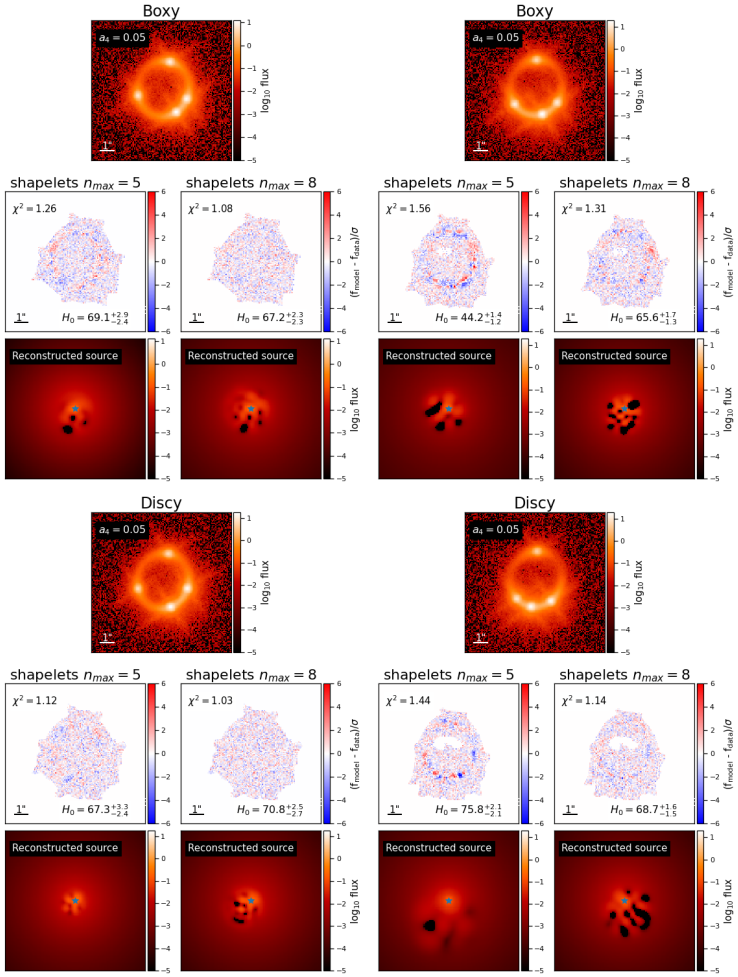

Figure 4.10: Shapelet reconstruction of the source for four mock systems with $a_4 = 0.05$, 3000s exposure time and a bright source.

Notes. The displayed configurations are either *fold* configuration (left) or *cusp_s* configuration (right). The input lensing galaxy is either boxy (top) or discy (bottom). For each mock system, we consider two fitting setups: including shapelets in the source model with maximal polynomial order $n_{\max} = 5$ or $n_{\max} = 8$. The associated residuals and source shape reconstruction are displayed. For good models (i.e. $\chi^2 < 1.2$), the morphology of the source gets less realistic as $n_{\max}$ increases.

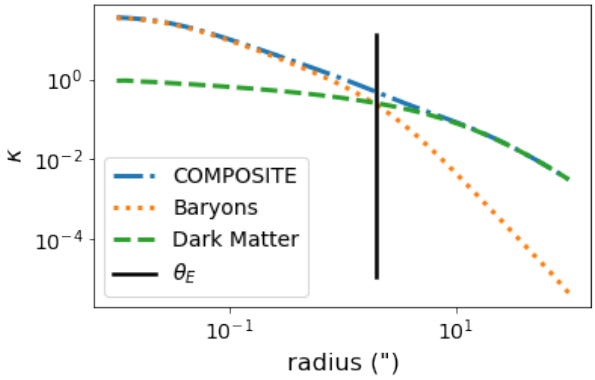

Figure 4.11: Radial convergence profile of the composite model used in Section 4.3.4.

Notes. The baryonic component emulated by a Chameleon profile (dotted orange), the dark matter component rendered with a NFW profile (dashed green), and the sum of both components (dash-dotted blue) are represented. The vertical solid black line indicates the Einstein radius of the total composite mass profile.

$$\kappa(\theta_1,\theta_2) = \frac{L_0}{1+q}\left(\frac{1}{\sqrt{\theta_1^2+\theta_2^2/q^2+4w_c^2/(1+q)^2}} - \frac{1}{\sqrt{\theta_1^2+\theta_2^2/q^2+4w_t^2/(1+q)^2}}\right), \tag{4.10}$$

where (θ_1,θ_2) are the coordinates in a reference frame oriented along the main axis of the Chameleon ellipsoid, L_0 is a normalisation factor, q is the axis ratio, w_c is a proxy for the core radius of the first NIE, and w_t is a proxy for that of the second NIE.

In Section 4.3.4, we use the following values: $q = 0.8$, $w_c = 0.024$, $w_t = 2.8$, and L_0 such that the deflection angle at $1''$ (if the Chameleon were circular) is $1.6''$. Such a Chameleon profile mimics a Sersic profile of index $n = 4$ and effective radius $R_{\rm eff} = 2.3''$. The radial profile of this Chameleon is presented with the dotted orange curve in Figure 4.11.

4.B.3 NFW model

The Navarro-Frenk-White (Navarro et al. 1996) mass profile is the most commonly used profile to represent dark matter halos. The three-dimensional density of such a circular profile is given by:

$$\rho(r) = \frac{\rho_0}{(r/r_s)(1+r/r_s)^2}, \tag{4.11}$$

where r is the radius, ρ_0 the central density, and r_s the scale radius. We refer to Golse & Kneib (2002) for a more complicated formulation of such a profile with ellipticity introduced in the lensing potential, as used in our simulations with `lenstronomy`.

In Section 4.3.4, we use the following values: $\rho_0 = 2.3\times10^{15}\ \mathrm{M}_\odot/\mathrm{Mpc}^3$, $R_s = 0.071$ Mpc, and the ellipticity is chosen such that the axis ratio in equal to 0.8 in convergence. Physically, this profile has a virial radius $R_{200} = 0.42$ Mpc and a virial mass $M_{200} = 1.1\times10^{13}\ \mathrm{M}_\odot$. The radial profile of this elliptical NFW is drawn in dashed green at Figure 4.11.

4.6 Further discussion at the light of recent literature

As stressed in this chapter, data quality is a crucial factor to consider to assess the detectability of the multipoles. Unfortunately, there is no universal way to summarize data quality. The signal-to-noise ratio (S/N) is instrumental in judging the quality but can be defined in multiple ways. One can characterise it by the instrumental set-up, with the exposure time and the magnitude of the observed object, or one can conversely cite the peak S/N or a statistic of S/N on a group of pixels. The former is mainly used in this chapter to distinguish between the different cases. Nevertheless, such description alone is insufficient when comparing my work to Galan et al. (2022)'s, in which the effect of multipoles on the extended source leaves very low residual patterns compared to mine, for similar instrumental set-ups and comparable extended source unlensed-and-lensed magnitudes. The difference lies in the radial profile of the source. By switching from my source shape ($R_{\mathrm{sersic}} = 0.1''$, $n_{\mathrm{sersic}} = 3$) to Galan et al. (2022)'s ($R_{\mathrm{sersic}} = 0.8''$, $n_{\mathrm{sersic}} = 2$), the peak S/N of an image of the extended source is divided by a factor 4. To produce the same decrease of peak S/N, I can equivalently divide the input flux of my "compact" extended source by a factor 14. Even though, citing the peak S/N does not describe the width and quality of the arcs, which will matter in the fitting procedure. While no simple characterisation of the data quality is perfect, comprehensive descriptions of the simulations help reproducing and comparing works more efficiently.

CHAPTER 5

MASS DENSITY TWISTS AND ELLIPTICITY GRADIENTS

This Chapter is based on Van de Vyvere et al., *Consequences of the lack of azimuthal freedom in the modeling of lensing galaxies*, Accepted in A&A (2022). Section 5.1 has been summarized as the context has already been introduced in Chapter 1. Minor changes have been applied to refer to Equations and Sections of this thesis when needed.

Massive elliptical galaxies can display structures that deviate from a pure elliptical shape, such as a twist of the principal axis or variations in the axis ratio with galacto-centric distance. Although satisfactory lens modelling is generally achieved without accounting for these azimuthal structures, the question about their impact on inferred lens parameters remains, in particular, on time delays as they are used in time-delay cosmography. This Chapter aims at characterising these effects and quantifying their impact considering realistic amplitudes of the variations. We achieved this goal by creating mock lensing galaxies with morphologies based on two data sets: observational data of local elliptical galaxies, and hydro-dynamical simulations of elliptical galaxies at a typical lens redshift. We then simulated images of the lensing systems with space-based data quality and modelled them in a standard way to assess the impact of a lack of azimuthal freedom in the lens model. We find that twists in lensing galaxies are easily absorbed in homoeidal lens models by a change of orientation of the lens up to 10° w.r.t. the reference orientation at the Einstein radius, and of the shear by up to 20° w.r.t. the input shear orientation. The ellipticity gradients,

on the other hand, can introduce a substantial amount of shear that may impact the radial mass model and consequently bias H_0, up to 10 $\mathrm{km\,s^{-1}\,Mpc^{-1}}$. However, we find that light is a good tracer of azimuthal structures, meaning that direct imaging should be capable of diagnosing their presence. This in turn implies that such a large bias is unlikely to go unaccounted for. Furthermore, the overall impact of twists and ellipticity gradients averages out at a population level. For the galaxy populations we considered, the cosmological inference remains unbiased.

5.1 Introduction

Morphological features of galaxies could provide important information about their formation history (Hao et al. 2006; Kormendy et al. 2009; Chaware et al. 2014; Cappellari 2016). Early surface photometry measurements of large samples of galaxies have shown different estimates of the percentage of significantly twisted objects among the galaxies. The estimates range from 10% to 60% (Lauer 1985b,a; Michard 1985; Djorgovski & King 1986; Jedrzejewski 1987; Vigroux et al. 1988). This broad disagreement can partially be described by the different criteria that are used to select the samples, the data quality of the images, and by the definition of the twist itself. Moreover, several factors unrelated to the intrinsic structure of the objects may be able to produce isophotal twisting, such as dust in lanes or patches, the overlap with isophotes of nearby projected companions, tidal effects due to nearby galaxies, a non-circular point spread function, and artificial trends in the background even after flat fielding (Kormendy 1982; Fasano & Bonoli 1989). Nevertheless, intrinsic azimuthal variations with the major axis of elliptical galaxies is now acknowledged. For instance, Hao et al. (2006) analysed the shape of 847 early-type galaxies and reported a standard deviation of 8.39° for the position angle variation between 1 and 1.5 half-light radii in their sample, and a 0.051 scatter for the ellipticity variations. Kormendy et al. (2009) focused on all known elliptical galaxies in the Virgo cluster and reported the position angle, ellipticity, and brightness profiles of those galaxies, linking the properties of the galaxies with a formation history. Corroborated by other studies (e.g., Krajnović et al. 2011; Fogarty et al. 2015; Cappellari 2016) and with the ingress of kinematics data, the formation history of elliptical galaxies, distributed into slow rotators and fast rotators, is becoming better understood. Slow rotator galaxies, with masses typically below $2\times10^{11}\mathrm{M}_\odot$, arise from spiral galaxies, are distributed in space accordingly, and are consistent with oblate spheroid shapes. On the other hand, more massive fast rotators are present in locally denser environments and are likely to display a triaxial symmetry. With the advent of understanding the galaxy formation and the structure of early-type galaxies, further models of elliptical galaxies are expected to be able to reach an increased precision.

While gravitational lensing analysis requires many ingredients to perform with the best precision, we focus here on the role of the mass model of the lensing galaxy. Most

lensing galaxies are massive ellipticals. Those early-type galaxies are mainly modelled by either a power-law ellipsoid or by a combination of a dark and baryonic ellipsoidal components in strong-lensing studies. From the point of view of the lensing mass distribution, the assumption about the radial mass profile has been explored extensively (Schneider & Sluse 2013, 2014; Xu et al. 2016; Kochanek 2020; Birrer et al. 2020; Kochanek 2021), while the azimuthal mass profile has been explored less frequently. Recently, Van de Vyvere et al. (2022a) (i.e. Chapter 4) specifically addressed the question of the impact of boxyness or discyness on the consmographic inference if only quadrupolar-mass models are used. Cao et al. (2022) studied the influence of the shape of lensing galaxies under the Elliptical Power-Law (EPL) model assumption in more detail. They used simulations of mock images whose lensing galaxy mass morphology was based on observed SDSS-MaNGA[1] stellar dynamics data, and cautioned about too simple (i.e., EPL) lens-mass models. Kochanek (2021) also cautioned about the possible effect of angular variations in the lensing galaxy on the Hubble constant when the model used lacks degrees of freedom in the azimuthal direction. These setups can allow clear but incorrect likelihood distinctions between different radial mass profiles that sometimes lead to an apparently precise but biased H_0 determination.

Only few works have intentionally taken possible twists and ellipticity variations with radius in the modelling of strong lensing galaxies into account. Schramm (1994) developed a framework to create any type of lensing galaxy profile through an ensemble of elliptical slices, but his work was not used in practical applications. Keeton et al. (2000) used a double pseudo-Jaffe model, with different core radii, cutoff radii, position angles, and ellipticities, to account for twist and ellipticity variations in the lens mass profile of the lensing system Q0957+561. Fadely et al. (2010) refined the model of the same lensing galaxies. They explicitly used the light map of the galaxy with a modelled constant mass-to-light ratio to account for the baryonic component, using fast Fourier transform methods to convert the mass maps into the lensing quantities. For the dark matter component, either a Navaro-Frenk-White profile (NFW; Navarro et al. 1996) or a combination of three softened power-law profiles were used. The twists and ellipticity changes of the light profile were thus explicitly used in the mass model for this specific system Q0957+561. More generally, using multiple analytical components in a mass model can inherently account for a gradient in ellipticity or position angle. In addition, nonparametric mass models (e.g., Liesenborgs et al. 2009; Lefor et al. 2013; Lubini et al. 2014) naturally allow for more azimuthal freedom. However, these free-form or multicomponent models have not been used to quantify the impact of azimuthal variations, but rather naturally account for it, sometimes even affording a larger freedom than is present in galaxies.

In this Chapter we do not model known lens systems with mass profiles increased

[1] SDSS stands for Sloan Digital Sky Survey, and MaNGA for Mapping Nearby Galaxies at APO, with APO standing for the Apache Point Obseratory

in azimuthal structures, but instead systematically investigate the impact that azimuthal perturbations have on lensed image morphologies by means of simulations. Specifically, we create mock lensing galaxies with varying position angle and/or ellipticity, simulate lensing images of a background source and model the images with standard lensing modelling methods, that is, we do not take the varying azimuthal structure into account. This experiment allows us to quantify the impact of the lack of azimuthal degree of freedom in a model of a lensing galaxy that displays twists and/or ellipticity gradients. This Chapter is complementary to Chapter 4 which investigates the impact of another type of azimuthal variations in lensing galaxies, that is, boxyness and discyness.

In Section 5.2 we first review the method of Schramm (1994) to simulate a lens mass profile displaying a varying position angle and ellipticity (Section 5.2.1). We then apply it (Section 5.2.2), explaining the strategy we followed, introducing a first academical experiment, and then a more realistic one. We end our method section with the characteristics of our mock images (Section 5.2.3) and standard fitting procedure (Section 5.2.4). In Section 5.3 we display the results of the different experiments. Finally, we summarize our findings and conclude in Section 5.4.

The fiducial cosmology used in this Chapter is identical to the one used in Chapter 4. We assume a flat ΛCDM cosmological model and the associated cosmological parameters are $\Omega_m = 0.3$, $\Omega_\Lambda = 0.7$, and $H_0 = 70\,\mathrm{km\,s^{-1}\,Mpc^{-1}}$.

5.2 Method

To study the effect of twists and ellipticity changes with radius on lensed images, we designed the following experiment. First, different lens mass profiles displaying twists and/or ellipticity variations were created. These mass profiles were then used to simulate mock images with HST data-quality by lensing a background source, consisting of a quasar and its host galaxy. The time delays associated with the lensed quasar images were also calculated. Afterward, the simulated frames were modelled using a power-law elliptical mass distribution (PEMD) and shear for the mass model, thus displaying neither twist nor ellipticity changes in the model. After the modelling process, we assessed the goodness of the fit and analysed the retrieved parameters to correlate the varying input profiles with specific modelled parameters, such as H_0. This method is similar to the one presented in Van de Vyvere et al. (2022a) (i.e. Chapter 4) which studied the impact of boxyness and discyness in lensing galaxies. As this Chapter and Chapter 4 focus on different types of azimuthal variations, the lensing galaxies are built differently: here we use a sum of slices that radially mimic a singular isothermal ellipsoid (SIE) profile, while we used an analytical SIE perturbed by a global octupolar moment in Chapter 4. Nevertheless, the scientific procedure is the same in the two Chapters as they both quantify how the input azimuthal perturba-

tions in lensing galaxies impact the parameter inference with a mass model displaying a single elliptical shape.

5.2.1 Lens mass profile: theory

We used the technique developed by Schramm (1994) to construct a mass distribution that allows the position angle to twist and ellipticity to vary with radius. This technique consists in approximating any mass profile by a sum of finite elliptical slices of constant surface mass density that can have different ellipticities, position angles, centers, and major-axis lengths. The superposition of the slices is a discrete approximation of the global mass profile. For each slice, the following quantities can be calculated: the lensing potential, its first derivative, that is, the deflection angles, and its second derivatives. They are then summed to compute the lensing quantities associated with the global mass profile. The lensing quantities associated with one slice are separated into two parts: those for a position inside the slice, and those for a position outside of the slice. If we consider an elliptical slice of constant surface mass density Σ_0 with a semi-major axis a, semi-minor axis b, and a position angle φ, the lensing potential at position (x, y) inside a slice centered at coordinates $(0,0)$ is given by

$$\Psi_{\rm in} = \frac{1}{2}\left((1-\epsilon)(x\cos\varphi + y\sin\varphi)^2 + (1+\epsilon)(y\cos\varphi - x\sin\varphi)^2\right)\Sigma_0 + \Sigma_0 r_{\rm E}^2(1-\epsilon^2)\ln r_{\rm E}\,, \tag{5.1}$$

where the elliptical parameter ϵ is $\frac{a-b}{a+b}$, and the elliptical radius $r_{\rm E}$ is equal to $\frac{a+b}{2}$. Outside the slice, the lensing potential is given by:

$$\Psi_{\rm ext} = \Re\left[\frac{1-\epsilon^2}{4\epsilon}\left(f^2\ln\left(\frac{{\rm sign}(ze^{-i\varphi})ze^{-i\varphi} + \sqrt{z^2e^{-2i\varphi} - f^2}}{2}\right) - {\rm sign}(ze^{-i\varphi})ze^{-i\varphi}\sqrt{z^2e^{-2i\varphi} - f^2} + z^2e^{-2i\varphi}\right)\Sigma_0\right], \tag{5.2}$$

where $z = x + iy$, $f^2 = a^2 - b^2$, and the sign function is defined such that

$${\rm sign}(z) = \begin{cases} +1 & \text{if x} > 0 \text{ or } (\text{x} = 0 \text{ and y} \geq 0) \\ -1 & \text{otherwise.} \end{cases}$$

The additive constant, that is, $\Sigma_0 r_{\rm E}^2(1-\epsilon^2)\ln r_{\rm E}$, in the $\Psi_{\rm in}$ definition was chosen such that the transition between external and internal potentials of a given slice was continuous. The deflection angle, $\alpha = \alpha_x + i\alpha_y$, inside the slice is given by

$$\alpha_{\rm in} = (z - \epsilon\bar{z}e^{2i\varphi})\Sigma_0. \tag{5.3}$$

And the deflection angle outside the slice is:

$$\alpha_{\rm ext} = \frac{2ab}{f^2}\left(\overline{z}e^{2i\varphi} - e^{i\varphi}\,\mathrm{sign}(\overline{z}e^{i\varphi})\sqrt{\overline{z}^2 e^{2i\varphi} - f^2}\right)\Sigma_0. \tag{5.4}$$

The second derivatives of the potential, which are also the first derivatives of the deflection angle, can be calculated numerically by deriving the deflection angle. We implemented such a mass profile under the name 'ElliSLICE' in the `lenstronomy` software.

To create a realistic lens mass profile, several slices have to be superposed. The lensing quantities (i.e., lensing potential and deflection angle) associated with each slice were calculated following Equations 5.1–5.4 , and they were then summed to constitute the lensing quantities associated with the whole profile. As the number of slices increases, the stepwise mass density approaches a smooth profile, but the computational time to calculate the lensing quantities of each slice and sum them grows as well. Approximately 60 slices in which the major axis is evenly spaced in log space are sufficient to accurately describe a realistic lensing mass profile, as shown in Figure 5.1 in which mass profiles created with slices are compared to a singular isothermal sphere (SIS). Section 5.3.1 and Figure 5.6 also later show that an HST-like mock image simulated with a lensing mass profile made of 60 slices following an SIE is perfectly modelled with an SIE mass model. Typically, the last slice extends up to five times the Einstein radius. Since each slice is associated with an analytical potential and deflection angle, these simulations show no spurious artificial shear, which occurs when truncated mass maps alone are used to compute the lensing quantities. The mass profile therefore does not have to be extended up to 50 times the Einstein radius (see Chapter 3, i.e. Van de Vyvere et al. (2020)).

In addition to the the mass of the lensing galaxy, a shear was also considered to mimic any tidal perturbation caused by galaxies along the line of sight or at the lens redshift. The lensing potential at position (x, y) associated with a shear is defined in Equation (1.20) and is reminded here:

$$\Psi_{\rm shear} = \frac{1}{2}(\gamma_1 x^2 + 2\gamma_2 xy - \gamma_1 y^2)$$

where γ_1 and γ_2 are the components of the complex shear. The shear strength is $\gamma_{\rm ext} = \sqrt{\gamma_1^2 + \gamma_2^2}$ and its orientation is $\phi_{\rm ext} = \frac{1}{2}\arctan(\gamma_2/\gamma_1)$. The first and second derivatives of the potential can easily be determined by analytical derivation of the lensing potential definition.

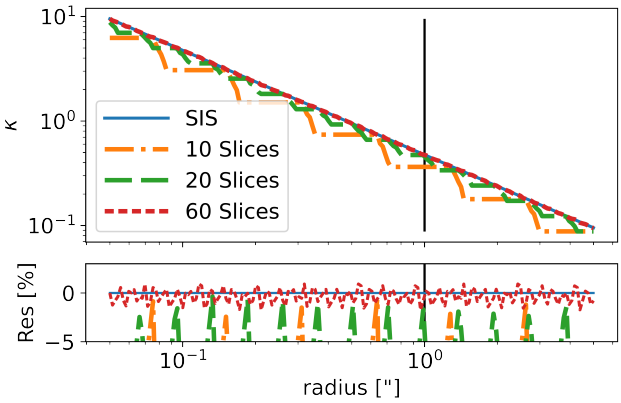

Figure 5.1: Accuracy of mass profiles created via slices following Schramm (1994) compared to an analytical Singular Isothermal Sphere (SIS).

Notes. Top : Radial convergence profile of a SIS (blue line), and of 'ElliSLICE' mass models using 10, 20, or 60 slices (dash-dotted orange line, dashed green line, and densely dashed red line respectively). Bottom : the residuals in percent between the SIS profile and profiles made of slices. The vertical black line indicates the Einstein radius.

5.2.2 Lens mass profile: in practice

5.2.2.1 Strategy

In practice, the lens mass profile consisting of elliptical slices needs to be defined by characterising each slice. The choice of the azimuthal profile given to the slices depends on the scientific question that is to be answered. Beyond the general investigation of the impact of twists and ellipticity gradients on lensing analyses, we particularly investigated which types of iso-density perturbations, that is, twists or ellipticity gradients, affect the fitted mass density profile most. We determined whether the same effects are produced if the variations are located in different regions of the galaxy. We further examined whether the combination of both position angle and ellipticity variations created unexpected degeneracies in the model. The quantitative impacts of the different perturbations when realistic twists and ellipticity gradients were considered were also studied.

We expect the twists to create quadrupolar moments that vary in orientation with radius; see the example in Figure 5.2 (top). The twists outside the Einstein radius are thus expected to be equivalent to additional external shears, while those inside the Einstein radius are expected to mostly influence the orientation of the fitted ellipsoid. Variations in ellipticity are expected to change the strength of quadrupolar

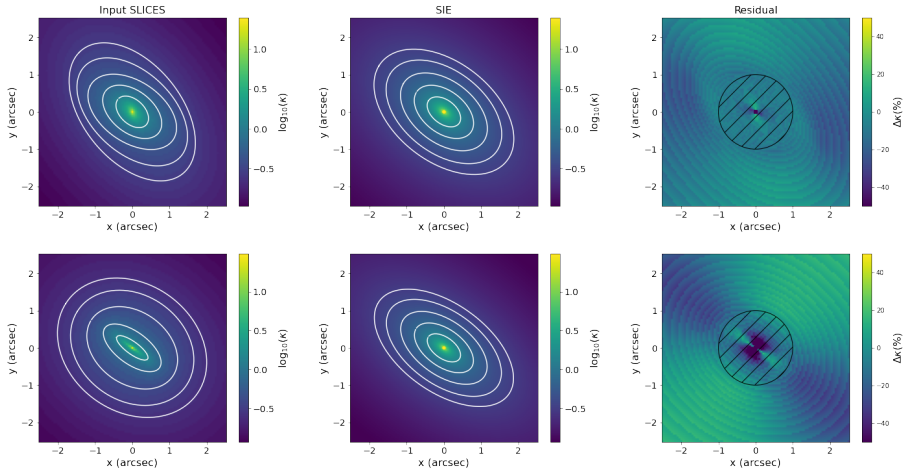

Figure 5.2: Comparison of mass profiles displaying twists or ellipticity variations with a mass profile following pure ellipsoid.

Notes. Left: Example of input profiles created with the slices method as explained in Section 5.2.1, displaying either twists (top) or ellipticity changes (bottom). Middle: singular isothermal ellipsoid with the ellipticity and the position angle of the corresponding sliced profile at the Einstein radius, i.e. $1''$. Right: Difference of the two kappa maps in percentage of the input profile, the dashed region indicates the region inner to the Einstein radius.

moment with radius, but not its orientation, as illustrated in Figure 5.2 (bottom). The ellipticity gradient is consequently absorbed by an interplay of shear and ellipsoid azimuthal shape, and may influence the slope of the radial profile of the ellipsoid to better balance the internal versus external shear, as suggested by Kochanek (2021).

To answer the different questions we raised, we explored two main paths: 1) We created an experiment in which we controlled the position angle profiles and the ellipticity gradients in order to systematically determine the influence of either twists or ellipticity changes in different parts of the galaxy, that is, inside the Einstein radius, at the Einstein radius, and outside the Einstein radius. 2) We created samples with twists and ellipticity changes based on realistic galaxies to investigate the impact of azimuthal structures on the population level. We note that by convention, when we report quantities measured at the Einstein radius, we effectively provide its value as measured at the slice whose major axis is closest to the Einstein radius.

Our first experiment consisted in using linear functions to describe the position angles or ellipticity profile, allowing changes in azimuthal structures at specific locations in the mock galaxy. This first sample was not meant to reproduce real galaxies, but limited the azimuthal structure to specific and controlled aspects. This allowed

us to qualitatively assess the effect of these structures on the modelling behavior.

The second experiment we conducted mimicked real galaxies. We used two physically motivated samples: We first used observation-based morphological properties of nearby elliptical galaxies, which has the drawback of only tracing the light. We then used morphological properties of hydro-dynamically simulated galaxies, which allowed us to trace the full mass profile, but might not always match the mass profiles of real galaxies. With each sample, we used elliptical slices to create mock lensing-mass profiles for which we selected either twists or ellipticity gradients to analyse each effect separately. We then combined the two variations to mimic populations that encompass the diversity of a sample of real lensing galaxies.

5.2.2.2 Monotonic azimuthal variations

First, we constructed a lens with slices displaying position angles and/or ellipticities that varied with radius according to an analytical function. The purpose of this first way of producing perturbations was to exactly control the input twist or ellipticities and acquire a basic knowledge about the influence of specific twist and ellipticity changes in lensing images.

In this test, we assumed a linear change in position angles or ellipticity with semi-major axis. We considered both variations separately. We chose a profile made of 60 slices, evenly spaced in log space, ranging from $0.01''$ to $6''$. When we varied the ellipticity, the latter grew linearly from 0.65 to 0.85, that is, at a rate of 0.033 per arcsec. When instead twists were considered, the angles varied linearly from 0° to 60 °, that is, 10° per arcsec rate of change (see Figure 5.3 and Figure 5.11). This variation is not meant to be realistic, but is still comparable to what is observed in hydrosimulated galaxies or in local galaxies, as shown in Figure 5.11. The Einstein radius was set to $\theta_E = 2''$, such that the variations in ellipticity or positions angles were significant both inside and outside the Einstein radius (see Figure 5.3).

We considered three regions in which variations could occur: the inner region, that is, the region in which the semi-major axis of the slices is $< 0.9\ \theta_E$; the middle region, characterised by a semi-major axis $> 0.9\ \theta_E$ and semi-minor axis $< 1.1\ \theta_E$; and the outer region, in which the semi-minor axis $> 1.1\ \theta_E$. With these regions, we created five different types of mock lensing profiles: (1) Mocks in which all slices were aligned and displayed the same ellipticity, that is, a constant axis-ratio and position angle in all regions. (2) Mocks for which only the inner part of the input galaxy was allowed to vary, either with twists or ellipticity changes. In other words, we varied the inner region, but the middle and outer regions remained constant. (3) Mocks with changes only near the Einstein radius, that is, changes in the middle region and a constant profile in the inner and outer regions. (4) Mocks in which only the outskirts of the galaxy varied, that is, variations in the outer region, but not in the inner and middle regions. (5) Finally, mocks in which variations occurred in all the three regions.

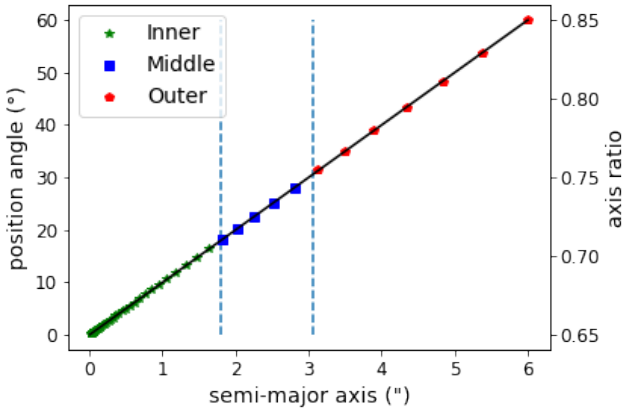

Figure 5.3: Slices properties of a fully varying profile in the monotonic azimuthal variations experiment, with either twists (left y-axis) or ellipticity gradient (right y-axis).

Notes. The dashed vertical lines are, from left to right, the line at which the semi-major axis = 0.9 θ_E and the line at which the semi-minor axis = 1.1 θ_E, considering an Einstein radius of 2″. They separate the different regions considered for variations (see Section 5.2.2.2). The slices belonging to the different regions are represented with different colors and symbols.

When either the position angle or the ellipticity was not allowed to vary, the fixed value was chosen to be the one at the Einstein radius. Figure 5.3 shows the fully varying position angle or axis ratio profile of the slices as a function of semi-major axis. The three regions we considered to delimit the different cases described above are indicated.

5.2.2.3 Data-motivated azimuthal variations

Second, we used realistic changes of ellipticity and/or position angles to quantitatively measure the impact of these variations on the lens modelling parameters. We investigated two types of realistic lensing galaxy samples. (a) We used observed light profiles of local massive elliptical galaxies through the sample studied by Kormendy et al. (2009). As the dark matter of these galaxies cannot be measured directly, the isophotes are the best reasonable proxy to the shape of the mass profile of elliptical galaxies. (b) We used hydro-dynamical simulations of the universe and directly accessed the mass of massive ellipticals at redshifts typical of lensing galaxies with the EAGLE[2] simulations (Schaye et al. 2015; Crain et al. 2015; McAlpine et al. 2016). The

[2] EAGLE stands for Evolution and Assembly of GaLaxies and their Environments

two samples have differences and similarities, which highlights the necessity of exploring both. We first present the two samples and then compare them.

For each galaxy in the sample, we created three types of profiles: (1) allowing variation of ellipticity, but fixing the position angles, (2) allowing twists, but fixing the ellipticity, and (3) allowing both types of variations. Fixing either the positions angles or the ellipticity helps understanding the role of each type of variations for the lensing quantities through the modelling scheme, while the cases where both types of changes are displayed are most representative of massive elliptical galaxies. For comparison purposes, a fiducial profile with both fixed position angle and ellipticity was also created for each galaxy. Since azimuthal structure variations may not be self-similar with galacto-centric radii, we created mocks for systems with Einstein radii of either 1 or 2 $''$.

(a) Observation-based morphologies

Kormendy et al. (2009) analysed the light profile of all known early-type galaxies in the Virgo cluster and provided the isophotal analysis of each galaxy (i.e., size, ellipticity, and orientation of ellipses matching the isophotes constituting the light profile). Among others, they included lenticular galaxies, dwarf ellipticals, and spheroidal galaxies (Kormendy et al. 2009; Graham 2019b). We did not select any of these peculiar types of early-type galaxies. We selected nine massive elliptical galaxies that extend at least up to $4''$ when redshifted to the target lens redshift (see Section 5.2.3 for a discussion of the redshift). While this limit of $4''$ may seem arbitrary, it ensures that the galaxies are wide enough to provide isophotal data up to at least twice the Einstein radius. Our sample is thus composed of the following elliptical galaxies: NGC 4649, NGC 4374, NGC 4261, NGC 4382, NGC 4636, NGC 4459, NGC 4473, NGC 4472, and NGC 4486.

The advantage of this sample is that it represents light measurements of real galaxies. Even without knowing the dark matter distributions, we can at least be sure that this sample is representative of the light distributions of typical local massive elliptical galaxies.

(b) Hydro-simulation based morphologies

The EAGLE project (Schaye et al. 2015; Crain et al. 2015; McAlpine et al. 2016) is a suite of hydro-dynamic simulations that was run with a modified version of the smoothed particle hydro-dynamics code `GADGET3` (last described by Springel 2005) with 1504^3 dark matter particles and an equal number of baryonic particles. The gravitational softening length of these particles is 2.66 comoving kpc (ckpc), limited

to a maximum physical scale of 0.7 proper kpc (pkpc). The resulting galaxies are in overall agreement with observed properties such as the star formation rate, passive fraction, Tully-Fischer relation, total stellar luminosity of galaxy cluster and colors (Schaye et al. 2015; Trayford et al. 2015), the evolution of the galaxy stellar mass function and sizes (Furlong et al. 2015, 2017), rotation curves (Schaller et al. 2015), and the α-enhancement of early-type galaxies (Segers et al. 2016).

To select a sample similarly populated as the Kormendy et al. (2009) sample, we used several criteria. First, we selected galaxies at redshift $z = 0.271$ (see Section 5.2.3 for a discussion of redshift), and then used a threshold at $10^{11}\mathrm{M}_{\odot}$ to select only the most massive galaxies. To avoid most spiral or lenticular galaxies displaying discy shapes, we considered the galaxies properties and selected only those with a principal axial ratio $c/b > 0.7$ following Trayford et al. (2019). We then applied the Simulating EAGLE LEnses (SEAGLE; Mukherjee et al. 2018) lens-simulation pipeline (Mukherjee et al. 2018, 2021), which uses the `GLAMER` code (Metcalf & Petkova 2014; Petkova et al. 2014) for particles projection, to the selected galaxies to create their dark matter, stellar, and gas surface mass density maps using different projection axes. The sum of the three components is the total projected mass map of a galaxy. Our selection still comprised about 25 galaxies, with projected mass maps in three arbitrary orthogonal directions. We thus randomly chose a subsample of 12 mass maps out of these. Three of these have peculiar ellipticities in the center of the galaxy, that is, axis ratios lower than 0.3 at radii typically smaller than $0.8''$. This intermediate-scale disk component is typical of ES, also called ellicular, galaxies (Liller 1966; Graham 2019a,b). The three ES galaxies appear as ES only in one projection. In the other projections, they appear as regular elliptical galaxies.

To convert the EAGLE mass maps into a series of elliptical slices, we used the `AutoProf` (Stone et al. 2021) software. `AutoProf` is a recent software providing pipelines that allow reducing, treating, and analysing several images at the same time. We only used the part of the pipeline that fits ellipses at different radii of a galaxy and display, among others, the ellipticity, the position angle, and the size of each retrieved ellipse. This isophotal fitting algorithm is based on Jedrzejewski (1987) with improvements in speed and accuracy through procedures adapted from machine-learning techniques. We cross-validated the resulting profiles with the more broadly used function `Ellipse` in `photutils` (Bradley et al. 2020). This last method is similarly based on Jedrzejewski (1987), but does not include the regularization schemes borrowed from machine learning used in `AutoProf`. As expected following Stone et al. (2021) for regular elliptical galaxies, the results from the two methods are similar, and the `AutoProf` results are more stable.

(c) Comparison of properties of the two realistic samples

The two galaxy samples from observations and from hydro-simulations have slightly

different properties in terms of changes in position angles and changes in ellipticity. To compare them, we introduced four metrics: ΔPA_{IN} ($\Delta elli_{IN}$), which is the change in position angle (ellipticity) between the slice with a semi-major axis at 0.25″ and the one at the Einstein radius ; and ΔPA_{OUT} ($\Delta elli_{OUT}$), being the change of position angle (ellipticity) between the slice with major axis at the Einstein radius and the one at twice this radius. These metrics summarize variations in ellipticity or position angles, even if the variation may not always be monotonic over the considered range of radii. The innermost limit is chosen to be 0.25″ to ensure that the shape parameters at this minimum semi-major axis are robust enough to be used as representative of the inner parts of the galaxies. Indeed, the EAGLE mass maps have a pixel size of 0.05″, and the fitted ellipses used to recover the shape parameters have to span enough pixels to adequately retrieve the local shape.

Two galaxies in our sample extracted from Kormendy et al. (2009) display particularly drastic position angle twists. However, one of these two galaxies is almost circular with an axis ratio of 0.97 at θ_E, compared to 0.84 for the other galaxy. Thus, only one galaxy in the chosen Kormendy et al. (2009) sample can be considered as significantly highly twisted. On the other hand, galaxies from the EAGLE sample generally display stronger changes in ellipticity. Since the sample from Kormendy et al. (2009) is based on isophotes of galaxies while the EAGLE sample is based on iso-density contours, the difference between the two sample could come from a difference between mass and light behavior. The EAGLE hydro-dynamical simulations provide stellar mass maps in addition to total mass maps. We can thus analyse the light of the EAGLE galaxies and compare it to properties of the light of observed galaxies in a consistent way. Comparison between the different samples in terms of twists and ellipicity changes are shown at Figure 5.4 as histograms and associated kernel density estimations (KDEs) of the four metrics for the samples we considered. The EAGLE iso-density and isophotal contours are similarly twisted and have analogous ellipticity changes. The range of ellipticity variations in the EAGLE sample, independently of whether we consider light or mass, is wider than the variation range from the sample from Kormendy et al. (2009). However, the highest $\Delta elli_{IN}$ and $\Delta elli_{OUT}$ are due to the three ellicular galaxies that were probed at two different Einstein radius. Excluding these three galaxies would lead to still wider, but more similar distributions of the EAGLE and Kormendy et al. (2009) samples. We conclude that the differences between the two samples is mainly due to the different types of early-type galaxies that constitute them. For illustration purpose, we present at Figure 5.11 a set of position angle and axis ratio profiles for the linear experiment from Section 5.2.2.2, two hydro-simulated galaxies, and two observed galaxies.

In addition to the position angle and ellipticity changes, we note that the axis ratios at the Einstein radius of the observed local galaxies are often higher than that of the simulated sample, as shown in Figure 5.5. This may yield a larger impact of the twists for the simulated sample, even with comparable distributions of the position

angle variations.

5.2.2.4 Radial mass distribution

For each mock lensing galaxy, we adjusted the surface mass density of each slice such that the radial profile at the mean elliptical radii follows an isothermal profile. We also always fixed the center of every slice to be the same in order to avoid any lopsidedness and focus on the effect of changes of position angle and/or ellipticity with the galactocentric radius.

To better understand the interplay between the azimuthal changes and the radial mass profile, we also constructed mock images based on radial lensing profile following a composite mass profile with baryonic and dark matter components. The results of this experiment are presented in Appendix 5.B.

Our method of specifying the constant surface density of each slice did not allow us to specify the Einstein radius and slopes with an arbitrary accuracy. This is particularly noticeable when there is a drastic change in ellipticity between several slices. In this case, the mass associated with the very-elliptical slices in the inner part of the galaxy can be underestimated and create a shallower profile at radii typically smaller than a few pixel, which biases the overall Einstein radius. If these extreme variations also occur up to the Einstein radius, the slope at that radius can be affected. Only the ellicular galaxies are subject to these drastic ellipticity evolution.Generally, the simulated Einstein radius and the slope of the azimuthally-averaged radial profile reach their targeted value (i.e., the value when no twist or ellipticity gradients are present) within an accuracy of 1%. For the most extreme cases, the Einstein radius can be biased by up to 7% and the slope by up to 3%. Different schemes of mass attribution to the slices can slightly modify the strength of this effect, but cannot prevent it. When analysing our results, we therefore ensured that we compared the fitted Einstein radius to the true input Einstein radius of each specific mock, calculated independently as being the radius at which the mean convergence drops below 1. This calculation has an accuracy of $0.01''$. The same practice was used for the slope results, which were compared to the input slope, measured using the azimuthally-averaged logarithmic power-law slope of a profile at the Einstein radius. In addition to the mass profile of the lensing galaxy made of slices, a shear was added with a strength $\gamma_{\rm ext} = 0.05$ and a random orientation $\phi_{\rm ext}$.

5.2.3 Creation of mock images

With the mass model produced as explained in the previous section, we used the `lenstronomy` software to create images of a background source composed of a quasar and a Sérsic host galaxy ($R_{\rm sersic} = 0.1, n_{\rm sersic} = 3$) at redshift $z_s = 2$, lensed by the mock lensing galaxy. The source was randomly placed inside the inner caustic to create a quad lens in the image plane. The choice of a circular Sérsic source allowed us to

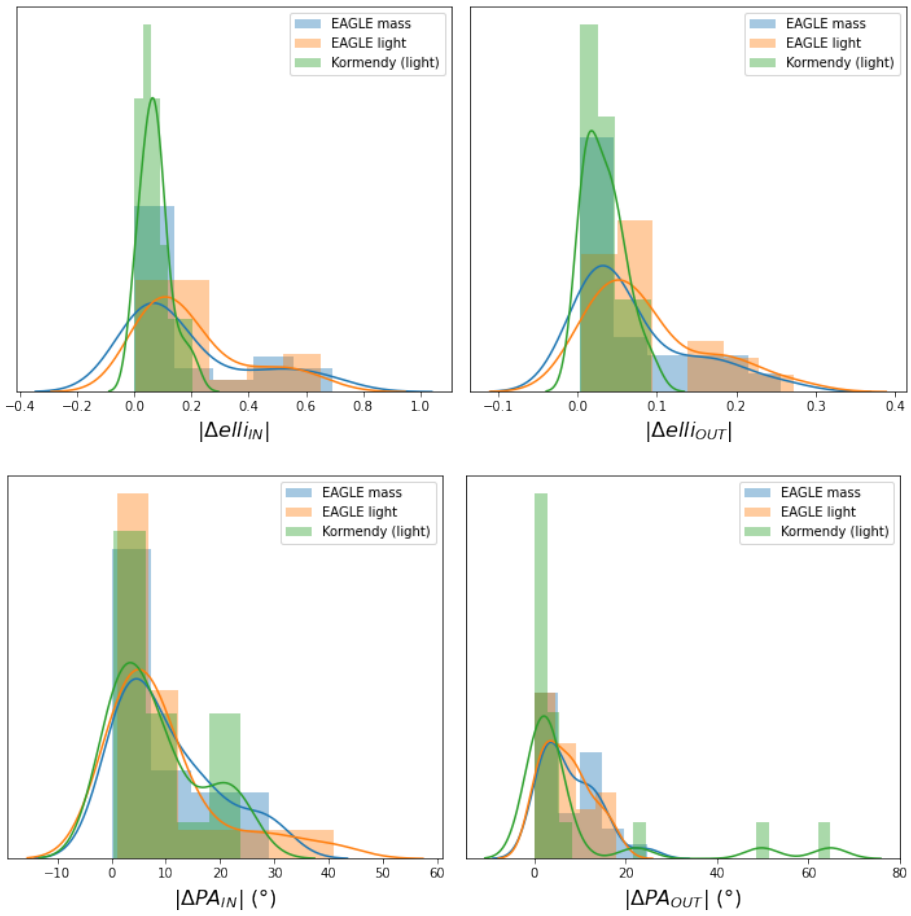

Figure 5.4: Distributions of absolute ellipticity changes (top) and position angles twists (bottom) for the observed and hydro-simulated sample.

Notes. The left panels summarize changes between 0.25″ and the Einstein radius, and the right panels focus on changes between one and two Einstein radii. The observed sample, using the light of nearby galaxies analysed by Kormendy et al. (2009) (green), is compared to the hydro-simulated sample using the mass of the EAGLE hydro-dynamical simulations from Mukherjee et al. (2018) (blue). The light profiles associated with the simulated galaxies (orange) is also displayed to facilitate comparison between the two samples.

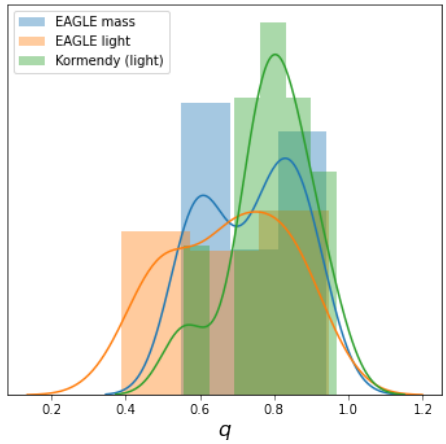

Figure 5.5: Distributions of the axis ratio at Einstein radius.

Notes. The colors are the same as in Figure 5.4.

avoid any specific degeneracy that could arise from the interplay between the ellipticity of the source, the image configuration, and the change in ellipticity or position angle in the lens.

We always considered our lensing galaxy at redshift 0.271. This redshift is typical of lensing galaxies as observed in the SLACS survey (Bolton et al. 2006; Treu 2010; González-Nuevo et al. 2012) and was also used in the SEAGLE project (Mukherjee et al. 2018), from which we used the pipeline to create mass maps in our sample of mock lensing galaxies based on hydro-dynamical simulations.

The lens was considered to be transparent to avoid blending between the lensed source images and the lens light. Incorporating lens light in our mock images would be more realistic. However, the lens light and the ring would overlap. Therefore the uncertainties introduced by the lens light subtraction would depend on the specific method used and would limit the generalization of the results. We nevertheless created a few mock images with lens light to assess the validity of our results for a non-transparent lens. We found that strong azimuthal variations in the lens light are generally not properly fitted by Sérsic profiles and ubiquitous patterns at the lens position can be seen in the residuals. On the other hand, if the lens light follows a nonazimuthally varying profile and is modelled as such, the additional freedom and noise introduced by the lens light beneath the arc do not influence the fitted parameters: consistent results are retrieved in both cases with and without lens light. We cannot rule out the possibility that specific lens-light profiles could degenerate with source-light patterns in the arc appearing due to azimuthal variations in the mass, and could

bias the subsequent fit. However, such cases are expected to be rare.

We created mocks with typical space-based data quality. In particular, we chose to simulate observations obtained with the Wide Field Camera 3 (WFC3) on board the Hubble Space Telescope (HST) in the F160W filter. This is one of the most frequently used setups for high-resolution imaging of lensed quasars (Suyu et al. 2017; Ding et al. 2021b). We used a PSF created from the drizzling of eight PSFs extracted from real images. This PSF is the same as the one used in Rung 2 and 3 of the Time Delay Lens modelling Challenge (TDLMC; Ding et al. 2021b). We used a pixel size of $0.08''$ and add noise assuming an exposure time of 5400 s. Our setup is highly similar to other works that simulated lensing systems (e.g., Ding et al. 2021b; Wagner-Carena et al. 2021; Park et al. 2021; Van de Vyvere et al. 2022a). A noise map and a mask, masking the pixels with values lower than twice the background level, were also created and were used during the lens modelling procedure.

The time delay between the quasar images were also calculated within `lenstronomy`. We used the exact value of the delay in the modelling process, but associated a 2% uncertainty with its value with a minimum threshold of one day.

5.2.4 Fitting procedure

After the mock images were created, they were modelled with `lenstronomy` assuming that the lensing galaxy is a singular power-law ellipsoid, and that an external shear is present. Since early-type galaxies density profiles are observed to be well approximated with a power-law profile up to large radii (Suyu et al. 2009, 2010), the power law was a standard model commonly employed to model real quasar images (Birrer et al. 2016; Shajib et al. 2019; Wong et al. 2020). We used a source model composed of a circular Sérsic profile with a quasar at its center. This setup uses similar light and mass profiles for the mocks and for the model, setting aside the azimuthal variations. It allowed us to test how the lack of flexibility of the model in the azimuthal direction impacted the inference. Because azimuthal and radial structures might interact, we later relaxed this assumption and used a radial distribution that no longer was a power law (Appendix 5.B).

As a first step, the slope of the power-law ellipsoid mass distribution (PEMD) was fixed to simulate an isothermal profile. A particle swarm optimization (PSO; Kennedy & Eberhart 1995; Shi & Eberhart 1998) was then initiated to identify the maximum likelihood. After convergence was reached (or, in a few cases, maximum iteration reached), the slope constraint was relaxed and a second PSO was started. A Markov chain Monte Carlo (MCMC), through the software `emcee` (Goodman & Weare 2010; Foreman-Mackey et al. 2013), finally proceeded in the vicinity of the second PSO optimum to sample the posterior and retrieve the uncertainties on the modelled parameters.

5.3 Results

5.3.1 Monotonic azimuthal variations

As described in Section 5.2.2.2, we performed an experiment with linear variations of ellipticity or position angles at radii lower, close to, and greater than the Einstein radius. While this test is not directly reflective of real galaxies, it is useful for understanding qualitatively the impact of each type of change occurring at different galacto-centric radii of a lensing galaxy. The results of this experiment are displayed at Figure 5.6.

Figure 5.6 shows that the changes in ellipticity outside the Einstein radius can be absorbed by the external shear by changing its strength by 0.01 and its orientation by 11°. The changes in ellipticity inside or at the Einstein radius, on the other hand, are absorbed by a change in slope that yields a bias of a few $\mathrm{km\,s^{-1}\,Mpc^{-1}}$ on H_0. The twists, on the other hand, mainly affect the retrieved orientations: the position angle of the ellipsoid is changed by up to 3 °for twists inside the Einstein radius, but the shear position angle varies by up to 37 °when the twist is outside θ_E, in agreement with Figure 5.2 (top). Twists present only at the Einstein radius do not influence orientations, as they are very localized and average out in the global mass profile. The effect of twists on the power-law slope and H_0 is harder to characterise as the evolution of both parameters when relaxing the fixed slope constraint is correlated, while the resulting H_0 remains mostly unbiased.

5.3.2 Data-motivated azimuthal variations

We now analyse the impact of twists and ellipticity gradients as they are displayed in data-motivated samples. The retrieved fitted parameters at a population level allow us to first verify the interpretation scheme outlined in Section 5.3.1, and second, to quantify the effective impact of data-motivated azimuthal structures. This last outcome will inform us on any possible issue affecting lens models that ignore the lens azimuthal structure. We refer to Section 5.2.2.3 for the description of the two samples used, that is (a) a sample based on observed isophotes of local galaxies and (b) a sample based on iso-density contours of galaxies drawn from hydro-dynamical simulations.

5.3.2.1 Observation-based morphologies

The summarized results of the selected Kormendy et al. (2009) population are displayed in Figure 5.7 and Table 5.2. As described in Section 5.3.1, the twists mainly impact the angles of the retrieved position angle of the main lens model, or the angle of the shear. The position angle of the ellipsoid differs from the fiducial angle with a scatter of 1.4°. The position angle of the shear is offset with respect to the true shear

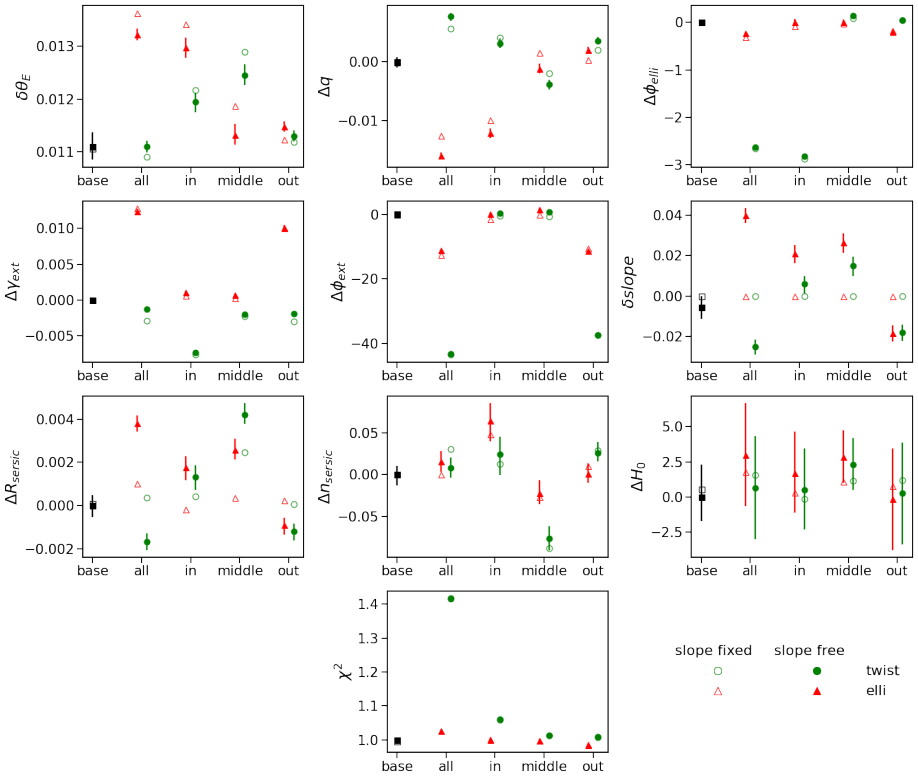

Figure 5.6: Fitted parameters of the performed experiment with linear variations of ellipticity and/or position angle with radius (see Section 5.3.1).

Notes. The two families of azimuthal variations, twist and ellipticity gradient, are displayed as green circles and red triangles, respectively. The results displayed with black squares are the ground-base case: the galaxy has iso-density contours that consist of ellipses displaying homoeidal symmetry (i.e., have the same axis ratio) and a single orientation. The open symbols characterise the results corresponding to the situation with a fixed fitted slope. The filled symbols display the median value of the final results after the constraint on the slope is relaxed. The error bars correspond to the 0.16 and 0.84 quantiles of the posterior distribution on the parameters. The x-axis tick labels indicate the type of variation considered: "base" refers to the ground-base case, "all" refers to variation occurring at all the radii, "in", "middle", and "out" indicate if the variation is limited to the region inside, around, or outside of the Einstein radius (see Section 5.2.2.2 for exact definitions). The y-axis quantities are defined in Table 5.1.

angle with a scatter of 2.8° on average. We note that the amplitude of the position angle deviation for the shear may also depend on the strength and orientation of the fiducial input shear. The gradient of ellipticity, on the other hand, mainly impacts the shear strength, the slope, the source size, and the value of H_0, introducing a scatter of 22%, 3.4%, 5.0%, and 5.1%, respectively, on these quantities. We did not separate the $\theta_E = 1''$ mock image results from the $\theta_E = 2''$ results because the two subsamples are too small to distinguish a statistically significant difference of behaviour.

Another clear trend is the correlation between H_0 and the fitted slope, but also with the source size. This suggests that to first order, the redistribution of the azimuthal mass due to ellipticity gradients has the same effect as the one produced by a mass-sheet transformation (MST; Schneider & Sluse 2013), as the fitted model is degenerate with the data provided that the source is magnified. The fact that the χ^2 is not 1 shows that this is not a perfect degeneracy. This behavior has been anticipated by Kochanek (2021), who stated that the presence of ellipticity variations will (1) favor a specific value of the fitted slope to balance internal and external shear introduced by the azimuthal perturbation and retrieve the correct general ring shape, (2) cause the model to increase or decrease the source size to recover the ring brightness and thickness, and (3) bias the value of H_0, which mainly depends on the lens mass model, accordingly.

The dependence of the modelled ellipticity on the input changes of the ellipticity inside the Einstein radius is trivial. The slight correlation between position angle of the PEMD model and the amplitude of the input twist is also trivial. The distribution of χ^2 informs us that good fits are retrieved in all cases, despite the twists and ellipticity changes. Finally, even if single H_0 values can be biased low or high, the recovered median value of the distribution is centered, within 0.3 σ, on the fiducial H_0, that is, 70 km s^{-1} Mpc^{-1}, for all types of azimuthal variations. We define σ as the mean value of the two sides of the 68% credible interval.

5.3.2.2 Hydro-simulation based morphologies

The results for the sample based on the EAGLE hydro-dynamical simulations is shown in Figure 5.8 and Table 5.3. The observed trends are similar to those from the sample of Kormendy et al. (2009), despite a few peculiarities that we explain below. First, the scatter on the position angle of the ellipsoid and on the shear in presence of twists is wider than what we measured in Section 5.3.2.1, with population standard deviations of 2.4° and 8.4°, respectively. The scatter on the recovered shear strength is about 44% in presence of ellipticity gradients, 26% with twists, and reaches 50% when the two morphological deformations are present, which is twice broader for this sample than for the sample of Kormendy. Second, when gradient of ellipticities are present, the retrieved axis ratio can differ by up to several percent from the ratio measured at the Einstein radius, in particular when a strong ellipticity gradient is present inside the Einstein ring. However, strong gradients are also harder to fit with a single elliptical

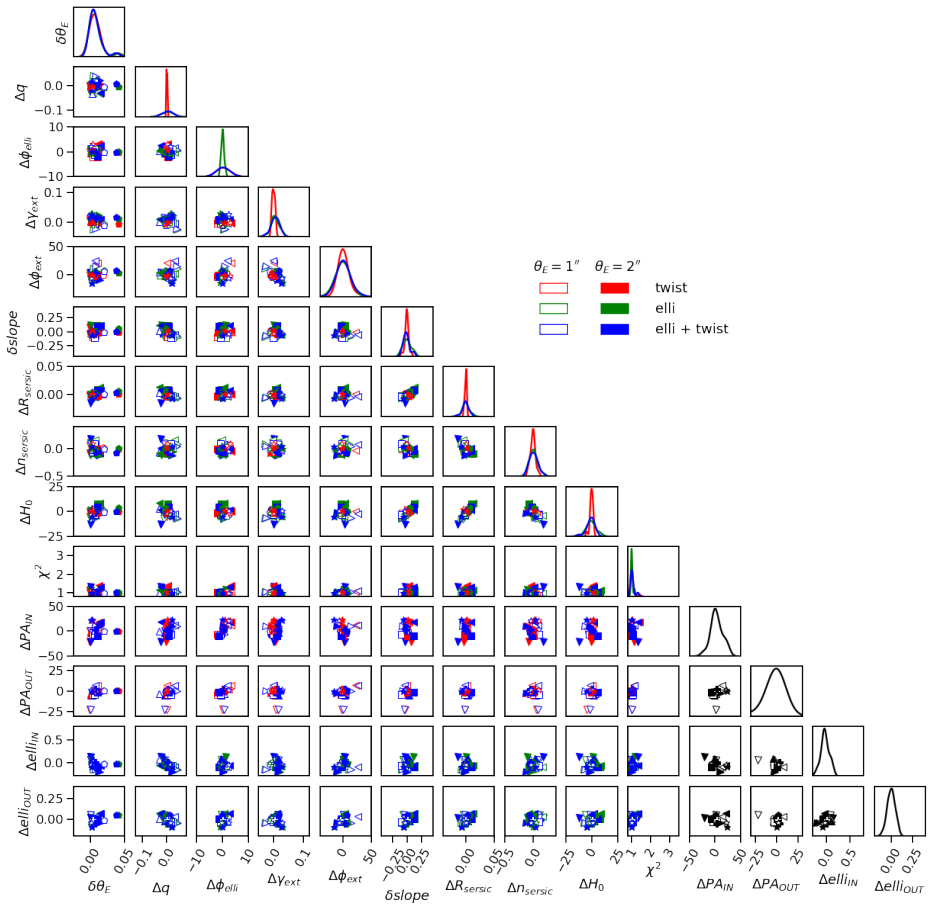

Figure 5.7: Population results based on mock mass profiles following the ellipticity and position angle variations observed in local galaxies, using the Kormendy et al. (2009) sample.

Notes. The nine fiducial galaxies are represented with different symbols, filled when the considered Einstein radius is $2''$, and empty for $\theta_E = 1''$. Each galaxy is used to create three types of mock mass profile: the twist case in which only the position angles follow the original galaxy profile (red), the ellipticity case in which only changes of ellipticity are allowed (green), and the twist + ellipticity variation case (blue). The different mock images, created with the lens mass profile that lenses a circular Sérsic background source, are modelled with a PEMD + shear lens model and a circular Sérsic for the source model. The definition of the first nine quantities is listed in Table 5.1. (*Continued on next page.*)

Figure 5.7 (*Continued*): Population results based on mock mass profiles following the ellipticity and position angle variations observed in local galaxies, using the Kormendy et al. (2009) sample.

Notes (*Continued*). The χ^2 is the reduced imaging χ^2 of the fit. The last four quantities are defined in Section 5.2.2.3. Since these latter quantities are specific to the different galaxies and do not involve any modelling, they are plotted in black. The diagonal cells are KDEs of the marginalized quantity. Only the fits with $\chi^2 < 1.5$ are considered for the KDE distributions.

Quantity	Difference between			Quantity description
	input	fiducial	fitted	
$\delta\theta_{\rm E}$	x		x	Einstein radius [$''$]
Δq		x	x	Lens axis ratio
$\Delta\phi_{\rm elli}$		x	x	Lens position angle [°]
$\Delta\gamma_{\rm ext}$		x	x	Shear strength
$\Delta\phi_{\rm ext}$		x	x	Shear position angle [°]
$\delta slope$	x		x	Power-law slope
$\Delta R_{\rm sersic}$		x	x	Source Sérsic radius [$''$]
$\Delta n_{\rm sersic}$		x	x	Source Sérsic index
ΔH_0		x	x	Hubble constant [$\mathrm{km\,s^{-1}\,Mpc^{-1}}$]

Table 5.1: Definition of the parameters used to compare models.

Notes. "Fiducial" stands for the retrieved value of the parameter for the fiducial case with no twists and no ellipticity changes. "Input" stands for the quantity calculated specifically for the mock, created with ellipticity changes and/or twits, taken at the Einstein radius for the effective slope.

profile, as indicated by the poorer χ^2. The slope, $R_{\rm sersic}$, $n_{\rm sersic}$, and H_0 also have a broader distribution due to the ellipticity gradients than the twist-only galaxies: the parameter population distributions for ellipticity gradients are between 2.6 and 4.1 times broader than the twists gradients for the quantities cited above. Third, the correlation between the slope, $R_{\rm sersic}$, and H_0 is similar to the correlation reported earlier with the sample from Kormendy et al. (2009). Aside, The correlation between the retrieved axis ratio and the changes in ellipticity inside the Einstein radius is trivial. Finally, the galaxies displaying the strongest ellipticity gradients, mostly the ellicular galaxies, are not well fit, as indicated by the χ^2. The twist-only galaxies, on the other hand, are all fit well.

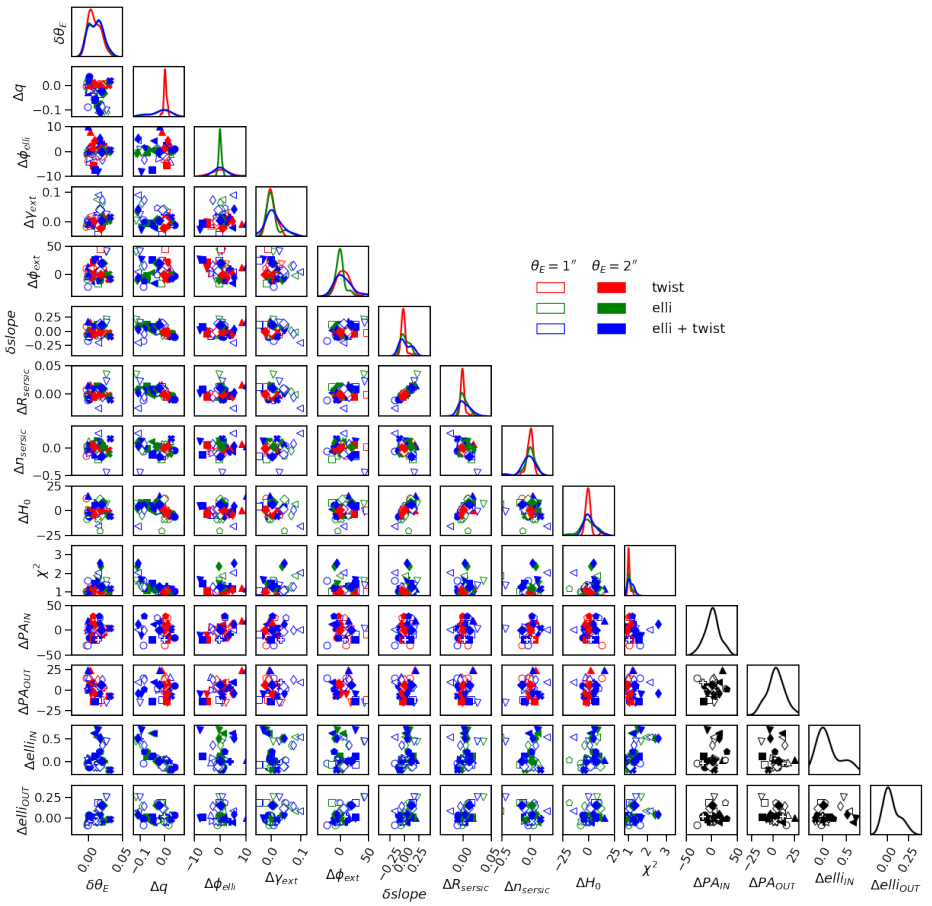

Figure 5.8: Population results for the EAGLE sample from Mukherjee et al. (2018), based on 12 fiducial galaxies.

Notes. The description is the same as for Figure 5.7. The markers of the three ES galaxies are triangles pointing to the left, triangles pointing to the bottom, and the diamond shape. We recall that only the fits with $\chi^2 < 1.5$ are considered for the KDE distributions.

Input			
	Twist	Elli	Elli + twist
ΔPA_{IN}	$1._{-6.}^{+13.}$	-	$1._{-6.}^{+13.}$
ΔPA_{OUT}	$-0.6_{-8.9}^{+2.2}$	-	$-0.6_{-8.9}^{+2.2}$
$\Delta elli_{IN}$	-	$-0.05_{-0.04}^{+0.12}$	$-0.05_{-0.04}^{+0.12}$
$\Delta elli_{OUT}$	-	$0.006_{-0.050}^{+0.035}$	$0.006_{-0.050}^{+0.035}$
Results			
	Twist	Elli	Elli + twist
$\delta\theta_E$	$6.5_{-6.8}^{+5.8} \times 10^{-3}$	$4.7_{-3.6}^{+7.3} \times 10^{-3}$	$5.8_{-4.8}^{+7.1} \times 10^{-3}$
Δq	$0.0_{-2.3}^{+2.1} \times 10^{-3}$	$0.0_{-1.6}^{+2.1} \times 10^{-2}$	$0.3_{-1.8}^{+1.7} \times 10^{-2}$
$\Delta\phi_{\rm elli}$	$0.1_{-1.2}^{+1.6}$	$1.7_{-5.3}^{+3.4} \times 10^{-1}$	$0.1_{-1.0}^{+0.9}$
$\Delta\gamma_{\rm ext}$	$0.0_{-5.0}^{+5.1} \times 10^{-3}$	$0.3_{-0.8}^{+1.3} \times 10^{-2}$	$0.7_{-1.1}^{+0.9} \times 10^{-2}$
$\Delta\phi_{\rm ext}$	$-0.3_{-1.9}^{+3.8}$	$0.9_{-4.8}^{+5.9}$	$1.8_{-9.1}^{+4.3}$
$\delta slope$	$-0.6_{-1.6}^{+2.4} \times 10^{-2}$	$-0.2_{-6.1}^{+7.6} \times 10^{-2}$	$-1.4_{-4.4}^{+3.4} \times 10^{-2}$
$\Delta R_{\rm sersic}$	$-0.0_{-1.8}^{+1.4} \times 10^{-3}$	$-0.2_{-4.6}^{+5.4} \times 10^{-3}$	$-0.8_{-3.0}^{+4.5} \times 10^{-3}$
$\Delta n_{\rm sersic}$	$-3.7_{-4.3}^{+2.7} \times 10^{-2}$	$0.2_{-7.5}^{+6.1} \times 10^{-2}$	$0.8_{-6.3}^{+7.6} \times 10^{-2}$
ΔH_0	$-0.3_{-0.9}^{+1.2}$	$-0.8_{-3.1}^{+4.0}$	$-0.6_{-3.0}^{+2.2}$

Table 5.2: Kormendy population results.

Notes. Input sample properties (top) and statistics of the model results (bottom) for each azimuthal variation subsample. See Section 5.2.2.3 for the comprehensive population description. See Table 5.1 for the retrieved quantities definition and Figure 5.7 for the visualisation of the results. Only fits with $\chi^2 < 1.5$ are considered within the population results.

5.3.2.3 Comparison of the two samples

We now compare the distributions of fitted quantities for our two mock populations in detail. Figure 5.10 compares the histograms of the two population results when both twists and ellipticity changes are present. We anticipate that the combined set of EAGLE and Kormendy covers a wide range of azimuthal variations within which the real population is expected to lie. While the extreme changes in ellipticity are sometimes difficult to model, most twists and ellipticity changes are easily absorbed by the model, which is a simple power-law ellipsoid model and shear. Figure 5.9 shows typical fit residuals when the azimuthal variations are well (top) and poorly (bottom) absorbed in the model. The galaxies based on the simulated sample display the most extreme ellipticity variations. The reason is that this sample includes ellicular galax-

Input			
	Twist	Elli	Elli + twist
ΔPA_{IN}	$2._{-14.}^{+11.}$	-	$2._{-14.}^{+11.}$
ΔPA_{OUT}	$-2.8_{-7.6}^{+8.5}$	-	$-2.8_{-7.6}^{+8.5}$
$\Delta elli_{IN}$	-	$-0.04_{-0.12}^{+0.42}$	$-0.04_{-0.12}^{+0.42}$
$\Delta elli_{OUT}$	-	$0.02_{-0.13}^{+0.06}$	$0.02_{-0.13}^{+0.06}$
Results			
	Twist	Elli	Elli + twist
$\delta\theta_E$	$0.6_{-0.5}^{+1.1} \times 10^{-2}$	$1.2_{-1.2}^{+0.8} \times 10^{-2}$	$1.3_{-1.3}^{+0.5} \times 10^{-2}$
Δq	$1.5_{-2.9}^{+6.8} \times 10^{-3}$	$-1.2_{-8.4}^{+2.7} \times 10^{-2}$	$-2.2_{-6.8}^{+3.5} \times 10^{-2}$
$\Delta\phi_{\text{elli}}$	$0.4_{-2.5}^{+2.3}$	$-0.4_{-4.3}^{+5.6} \times 10^{-1}$	$-0.0_{-3.2}^{+3.8}$
$\Delta\gamma_{\text{ext}}$	$-0.0_{-1.0}^{+1.6} \times 10^{-2}$	$-0.1_{-0.4}^{+4.0} \times 10^{-2}$	$0.4_{-1.2}^{+3.8} \times 10^{-2}$
$\Delta\phi_{\text{ext}}$	$7.6_{-9.7}^{+7.0}$	$-0.1_{-6.9}^{+4.0}$	$0.3_{-0.9}^{+1.9} \times 10^{1}$
$\delta slope$	$-1.5_{-2.6}^{+1.4} \times 10^{-2}$	$0.6_{-6.4}^{+9.9} \times 10^{-2}$	$-0.0_{-0.7}^{+1.3} \times 10^{-1}$
ΔR_{sersic}	$-1.0_{-1.7}^{+2.0} \times 10^{-3}$	$0.9_{-4.7}^{+7.2} \times 10^{-3}$	$1.2_{-7.9}^{+8.7} \times 10^{-3}$
Δn_{sersic}	$1.0_{-5.1}^{+2.2} \times 10^{-2}$	$0.0_{-1.1}^{+0.8} \times 10^{-1}$	$-2.1_{-8.7}^{+9.2} \times 10^{-2}$
ΔH_0	$-0.5_{-2.2}^{+1.3}$	$0.0_{-4.4}^{+8.1}$	$1.3_{-4.5}^{+5.2}$

Table 5.3: EAGLE population results.

Notes. Distributions of azimuthal variations for the sample (top) and associated population results (bottom). See Section 5.2.2.3 for the comprehensive population description. See Table 5.1 for the retrieved quantities definition and Figure 5.8 for the results visualisation. Only fits with $\chi^2 < 1.5$ are considered.

ies, which are absent from the sample studied by Kormendy. For the two samples, the changes in position angles are absorbed by the position angle of the modelled ellipsoid and the orientation of the shear. The variations in ellipticity have an impact on the retrieved shear strength, with amplitudes depending on the sample. The same observation can be made for the slope of the power-law ellipsoid, the source size, and H_0. Moreover, no bias is observed, the recovered median value of H_0 being less than half a σ away from the fiducial one. The ΔH_0 distribution for the sample based on EAGLE galaxies is slightly broader, however, as they display a broader range of ellipticity variations (see Section 5.2.2.3).

The strong correlation between H_0, the power-law slope, and the source size when ellipticity gradients are present is similar to what would be observed in presence of a mass sheet degeneracy (MSD), and it appears in both samples. This can be qualita-

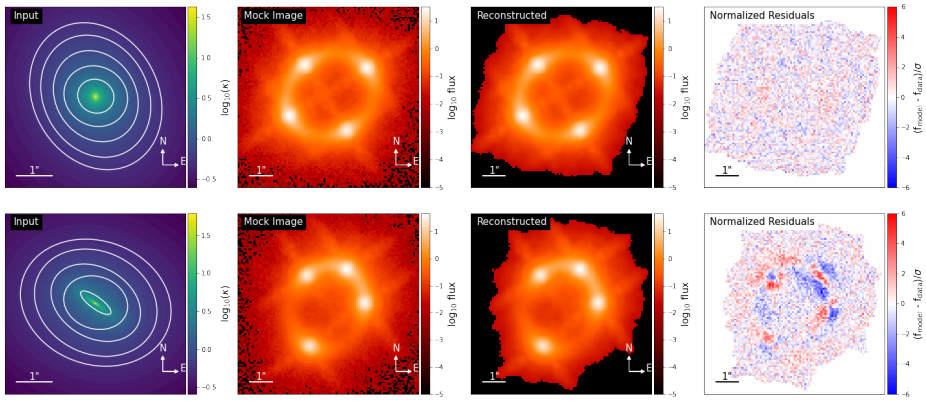

Figure 5.9: Example of a fit when ellipticity gradients and twists are well absorbed within the model (top) and when these azimuthal variations leave ubiquitous patterns in the residuals (bottom).

Notes. From left to right: Convergence map of the input mass profile displaying twists and ellipticity gradients, mock image created with this mass profile, best power-law + shear model fitting the mock image, and residuals between the image and the model. In most cases, the residuals display no patterns. When extreme changes in ellipticity are displayed in the input mass model, as for ellicular galaxies, the azimuthal variations may not be absorbed by the model. In this case, the residuals display recognisable patterns that are unlikely to be mistaken as lens light or any other well-behaved light component.

tively understood from the bottom panel of Figure 5.2. To compensate for the missing or excess mass introduced by ellipticity gradients, the slope of the density profile of the model needs to be modified and rescaled to conserve the mass within the Einstein radius. A pure mass sheet transformation (MST) acts only as a rescaling of a radial mass density profile. Nevertheless, the ellipticity gradients, which are azimuthal variations, trigger an MST-like degeneracy. The pure MST effects have been mitigated so far: We used power-law mass profiles for both the input lens mass and the model, whereas an MST cannot transform a power law into a power law. It may therefore be important to relax the assumption on the radial density profile to better investigate the interplay between the radial mass profile and the azimuthal variations. We thus added Appendix 5.B to explore this question further by creating mock lenses following a composite mass model instead of a power law. We did not observe an additional effect of the interaction of the radial and azimuthal mass profile. The MST due to the radial mass profile and the MST-like degeneracy due to azimuthal variations seem to act independently.

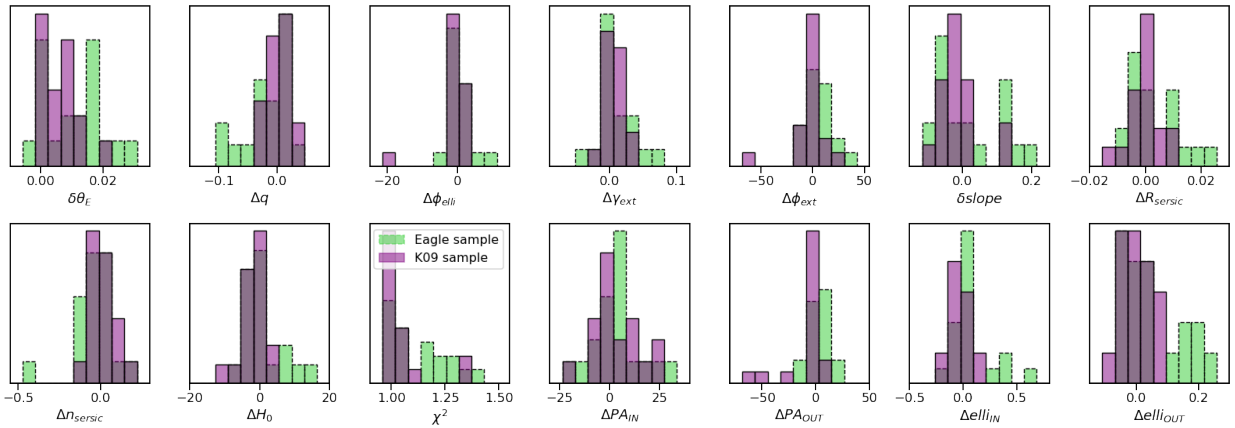

Figure 5.10: Comparison of results for the sample of mocks based on hydro-simulated morphologies (dashed green) and for the results based on observed morphologies (plain red) when both ellipticity variations and twists are present.

Notes. Both variations are needed to mimic realistic galaxies. The displayed quantities are identical those of Figures 5.7 & 5.8. Only the fits displaying χ^2<1.5 are considered.

5.4 Summary and conclusions

Isophotal twists and ellipticity variations have been detected in elliptical galaxies in the local environment as well as at higher redshifts (see, e.g., Fasano & Bonoli 1989; Keeton et al. 2000; Hao et al. 2006; Pasquali et al. 2006; Kormendy et al. 2009). Lensing galaxies, which mostly are massive ellipticals, can also display these features (see, e.g., Keeton et al. 2000; Fadely et al. 2010). However, most lensing galaxies are modelled with a simple ellipsoidal shape (see, e.g., Treu & Marshall 2016; Shajib et al. 2019; Wong et al. 2020). Characterising the influence of this assumption has been the goal of this Chapter.

We have followed a method similar to that of Van de Vyvere et al. (2022a), i.e. Chapter 4. We created mock lensing galaxies that displayed twists and/or ellipticity gradients using the method proposed by Schramm (1994). It consists of superposing finite elliptical slices of constant surface density, which have different sizes, mass, orientations, and ellipticities, to mimic an arbitrary mass profile. The lensing potential and deflection angle of each slice are known analytically, and were summed to compute the lensing quantities associated with the whole mass profile. We then simulated gravitationally lensed systems and modelled them with a mass profile characterised by a single orientation and ellipticity. The analysis of the retrieved parameters allowed us to quantify the impact of the scarcity of azimuthal structures in the lens modelling.

We first simulated lensing galaxies with position angles and ellipticities that varied linearly with radius to acquire a heuristic understanding of the role of each of these two azimuthal structures on lensed images. We found that moderate azimuthal changes do not preclude good modelling of the systems. The twists in the inner regions of the galaxy mainly impact the orientation of the fitted ellipsoids, while twists in the outer regions of the galaxy rotate the position angle of the retrieved shear. For ellipticity gradients in the outer part of the galaxy, the shear strength and orientation are modified instead. Ellipticity gradients in the inner part mainly impact the ellipticity of the modelled density profile. Ellipticity variations also influence other parameters, however, such as the power-law slope, the source size, and the time-delay distance, which is a proxy for H_0. This is explained by a balance of the internal and external shear that is achieved in the modelling by an adjustment of the radial profile, thus modifying H_0, and accommodating the source size accordingly. This confirms the statement by Kochanek (2021) that fitting a lensing galaxy displaying ellipticity gradients with a homoeidal power-law profile would lead to a bias on the slope to balance the internal and external shear introduced by the change of ellipticity, and would thus bias H_0.

To quantify the impact of twists and ellipticity gradients on lens parameters and cosmography, we simulated and modelled populations of lensing galaxies displaying realistic morphologies. Two populations of data-motivated azimuthal variations were considered: the light profiles of observed nearby galaxies (Kormendy et al. 2009), and

the mass profiles of galaxies from the EAGLE hydro-dynamical simulations (Schaye et al. 2015). Both samples display similar position angle variations. Ellicular galaxies in the EAGLE sample yield a wider population of ellipticity gradients, however, as the sample contains galaxies displaying drastic variations in their ellipticity profile (e.g., an axis ratio varying by 0.5 within 4 kpc). While extreme ellipticity variations are difficult to model, all the twists we tested were easily absorbed in the modelling. When both twists and ellipticity gradients are present in the mock lensing galaxy, the effect of each simply add up. The modelling of a single lens can reach a bias on the shear orientation of 20°, while the shear strength can rise up to twice its fiducial value. The H_0 inference can also be biased up to 10 $\mathrm{km\,s^{-1}\,Mpc^{-1}}$. Nevertheless, the influence of the azimuthal variations averages out at a population level. The median H_0 value is centered on the fiducial value within less than 0.5σ for both observed and hydro-simulated morphologies. Other parameters such as the shear strength, shear orientation, and the ellipsoid axis ratio and position angle are also centered on their fiducial values at a population level. The absence of ellicular galaxies yields narrower distributions of the fitted parameters in the observation-based sample compared to the hydro-simulation sample.

The reported results on a lens-by-lens case may cause concern, but fortunately, galaxies are not transparent, and twists and ellipticity gradients may be readily detectable in their luminosity profile. The lens-light variations are a sufficiently good proxy of the mass distribution azimuthal patterns according to the analysis we performed of elliptical galaxies from hydro-dynamical simulations. By comparing light and mass in EAGLE, we found that the variations in orientation and axis ratio in the light are similar to the variation in the mass. The light is thus a good tracer of the position angle and ellipticity fluctuations in the inner 15 kpc of elliptical galaxies. The precision of the instrument point spread function, which blurs and circularizes the features of the galaxies, will nevertheless play a role in the detection of azimuthal variations, especially in the inner parts of the galaxy.

In principle, kinematic information should also provide additional constraining power that can help to inform and model the existence of such structures. However, in practice, neither the data quality nor the kinematic models commonly employed in lensing contexts are sufficient to this degree as yet. In the context of lens modelling, many assume spherical Jeans velocity dispersions (e.g., Wong et al. 2017; Birrer et al. 2019; Rusu et al. 2020), or the most advanced models assume axisymmetry (e.g., Yıldırım et al. 2021), and therefore do not take azimuthal structures into account. While methods exist to create mock kinematics with additional structure (e.g., triaxiality via Schwarzschild modelling), these structures can currently not be modelled jointly with lens modelling. As kinematic simulation and lens modelling codes coevolve, it might be possible in the future to better constrain a complex galaxy with azimuthal variations using spatially resolved kinematic information.

To conclude, this Chapter explores the effect of iso-density twists and elliptic-

ity gradients on lensing cosmography analyses, as such azimuthal variations exist in early-type galaxies. The impact of twists on the modelling is in general rather marginal. Ellipticity gradients, on the other hand, can introduce substantial amount of shear that can be partly absorbed by the lens models, with an impact on the value of H_0 on a single lens basis. However, no bias is observed at the population level. We did not construct our samples to perfectly match the true population of lensing galaxies, but we chose it with a rather broad diversity representative of real systems. An overpopulation of some subsamples might change the broad picture slightly, but the latter indicates that the impact of ellipticity gradients and twists is generally small or averages out. If a population analysis is not feasible, a lens-light analysis should enable a rough estimation of the azimuthal variations. It may be important to look at the light profile outside the Einstein radius as ellipticity gradients in these regions can introduce substantial shear. If azimuthal variations are detectable in the isophotes, a more complex modelling scheme can consequently be applied to increase the azimuthal freedom in the mass model and assess the presence of a possible systematic bias.

More broadly, ellipticity gradients and twists are not the only type azimuthal variations that can be considered. Van de Vyvere et al. (2022a) (i.e. Chapter 4) also explored the role of undetected azimuthal variations in the mass on the model and specifically H_0, but focused on the role of the multipolar component of order 4, which corresponds to boxyness and discyness. They found that boxyness or discyness in the mass introduces specific patterns in the lensed arcs. Depending on the signal-to-noise ratio and on the complexity allowed in the source reconstruction, these patterns could be absorbed in the modelling with purely ellipsoidal power-law mass profiles. For ellipticity gradients and twists, the patterns are almost always unnoticed as they are easily modelled by changing the azimuthal components (orientation and strength of shear or ellipticity) and/or by modifying the radial power-law mass model. Both ellipticity gradients and multipoles of order 4 have impacts on H_0 up to a bias of 15%. However, a realistic combined population of boxy and discy galaxies averages the H_0 bias to be below the percent level, and similarly, a sample of early-type galaxies displaying a variety of ellipticity gradients also averages out the bias down to the percent level. A combination of all the different types of azimuthal variations (i.e., boxyness or discyness, ellipticity gradients, and twists) was not explored in this thesis. Nevertheless, as both multipolar variations and ellipticity gradients have little bias on H_0 at a population level, we expect that a sample of galaxies displaying a combination of both would also lead to an unbiased cosmological inference, even if cosmological results of individual lensing systems could be more widely spread.

5.A Example profiles

In the Chapter, we constructed mock lensing galaxies with varying azimuthal profiles. Five of these position angle and axis ratio profiles are presented in Figure 5.11. The convergence maps created with slices following the different azimuthal variation profiles are shown in Figure 5.12. In Section 5.2.2.2, monotonic variations of position angle or ellipticity were considered. The profile used is displayed as a purple long-dashed line. Two data-motivated samples of azimuthal variations were considered in Section 5.2.2.3: the morphologies based on observed local elliptical galaxies analysed by Kormendy et al. (2009), and the morphologies based on the density of EAGLE hydro-simulated galaxies. Two profiles of each sample are presented in Figure 5.11: with dashed blue and dash-dotted orange lines for the morphologies based on hydro-simulations, and as plain green or dotted red lines for those based on observations.

5.B Composite mass profiles

To explore the role of radial mass profile in conjunction with azimuthal variations such as twists or ellipticity gradients, we created new samples of mock lensing images based on composite lensing mass profiles consisting of a baryonic and a dark matter component. Unlike the power-law profile, this mass profile does not display the same radial slope at every galactocentric radii.

The baryonic component is usually represented with a Sérsic or a Chameleon profile (Dutton et al. 2011; Suyu et al. 2014; Gomer et al. 2022). The Chameleon profile, which is the difference between two nonsingular isothermal ellipsoids (NIE), mimics the well-known Sérsic profile for Sérsic indexes between 1 and 4 and has the advantage of being less computationally demanding for the calculation of lensing quantities. The mathematical formulation we used for this profile is introduced in Equation (4.10) and reminded here:

$$\kappa(\theta_1,\theta_2) = \frac{L_0}{1+q}\left(\frac{1}{\sqrt{\theta_1^2+\theta_2^2/q^2+4w_c^2/(1+q)^2}} - \frac{1}{\sqrt{\theta_1^2+\theta_2^2/q^2+4w_t^2/(1+q)^2}}\right)$$

where (θ_1,θ_2) are defined within the coordinate system oriented along the main axis of the Chameleon ellipsoid, L_0 is a normalisation factor, q is the axis ratio, w_c is a proxy for the core radius of the first NIE, and w_t is that of the second NIE.

The dark matter component is commonly simulated with a Navaro-Frenk-White mass model (NFW ; Navarro et al. 1996). The halo of dark matter thus follows Equa-

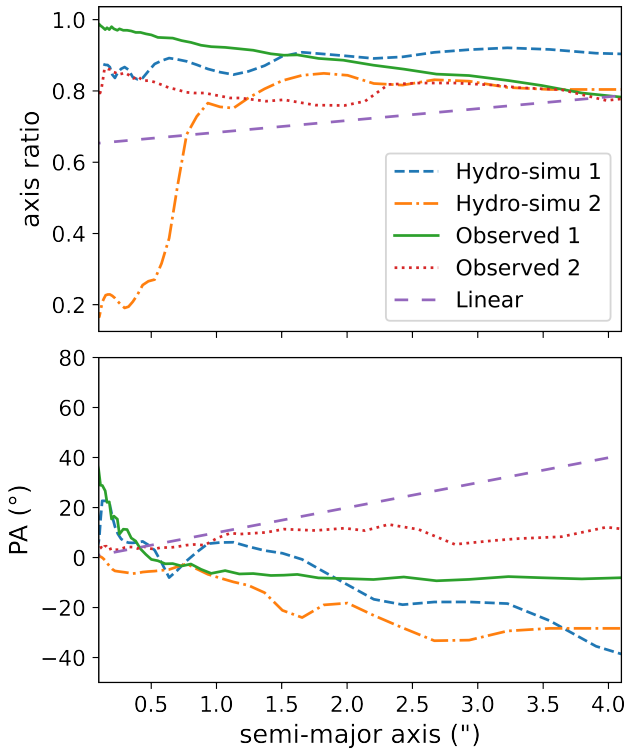

Figure 5.11: Example variations with semi-major axis of axis ratio (top) and position angle (bottom) from hydro-simulated, observed, and custom-designed galaxies.

Notes. The "Hydro-simu 2" curves depict the morphology of an ellicular galaxy, i.e. an early-type galaxy displaying a medium-sized disk component in the center. The position angle profiles are translated by a constant angle to help visualisation. The corresponding convergence maps are also shown in Figure 5.12.

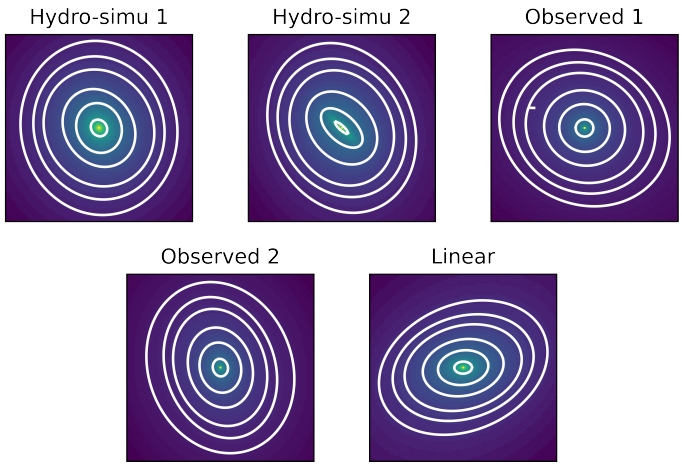

Figure 5.12: Examples of convergence maps created with slices for hydro-simulated, observed, and custom-designed galaxies that display axis ratio and position angle variations with semi-major axis.

Notes. The corresponding azimuthal profiles of the different galaxies are displayed in Figure 5.11.

tion (4.11), that is:

$$\rho(r) = \frac{\rho_0}{(r/r_s)(1+r/r_s)^2}$$

where ρ is the 3D mass density, ρ_0 the central mass density, and r_s is the scale radius at which the profile smoothly switches between a $\rho \propto 1/r$ relation and a $\rho \propto 1/r^3$ proportionality. The lensing quantities formulation in 2D of such mass density in pseudo-elliptical symmetry can be found in Golse & Kneib (2002).

The composite mass profile we chose to simulate had the following characteristics. The Einstein radius was set to $1''$, which is typical of observed Einstein radii. Other characteristics were chosen such that in the end, the baryonic profile mimicked a Sérsic with $R_{\rm eff} = 1.7''$ and $n_{\rm sersic} = 4$, corresponding to a total mass of 0.28×10^{12} $M_\odot$, and the dark matter profile had physical size of $R_{200} = 0.25$ Mpc and $M_{200} = 2.4 \times 10^{12}$ $M_\odot$. The latter is defined as the mass enclosed in the radius R_{200} in which the average density is 200 times the critical density of the universe at the considered redshift. This setup is arbitrary but representative of real lensing galaxies (Gomer et al. 2022). Such a radial mass profile is presented in Figure 5.13.

The radial mass profile was created using the azimuthal average of the elliptically symmetric mass density at each radius. However, the azimuthal profile shows that for

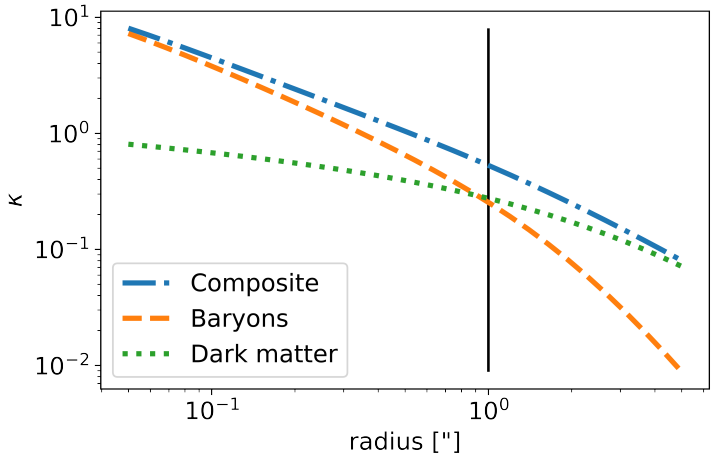

Figure 5.13: Radial profile of the composite mass model (dash-dotted blue line), made of a baryonic component following a Chameleon profile (dashed orange line) and a dark matter component simulated with an NFW mass profile (dotted green line).

Notes. The vertical black line indicates the Einstein radius.

an elliptical composite mass profile, the logarithmic slope of the profile is not constant for a circular azimuthal cut because it probes different elliptical radii of a profile with a varying slope with radius, as shown in Figure 5.14.

With the radial profile as simulated above, mock lensing images can be created for the different twist and ellipticity profiles of the two populations of data-motivated azimuthal variations, that is, the observation-based an the hydro-simulation-based morphologies. These images were then modelled with a PEMD and a shear, following the same procedure as implemented before.

Figures 5.15 & 5.16 display the results when both twists and ellipticity changes are considered for the mocks based on either an SIE input mass profile and Einstein radius of $1''$ (dashed green), or a composite input mass profile (plain red). Figure 5.15 specifically focuses on results from mock lensing galaxies based the isophotes of the observed sample, and Figure 5.16 displays those based on the iso-density contours of the hydro-simulated sample (see Section 5.2.2.3 for the sample details). Only fits with $\chi^2 < 1.5$ were considered. For the sample based on observed morphologies, all the fits have χ^2 below the cutoff. This is not the case for the sample based on simulation: 9 (10) out of 12 mock images with a composite (isothermal) radial lens profile were fit to the required level. The galaxies leading to poor χ^2 beyond the cutoff are not systematically the same for the two radial profiles (i.e., composite or isothermal).

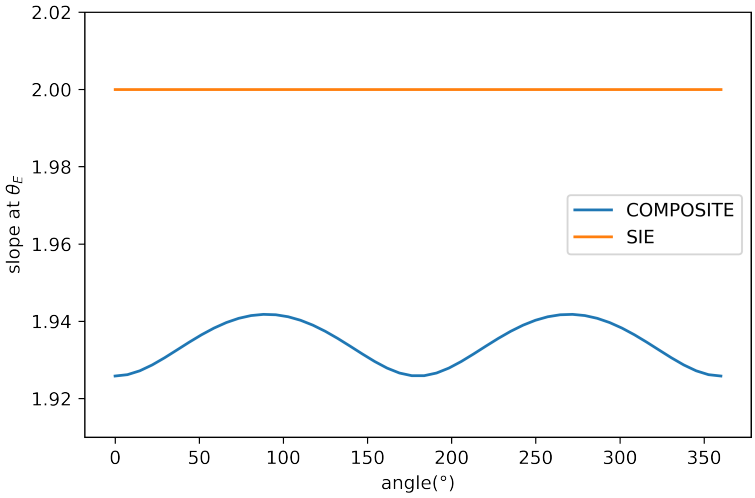

Figure 5.14: Circular azimuth cut of the profile slope for an SIE (orange) and the composite mass profile (blue) described in this section, considering a typical mass density axis ratio of 0.8 for both components, taken at the Einstein radius θ_E=1″.

Compared to the models of the isothermal mock lensing systems, the parameters of the models resulting from composite mocks are more widely spread in terms of shear angle, slope, source size, and H_0 for azimuthal variations based on either an observational sample (Figure 5.15) or a hydro-simulated sample (Figure 5.16). This extent in these characteristics is understood as the imprint of the variation in slope with angle for a given radius, as shown in Figure 5.14. Depending on the configuration and the ellipticity, the slope distributions even of mocks displaying neither twist nor ellipticity gradients are between twice and three times broader for the composite mass profile than for the isothermal profile. This scatter on the slope is additionally broadened by the ellipticity variations, hence the twice or three times larger scatter in ΔH_0 for the composites mocks compared to the isothermal mocks.

The interplay between the radial profile and the azimuthal variations does not add bias to H_0. Even if the MSD induces a shift in the central value of the H_0 distribution for the composite mocks – the H_0 distribution for the composite mocks is centered on 60 km s^{-1} Mpc^{-1} instead of 70 km s^{-1} Mpc^{-1} (see Birrer et al. (2020) for a discussion on how to mitigate this degeneracy)–, the ΔH_0 distributions (see Table 5.1 for definition) are centered on 0 for the composite mocks, similarly as for the isothermal mocks.

To summarize, the results of the modelling of composite radial mass profile are similar to those with an isothermal radial mass profile: the same correlations are ob-

served, and no additional bias on H_0 is observed due to the interplay between radial and azimuthal variations. The only noticeable difference is the larger scatter of the distributions of the composite results. It is understood as the manifestation of an intrinsic property of the composite mass models independent of the azimuthal variations, however. The mock composite mass profile thus does not seem to interact more with the input azimuthal variations than a power-law mass profile does.

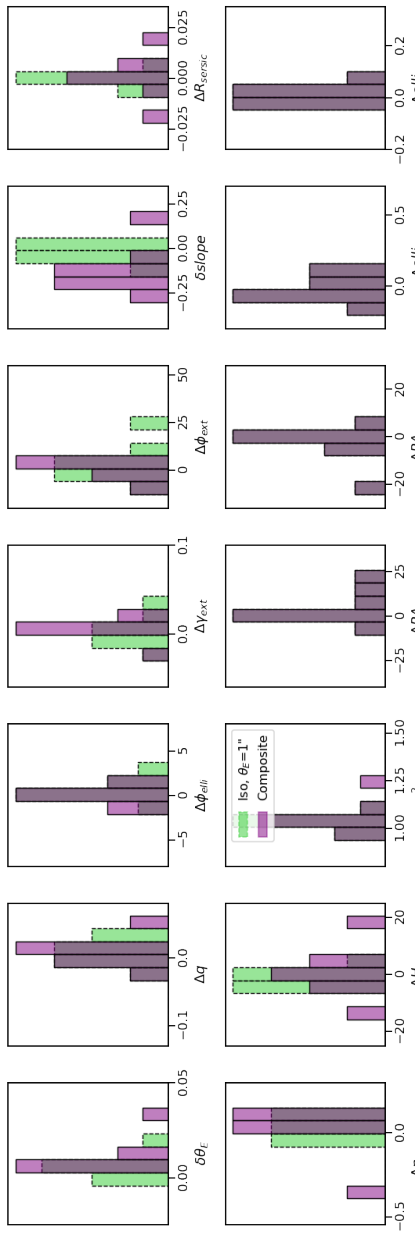

Figure 5.15: Comparison between fitted parameters of mock images created with either isothermal (dashed green) or composite radial mass profiles (plain red). The mock lensing mass models display both ellipticity changes and twists based on the **observed morphologies**, using the Kormendy et al. (2009) sample.

Notes. Only $\theta_E = 1''$ lensing galaxies are displayed for the isothermal cases in order to match the Einstein radius of the composite mock images samples. Only fits with resulting $\chi^2 < 1.5$ are considered. The four right cells of the second row display identical distributions, as the same population of twists and ellipticity changes are used to create the composite and the SIE mocks, and all the fit results have sufficiently low χ^2.

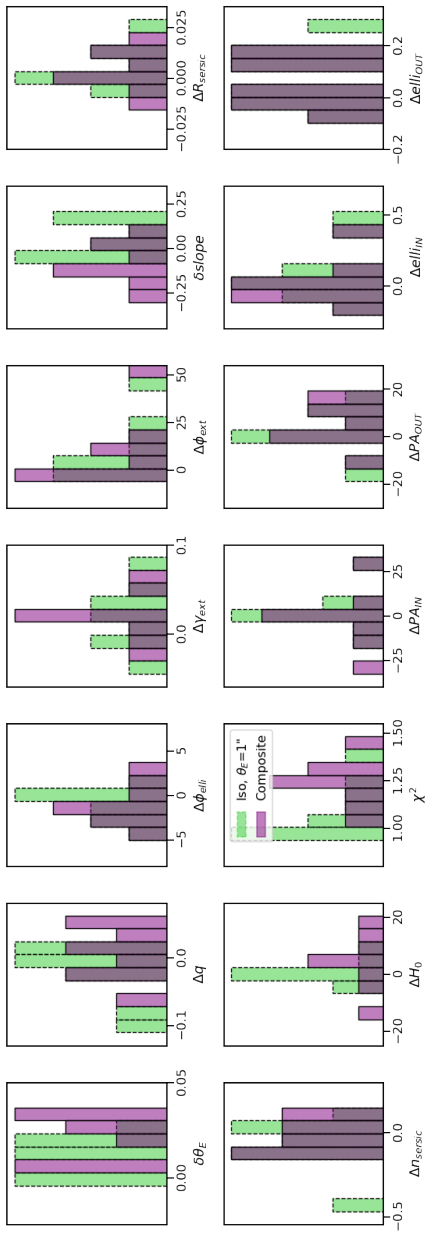

Figure 5.16: Comparison between fitted parameters results of mock images created with either isothermal (dashed green) or composite radial mass profiles (plain red). The mock lensing mass models display both ellipticity changes and twists, based on the **hydro-simulated morphologies**, using EAGLE galaxies from Mukherjee et al. (2018).

Notes. Only $\theta_E = 1''$ lensing galaxies are displayed for the isothermal cases in order to match the Einstein radius of the composite mock images samples. Only fits with resulting $\chi^2 < 1.5$ are considered. Due to the χ^2 cut, the displayed distributions of ellipticity gradient and twists are slightly different.

CHAPTER 6

CONCLUSION

6.1 Summary and discussion

This thesis takes place in the context of using time-delay lenses to perform a **cosmographic inference**. Time-delay lensing is one out of several probes which allows one to infer the Hubble constant. As introduced in Section 1.1, the inference of the Hubble constant based on early-time probes, i.e. using the CMB and BAO, is currently in tension with the inference of H_0 originating from the late-time probes, such as the Cepheids and type Ia supernova used to construct a distance ladder (Abbott et al. 2018; Riess et al. 2019; Verde et al. 2019; Freedman et al. 2020; Pesce et al. 2020; Philcox et al. 2020; Planck Collaboration et al. 2020; Schombert et al. 2020; Wong et al. 2020; Blakeslee et al. 2021). This tension may originate from under-estimation of the errors of one or several methods, or can be due to a systematic bias, or may be the hint of the need of a profound revision of our cosmological paradigm. The **time-delay method**, taking advantage of the difference in arrival time between the images of strongly lensed systems which is inversely proportional to H_0, is a late-time probe which is independent of any distance ladder and is thus a key method that can potentially break the tension in H_0 (see Wong et al. 2020; Birrer et al. 2020, among others). The accuracy and precision one can achieve with time-delay lenses however depends on the working hypotheses.

For many years, scientists used rather simple mass models for the lenses. Even with recent high resolution images and increased knowledge of elliptical galaxies,

more sophisticated models are surprisingly not often used: the simple models remain very efficient in reproducing the data down to the noise. Knowing whether this is because details of the galaxy morphology are not relevant for lensing or whether the simple models are strongly affected by degeneracies is an important question. Most of the past efforts focused on studying the impact of the assumption on the radial distribution of the mass (see Schneider & Sluse 2013, 2014; Birrer et al. 2020, among others). In this thesis, we have investigated the impact of the lack of azimuthal freedom in models. For this purpose, we had to create simulated systems. Depending on the purpose and on the target level of complexity of the mock lens, one can choose to either use analytical mock lensing galaxies (e.g. Kochanek 2020, 2021; Millon et al. 2020a; Ding et al. 2021b; Wagner-Carena et al. 2021), often following power-law mass distributions, or use pixelated lensing galaxies (e.g. Xu et al. 2015, 2016; Mukherjee et al. 2018; Denzel et al. 2020; Ding et al. 2021b), for instance based on hydro-dynamical simulations.

When emulating lensing systems using pixelated mass maps, one has to find a balance between the resolution of the map, its size, and the computational time needed to perform one or more simulations. The resolution of the map is generally constrained, either by the resolution of the Universe simulation used, or by pixel size of lenses light maps which the mass is based on through a mass-to-light ratio. There is however no specific prescription for the size: if one wants to take the whole mass and any pertubers in the vicinity of the galaxy into account, the map will generally extend up to the Virial radius or R_{200}, conversely, someone interested in the central part of the galaxy, which matters most for lensing, will cut the map at a few Einstein radii. By comparing lensed systems created with variety of **mass maps** cut at different radii and/or with different shapes of the **truncation** region, I found that artefacts mimicking physical deformation of the lensed images could appear (see Chapter 3). To summarize, the mass profiles of galaxies are cut with a specific shape, generally squared, when used as mass maps. This truncation does not follow the iso-density contours of the profile, hence creating an asymmetry by taking into account mass inside the border that is not balanced by its analog beyond the border. This excess of mass at specific locations at the edge of the map creates an artifact mimicking a shear. As no convergence is associated to shear, this subtlety is tricky to spot during cross-checks in the simulation of lensing systems. As a consequence, simulated lensing systems victims of this effect will generally be well modelled with an excessive shear component. This effect provides for instance an explanation for the ellipticity - shear correlation found by Mukherjee et al. (2018) in which the authors modelled mock lensing systems created with hydro-dynamically simulated mass maps extending to a few Einstein radii. While the correlation was originally interpreted as a modelling degeneracy, my work advocates for an explanation based on the artificial shear due to truncation. Another recent literature result hints towards the capture of such effect by neural networks trained on mock lensing systems created with truncated mass

maps (Adam et al. 2022). This will potentially introduce a bias on future applications of those neural networks on real data. Those two works where the truncation of the mass maps, at least partially, impacts the scientific conclusion of the study highlight the importance of proceeding carefully when creating simulations of lensing systems using truncated mass maps as the lens.

To study the impact of azimuthal structures in lensing analyses, I used analytical models as they allowed flexibility to create the desired profiles, while enabling to control and disentangle the effects of the different perturbations. The truncation issue thus did not arise, but it helped me keep in mind that asymmetries outside the Einstein radius can influence the lensed images morphology. In this thesis, I specifically focused on the main azimuthal structures present in elliptical galaxies, that is, boxyness and discyness, and the variations of ellipticity and position angle with radius. Those structures are often remnants of formation history and interactions with neighbouring objects, as well as being partially due to projection effects.

I first explored the impact on lensing analysis of multipolar structures of order 4, i.e. **boxyness** and **discyness** (see Chapter 4). Prior to this work, the impact of those structures on flux-ratio anomalies and images positions had been studied by Keeton et al. (2003); Xu et al. (2015); Gomer & Williams (2018), among others. However, the analysis of their impact on extended lensed features was still missing. By creating complex mass profiles to simulate lensing systems (with a quasar source embedded in a host galaxy) and modelling the latter with standard models used in nowadays lensing analyses, I found the following: if present in the lensing galaxy but not in the modelling procedure, the effect of boxyness and discyness is ubiquitously visible in the residuals for lensing systems simulated with high signal-to-noise. However, a decrease in data quality or an increase in freedom in the source light model allows one to model the lensing systems without noticing multipolar effect. In the latter case, the bias on the inferred H_0 value can reach several percent. Considering a population of lenses with multipolar strength observed in elliptical galaxies, the bias however averages out. Moreover, the broadening of the H_0 distribution in presence of multipoles is already implicitly taken into account in the quoted uncertainties of time-delay lensing analyses (e.g. in Wong et al. 2020). The results at a population level are reassuring for the future of time-delay lensing studies as the lensing community aims at increasing the number of lensing systems. Conversely, the cosmography inference based on a single lensing system is expected to be potentially biased. To cope with this effect, one may consider to include multipolar structures in the lens model. This has recently been performed by Powell et al. (2022) who modelled the high-quality radio observations of MG J0751+2716, both with and without multipolar structures. By increasing the model freedom with such azimuthal structures, the model significantly improved the statistical evidence, and the predicted effect on H_0 is of the order of a 3% change. Aside, Galan et al. (2022) simulated quasar-less lensing systems in which the lensing galaxy displays discyness, and successfully retrieved the multipolar

component using a wavelet-based perturbation modelling. While modelling boxyness and discyness is promising, the necessity of having high signal-to-noise data to detect them yet remains.

I then explored two other types of azimuthal variations: the **twists** of iso-density contours and the **variations of ellipticity** with radius (see Chapter 5). To the best of my knowledge, Keeton et al. (2000) is the only work in which a multi-component model was used to purposely account for changes of position angle and ellipticity of the lens mass to model a lensing system. Other works using multi-component models or non-parametric models will naturally allow for more azimuthal freedom than the conformal models, but rarely with the goal of accounting for a specific azimuthal variation. I thus investigated the impact of lack of azimuthal freedom in the modelling of lenses displaying ellipticity gradients and twists. Using the method introduced in Schramm (1994), I simulated lensing systems in which lensing galaxies display realistic twists and/or ellipticity gradients and found the following. Twists do not directly impact cosmological inference, but do influence the modelled shear orientation and strength. Ellipticity variations are more problematic, they impact the retrieved value of H_0, on top of modifying the radial slope of the fitted profile, the source radial profile, and the shear strength and orientation. The bias on H_0 fortunately averages out when inferred from a population of lensing galaxies. Both types of variations are almost always easily absorbed by the model, even if the images are high-quality data. The use of elliptical power laws is consequently sufficient to accurately retrieve H_0 for population analyses but may lead to biases for a single lens. The value and orientation of the shear is subject to variations due to both twists and ellipticity gradients. Recently, Cao et al. (2022) created mock lensing systems thanks to realistic mass maps, based on SDSS-MaNGA IFU data (Li et al. 2018, 2019), without explicitly emulating an external shear. They fitted those mock images with a power-law model + shear, and found a typical shear strength $\gamma_{\rm ext} = 0.015$. While 15% to 40% of the shear they recover can still be due to the truncation of the mass map which happens at 10-30 $\theta_{\rm E}$ – instead of 50 $\theta_{\rm E}$ recommended in Chapter 3 –, it mainly reflects the impact of twists and ellipticity gradients.

6.2 Further discussion

The **shear** retrieved in the modelling of lensing systems is influenced by several azimuthal deformations in the lens, generally unaccounted for in the modelling, and this thesis helped quantifying this effect. In time-delay strong lensing cosmography, one of the key elements to consider is the lens environment (see Section 1.2.2) as H_0 scales with $(1-\kappa_{\rm ext})$, where $\kappa_{\rm ext}$ is the external convergence due to the environment. By studying the density of galaxies in the vicinity of the lens and along the line-of-sight towards the source, and by comparing it to simulated environments, one can constrain the external convergence at the location of the lensed images. As each sim-

ulated line-of-sight is associated to both an external convergence and shear, one can use the modelled shear to further constrain the external convergence. At the light of my research, it appears that the strength and orientation of the modelled shear can be biased by a few to several percent. Using it as prior to infer $\kappa_{\rm ext}$ may lead to a similar systematic error on H_0. If models were including more azimuthal freedom, the retrieved shears could better represent the external contributions from galaxies in the environment and provide more reliable constraints on the external convergence. While this is conceptually feasible, this may require even higher quality data than state-of-the-art images, as my work showed that the latter are well modelled with elliptical power-law + shear models despite the presence of twists and ellipticity gradient. Not using the shear as a prior in the $\kappa_{\rm ext}$ inference thus remains the safest solution.

In this thesis as well as in lensing papers, the **data quality** is a crucial factor to consider. There is no adequate procedure to characterise the signal-to-noise ratio in presence of extended sources. I chose to describe the data quality mainly with an instrumental set-up, and the lensed and unlensed magnitude of the source. But by comparing with simulations performed by Galan et al. (2022), the importance of the source radial profile in describing the signal-to-noise was highlighted. Indeed, with similar instrumental set-ups and magnitudes, the patterns in the residuals were highly dependent on the extended source compactness. As a simple prescription, I advocate for comprehensive descriptions of the simulations, as done here as well as in Galan et al. (2022), to allow easy comparison of different works. The comparison between the data quality of simulated and real lensing systems however remains complex.

6.3 Ways forward

This thesis studied the impact of several azimuthal structures on lensing analyses and quantified their influence on H_0. This work opened a large panel of possible ways to go forward. First, now that we better understand the role of radial and azimuthal structures on the lensed images and H_0, a full end-to-end simulation framework that mimics all the complexity of real images, with lens light and realistic sources can be performed. Second, seeing the importance of azimuthal structures, I think that the information contained in the lens light, which was generally set aside in this thesis with simulations, should not be underexploited in real lensing systems as the azimuthal structures are imprinted in the light of the lens as well. Third, there is a clear correlation between the kinematic of a galaxy and the structures in its mass. As resolved kinematics becomes currently possible with lenses, using them should also improve the constraints on the mass of the lens, by helping classify the lens as well as by allowing a powerful joint image-kinematic modelling. Finally, one open question raised by this work was the degeneracy in the modelling between source light struc-

tures and lens mass structures. Better understanding this effect is also primordial to guarantee an accurate value of H_0.

Thanks to this thesis, different azimuthal structures have been studied and their impact been quantified thanks to simulations. The simulations could thus be put a step further by **combining all the azimuthal perturbations**, even some that were not considered here as the lopsidedness, and the presence of companions, for instance. Cao et al. (2022) initiated a step in that direction by creating lensing systems with quasar-less sources based on SDSS-MaNGA IFU data, and modelled them with elliptical power laws. They found systematic shear, partially due to artificial shear as discussed earlier, and also a predicted bias on $H_0 \sim 9\%$. The reported systematic bias on H_0 is however mainly explained by a mass sheet degeneracy between the true profile and the power-law model used. The part of this bias which is due to azimuthal structures can not be disentangled from the one originating from the mass sheet degeneracy. Using the hierarchical framework developed in Birrer et al. (2020) should mitigate the effect of the mass sheet degeneracy, by using the kinematic information of the lenses. Including lens light, simulating more realistic extended light sources, adding quasar images with associated time delays, getting rid of the artificial shear effect, and using the kinematic information would further improve the simulations from Cao et al. (2022) and allow an even better quantification of the achievable precision and accuracy on H_0 when using mass models with an elliptical symmetry.

Aside from simulating **lens light**, modelling and analysing it with great precision in real cases should help identifying the main azimuthal structures present in the mass of the lens. Nevertheless, the blending between (1) the PSF patterns at the quasar images, (2) the lensed extended source creating arcs, and (3) the lens light makes such analysis difficult and multi-band imaging may be required to disentangle the different components. Once isolated, the lens light can for instance be studied by fitting ellipses on its isophotes to retrieve their orientation, ellipticity, and multipolar component. By placing boundaries on the strength and type of azimuthal structures, one can either adopt an advanced modelling scheme if needed, or use a simple one while better apprehending the biases that may affect the modelling. The first step in that direction has been made by Shajib et al. (2022), who analysed the lens light of WGD 2038–4008 and found little multipolar patterns in the isophotes within the Einstein radius, leading the authors to keep their former modelling freedom, without including boxyness or discyness.

Similarly, **resolved kinematics** of the lens can help deduce the type of elliptical galaxy (see Section 1.3), hence potentially informing on the potential discyness or boxyness of the lensing galaxies. Aside, resolved kinematics may also become a very powerful tool when used in a joint lensing and kinematic modelling to constrain the mass model (see e.g. Barnabè & Koopmans 2007), instead of performing it in a post-modelling step, as usually done to break the MSD with velocity dispersion measurement done in apertures. The joint modelling of lensing and resolved kinematic infor-

mation has the disadvantage of being slow because the kinematic model requires a new calculation of stellar orbits at every iteration. Strategies to lower the computation time have been implemented by Barnabè & Koopmans (2007), but such a joint modelling remains demanding. Using the kinematic information in a post-modelling step requires less time: such practice assumes that the image modelling results comprehend the true solution and the kinematic only helps selecting the right region of the parameter space with a sampling[1]. Nevertheless, this assumption may not always be true, and directly driving the modelling to a suitable parameter space for both the imaging and kinematic data conceptually remains a cleaner solution. Moreover, resolved kinematics significantly brings more information than single aperture measurements and should be used in a consistent way with imaging data. To speed up the joint modelling of the image and the resolved kinematics, I am contributing to a project which aims at replacing the theoretical kinematic calculation by a neural network. This new tool might open a new way of using resolved kinematics in the modelling of lensing systems.

While kinematic information helps break the MSD, other degeneracies may also need to be handled to retrieve H_0 accurately. As seen in Chapter 4, the boxyness and discyness in the **mass of lenses** can be absorbed as **source structures** in the model. Even if the population analysis showed that H_0 was unbiased, this degeneracy involving azimuthal structures needs to be better understood. With a team, we started studying the influence of having more degrees of freedom either in the mass of the lens or in the light of the source, using several modelling codes. Studying the impact of the different prescriptions on the modelling results should allow us to better understand the quantities that are affected by such degeneracies. The outcome of such a study might be very insightful for the community.

6.4 The final word

Lensing, on paper as well as in practice, has a tremendous potential to help understand the Universe. After spending four years dissecting what could go wrong in lensing analyses, I am confident that lenses can be used as accurate cosmological probes. To reach a percent-level precision on H_0, one needs to understand the mass distribution of galaxies at a great level of detail. Such sensitivity to details shows that lensing may be an even better probe of galaxy mass distribution than anticipated, and demonstrates that a giant leap has been realised over the last decade. The scientific interest in accounting for these fine details which I observed in the lensing community tells me that the story is definitely not over and a lot of great work will continue to flourish in the coming years.

[1] Note that Birrer et al. (2020) revised the way kinematic can be used in post-modelling by explicitly including a mass sheet transformation and constraining its strength thanks to kinematic, among others.

BIBLIOGRAPHY

Abbott, T. M. C., Abdalla, F. B., Annis, J., et al. 2018, MNRAS, 480, 3879

Abbott, T. M. C., Aguena, M., Alarcon, A., et al. 2022, Phys. Rev. D, 105, 023520

Adam, A., Perreault-Levasseur, L., & Hezaveh, Y. 2022, arXiv e-prints, arXiv:2207.01073

Aiola, S., Calabrese, E., Maurin, L., et al. 2020, J. Cosmology Astropart. Phys., 2020, 047

Alam, S., Ata, M., Bailey, S., et al. 2017, MNRAS, 470, 2617

Barkana, R. 1998, ApJ, 502, 531

Barnabè, M. & Koopmans, L. V. E. 2007, ApJ, 666, 726

Barrera, B., Williams, L. L. R., Coles, J. P., & Denzel, P. 2021, The Open Journal of Astrophysics, 4, 12

Bartelmann, M. & Schneider, P. 2001, Phys. Rep., 340, 291

Bender, R., Doebereiner, S., & Moellenhoff, C. 1988, A&AS, 74, 385

Bender, R., Surma, P., Doebereiner, S., Moellenhoff, C., & Madejsky, R. 1989, A&A, 217, 35

Bianchini, F., Wu, W. L. K., Ade, P. A. R., et al. 2020, ApJ, 888, 119

Birrer, S. & Amara, A. 2018, Physics of the Dark Universe, 22, 189

Birrer, S., Amara, A., & Refregier, A. 2015, ApJ, 813, 102

Birrer, S., Amara, A., & Refregier, A. 2016, J. Cosmology Astropart. Phys., 2016, 020

Birrer, S., Shajib, A. J., Galan, A., et al. 2020, A&A, 643, A165

Birrer, S., Shajib, A. J., Gilman, D., et al. 2021, Journal of Open Source Software, 6, 3283

Birrer, S. & Treu, T. 2021, A&A, 649, A61

Birrer, S., Treu, T., Rusu, C. E., et al. 2019, MNRAS, 484, 4726

Blakeslee, J. P., Jensen, J. B., Ma, C.-P., Milne, P. A., & Greene, J. E. 2021, ApJ, 911, 65

Bolton, A. S., Burles, S., Koopmans, L. V. E., Treu, T., & Moustakas, L. A. 2006, ApJ, 638, 703

Bradley, L., Sipőcz, B., Robitaille, T., et al. 2020, astropy/photutils: 1.0.1

Breuval, L., Kervella, P., Anderson, R. I., et al. 2020, A&A, 643, A115

Brewer, B. J. & Lewis, G. F. 2008, MNRAS, 390, 39

Burke, W. L. 1981, ApJ, 244, L1

Cao, X., Li, R., Nightingale, J. W., et al. 2022, Research in Astronomy and Astrophysics, 22, 025014

Caon, N., Capaccioli, M., & D'Onofrio, M. 1993, MNRAS, 265, 1013

Cappellari, M. 2016, ARA&A, 54, 597

Chaware, L., Cannon, R., Kembhavi, A. K., Mahabal, A., & Pandey, S. K. 2014, ApJ, 787, 102

Chen, G. C. F., Fassnacht, C. D., Suyu, S. H., et al. 2021, A&A, 652, A7

Chen, G. C. F., Suyu, S. H., Wong, K. C., et al. 2016, MNRAS, 462, 3457

Chu, Z., Lin, W. P., Li, G. L., & Kang, X. 2013, ApJ, 765, 134

Claeskens, J. F., Sluse, D., Riaud, P., & Surdej, J. 2006, A&A, 451, 865

Courbin, F. & Minniti, D. 2002, Gravitational Lensing: An Astrophysical Tool, Vol. 608

Courbin, F., Saha, P., & Schechter, P. L. 2002, Quasar Lensing, ed. F. Courbin & D. Minniti (Berlin, Heidelberg: Springer Berlin Heidelberg), 1–54

Crain, R. A., Schaye, J., Bower, R. G., et al. 2015, MNRAS, 450, 1937

Denzel, P., Mukherjee, S., Coles, J. P., & Saha, P. 2020, MNRAS, 492, 3885

Despali, G., Vegetti, S., White, S. D. M., Giocoli, C., & van den Bosch, F. C. 2018, MNRAS, 475, 5424

Ding, X., Treu, T., Birrer, S., et al. 2021a, MNRAS, 501, 269

Ding, X., Treu, T., Birrer, S., et al. 2021b, MNRAS, 503, 1096

Djorgovski, S. & King, I. R. 1986, ApJ, 305, L61

Dressel, L. 2012, Wide Field Camera 3 Instrument Handbook for Cycle 21 v. 5.0

Du, W., Zhao, G.-B., Fan, Z., et al. 2020, ApJ, 892, 62

Dunlop, J. S., McLure, R. J., Kukula, M. J., et al. 2003, MNRAS, 340, 1095

Dutton, A. A., Brewer, B. J., Marshall, P. J., et al. 2011, MNRAS, 417, 1621

Emsellem, E., Cappellari, M., Krajnović, D., et al. 2011, MNRAS, 414, 888

Enzi, W., Vegetti, S., Despali, G., Hsueh, J.-W., & Metcalf, R. B. 2020, MNRAS, 496, 1718

Fadely, R., Keeton, C. R., Nakajima, R., & Bernstein, G. M. 2010, ApJ, 711, 246

Fasano, G. & Bonoli, C. 1989, A&AS, 79, 291

Fogarty, L. M. R., Scott, N., Owers, M. S., et al. 2015, MNRAS, 454, 2050

Foreman-Mackey, D., Hogg, D. W., Lang, D., & Goodman, J. 2013, PASP, 125, 306

Freedman, W. L., Madore, B. F., Hatt, D., et al. 2019, ApJ, 882, 34

Freedman, W. L., Madore, B. F., Hoyt, T., et al. 2020, ApJ, 891, 57

Freedman, W. L., Madore, B. F., Scowcroft, V., et al. 2012, ApJ, 758, 24

Frigo, M., Naab, T., Hirschmann, M., et al. 2019, MNRAS, 489, 2702

Furlong, M., Bower, R. G., Crain, R. A., et al. 2017, MNRAS, 465, 722

Furlong, M., Bower, R. G., Theuns, T., et al. 2015, MNRAS, 450, 4486

Galan, A., Peel, A., Joseph, R., Courbin, F., & Starck, J. L. 2021, A&A, 647, A176

Galan, A., Vernardos, G., Peel, A., Courbin, F., & Starck, J.-L. 2022, arXiv e-prints, arXiv:2207.05763

Genel, S., Vogelsberger, M., Springel, V., et al. 2014, MNRAS, 445, 175

Gilman, D., Birrer, S., Nierenberg, A., et al. 2020a, MNRAS, 491, 6077

Gilman, D., Birrer, S., Treu, T., Nierenberg, A., & Benson, A. 2019, MNRAS, 487, 5721

Gilman, D., Bovy, J., Treu, T., et al. 2021, MNRAS, 507, 2432

Gilman, D., Du, X., Benson, A., et al. 2020b, MNRAS, 492, L12

Golse, G. & Kneib, J. P. 2002, A&A, 390, 821

Gomer, M. R., Sluse, D., Van de Vyvere, L., Birrer, S., & Courbin, F. 2022, arXiv e-prints, arXiv:2209.02076

Gomer, M. R. & Williams, L. L. R. 2018, MNRAS, 475, 1987

González-Nuevo, J., Lapi, A., Fleuren, S., et al. 2012, apj, 749, 65

Goodman, J. & Weare, J. 2010, Communications in Applied Mathematics and Computational Science, 5, 65

Graham, A. W. 2019a, MNRAS, 487, 4995

Graham, A. W. 2019b, PASA, 36, e035

Hao, C. N., Mao, S., Deng, Z. G., Xia, X. Y., & Wu, H. 2006, MNRAS, 370, 1339

Henning, J. W., Sayre, J. T., Reichardt, C. L., et al. 2018, ApJ, 852, 97

Hilbert, S., Hartlap, J., White, S. D. M., & Schneider, P. 2009, A&A, 499, 31

Hilbert, S., White, S. D. M., Hartlap, J., & Schneider, P. 2007, MNRAS, 382, 121

Hsueh, J. W., Enzi, W., Vegetti, S., et al. 2020, MNRAS, 492, 3047

Hsueh, J. W., Oldham, L., Spingola, C., et al. 2017, MNRAS, 469, 3713

Jahnke, K. & Wisotzki, L. 2003, MNRAS, 346, 304

Jedrzejewski, R. I. 1987, MNRAS, 226, 747

Kassiola, A. & Kovner, I. 1993, ApJ, 417, 450

Keeton, C. R. 2001, arXiv e-prints, astro

Keeton, C. R., Falco, E. E., Impey, C. D., et al. 2000, ApJ, 542, 74

Keeton, C. R., Gaudi, B. S., & Petters, A. O. 2003, ApJ, 598, 138

Keeton, C. R., Gaudi, B. S., & Petters, A. O. 2005, ApJ, 635, 35

Keeton, C. R. & Kochanek, C. S. 1998, ApJ, 495, 157

Keeton, C. R., Kochanek, C. S., & Seljak, U. 1997, ApJ, 482, 604

Kennedy, J. & Eberhart, R. 1995, in Proceedings of ICNN'95 - International Conference on Neural Networks, Vol. 4, 1942–1948 vol.4

Khetan, N., Izzo, L., Branchesi, M., et al. 2021, A&A, 647, A72

Khochfar, S. & Burkert, A. 2005, MNRAS, 359, 1379

Kochanek, C. S. 2006, Strong Gravitational Lensing (Berlin, Heidelberg: Springer Berlin Heidelberg), 91–268

Kochanek, C. S. 2020, MNRAS, 493, 1725

Kochanek, C. S. 2021, MNRAS, 501, 5021

Kochanek, C. S. & Dalal, N. 2004, ApJ, 610, 69

Kochanek, C. S., Keeton, C. R., & McLeod, B. A. 2001, ApJ, 547, 50

Koopmans, L. V. E., Treu, T., Fassnacht, C. D., Blandford, R. D., & Surpi, G. 2003, ApJ, 599, 70

Kormendy, J. 1982, Saas-Fee Advanced Course, 12, 115

Kormendy, J., Fisher, D. B., Cornell, M. E., & Bender, R. 2009, ApJS, 182, 216

Krajnović, D., Alatalo, K., Blitz, L., et al. 2013, MNRAS, 432, 1768

Krajnović, D., Emsellem, E., Cappellari, M., et al. 2011, MNRAS, 414, 2923

Lagattuta, D. J., Auger, M. W., & Fassnacht, C. D. 2010, ApJ, 716, L185

Lagattuta, D. J., Vegetti, S., Fassnacht, C. D., et al. 2012, MNRAS, 424, 2800

Lauer, T. R. 1985a, MNRAS, 216, 429

Lauer, T. R. 1985b, ApJS, 57, 473

Lefor, A. T., Futamase, T., & Akhlaghi, M. 2013, New A Rev., 57, 1

Li, H., Mao, S., Cappellari, M., et al. 2018, MNRAS, 476, 1765

Li, R., Li, H., Shao, S., et al. 2019, MNRAS, 490, 2124

Liesenborgs, J., de Rijcke, S., Dejonghe, H., & Bekaert, P. 2009, MNRAS, 397, 341

Liller, M. H. 1966, ApJ, 146, 28

Lubini, M., Sereno, M., Coles, J., Jetzer, P., & Saha, P. 2014, MNRAS, 437, 2461

Mao, S. & Schneider, P. 1998, MNRAS, 295, 587

McAlpine, S., Helly, J. C., Schaller, M., et al. 2016, Astronomy and Computing, 15, 72

Metcalf, R. B., Meneghetti, M., Avestruz, C., et al. 2019, A&A, 625, A119

Metcalf, R. B. & Petkova, M. 2014, MNRAS, 445, 1942

Michard, R. 1985, A&AS, 59, 205

Millon, M., Courbin, F., Bonvin, V., et al. 2020a, A&A, 642, A193

Millon, M., Courbin, F., Bonvin, V., et al. 2020b, A&A, 640, A105

Millon, M., Galan, A., Courbin, F., et al. 2020c, A&A, 639, A101

Mitsuda, K., Doi, M., Morokuma, T., et al. 2017, ApJ, 834, 109

Möller, O., Hewett, P., & Blain, A. W. 2003, MNRAS, 345, 1

Mollerach, S. & Roulet, E. 2002, Gravitational Lensing and Microlensing

Mukherjee, S., Koopmans, L. V. E., Metcalf, R. B., et al. 2018, MNRAS, 479, 4108

Mukherjee, S., Koopmans, L. V. E., Metcalf, R. B., et al. 2021, MNRAS, 504, 3455

Navarro, J. F., Frenk, C. S., & White, S. D. M. 1996, ApJ, 462, 563

Nierenberg, A. M., Gilman, D., Treu, T., et al. 2020, MNRAS, 492, 5314

Nightingale, J. W. & Dye, S. 2015, MNRAS, 452, 2940

Park, J. W., Wagner-Carena, S., Birrer, S., et al. 2021, ApJ, 910, 39

Pasquali, A., Ferreras, I., Panagia, N., et al. 2006, ApJ, 636, 115

Peng, C. Y., Ho, L. C., Impey, C. D., & Rix, H.-W. 2010, AJ, 139, 2097

Penoyre, Z., Moster, B. P., Sijacki, D., & Genel, S. 2017, MNRAS, 468, 3883

Pesce, D. W., Braatz, J. A., Reid, M. J., et al. 2020, ApJ, 891, L1

Petkova, M., Metcalf, R. B., & Giocoli, C. 2014, MNRAS, 445, 1954

Philcox, O. H. E., Ivanov, M. M., Simonović, M., & Zaldarriaga, M. 2020, J. Cosmology Astropart. Phys., 2020, 032

Planck Collaboration, Aghanim, N., Akrami, Y., et al. 2020, A&A, 641, A6

Plazas Malagón, A. A. 2020, Symmetry, 12, 494

Powell, D. M., Vegetti, S., McKean, J. P., et al. 2022, arXiv e-prints, arXiv:2207.03375

Refregier, A. 2003, ARA&A, 41, 645

Rest, A., van den Bosch, F. C., Jaffe, W., et al. 2001, AJ, 121, 2431

Riess, A. G., Casertano, S., Yuan, W., et al. 2021, ApJ, 908, L6

Riess, A. G., Casertano, S., Yuan, W., Macri, L. M., & Scolnic, D. 2019, ApJ, 876, 85

Ross, N. R., Assef, R. J., Kochanek, C. S., Falco, E., & Poindexter, S. D. 2009, ApJ, 702, 472

Rusu, C. E., Oguri, M., Minowa, Y., et al. 2016, MNRAS, 458, 2

Rusu, C. E., Wong, K. C., Bonvin, V., et al. 2020, MNRAS, 498, 1440

Schaller, M., Frenk, C. S., Bower, R. G., et al. 2015, MNRAS, 451, 1247

Schaye, J., Crain, R. A., Bower, R. G., et al. 2015, MNRAS, 446, 521

Schmidt, T., Treu, T., Birrer, S., et al. 2022, arXiv e-prints, arXiv:2206.04696

Schneider, P. 2006, Weak Gravitational Lensing (Berlin, Heidelberg: Springer Berlin Heidelberg), 269–451

Schneider, P., Kochanek, C., & Wambsganss, J. 2006, Gravitational Lensing: Strong, Weak and Micro

Schneider, P. & Sluse, D. 2013, A&A, 559, A37

Schneider, P. & Sluse, D. 2014, A&A, 564, A103

Schombert, J., McGaugh, S., & Lelli, F. 2020, AJ, 160, 71

Schramm, T. 1994, A&A, 284, 44

Segers, M. C., Schaye, J., Bower, R. G., et al. 2016, MNRAS, 461, L102

Shah, P., Lemos, P., & Lahav, O. 2021, A&A Rev., 29, 9

Shajib, A. J., Birrer, S., Treu, T., et al. 2019, MNRAS, 483, 5649

Shajib, A. J., Wong, K. C., Birrer, S., et al. 2022, arXiv e-prints, arXiv:2202.11101

Shi, Y. & Eberhart, R. 1998, in 1998 IEEE International Conference on Evolutionary Computation Proceedings. IEEE World Congress on Computational Intelligence (Cat. No.98TH8360), 69–73

Sluse, D., Chantry, V., Magain, P., Courbin, F., & Meylan, G. 2012, A&A, 538, A99

Sluse, D., Surdej, J., Claeskens, J. F., et al. 2003, A&A, 406, L43

Springel, V. 2005, MNRAS, 364, 1105

Springel, V., White, S. D. M., Jenkins, A., et al. 2005, Nature, 435, 629

Stone, C. J., Arora, N., Courteau, S., & Cuillandre, J.-C. 2021, MNRAS, 508, 1870

Suyu, S. H., Auger, M. W., Hilbert, S., et al. 2013, ApJ, 766, 70

Suyu, S. H., Bonvin, V., Courbin, F., et al. 2017, MNRAS, 468, 2590

Suyu, S. H. & Halkola, A. 2010, A&A, 524, A94

Suyu, S. H., Marshall, P. J., Auger, M. W., et al. 2010, ApJ, 711, 201

Suyu, S. H., Marshall, P. J., Blandford, R. D., et al. 2009, ApJ, 691, 277

Suyu, S. H., Treu, T., Hilbert, S., et al. 2014, ApJ, 788, L35

Tagore, A. S., Barnes, D. J., Jackson, N., et al. 2018, MNRAS, 474, 3403

Trayford, J. W., Frenk, C. S., Theuns, T., Schaye, J., & Correa, C. 2019, MNRAS, 483, 744

Trayford, J. W., Theuns, T., Bower, R. G., et al. 2015, MNRAS, 452, 2879

Treu, T. 2010, ARA&A, 48, 87

Treu, T. & Marshall, P. J. 2016, A&A Rev., 24, 11

Trotter, C. S., Winn, J. N., & Hewitt, J. N. 2000, ApJ, 535, 671

Unruh, S., Schneider, P., & Sluse, D. 2017, A&A, 601, A77

Van de Vyvere, L., Gomer, M. R., Sluse, D., et al. 2022a, A&A, 659, A127

Van de Vyvere, L., Sluse, D., Gomer, M. R., & Mukherjee, S. 2022b, A&A, 663, A179

Van de Vyvere, L., Sluse, D., Mukherjee, S., Xu, D., & Birrer, S. 2020, A&A, 644, A108

Verde, L., Treu, T., & Riess, A. G. 2019, Nature Astronomy, 3, 891

Vigroux, L., Souviron, J., Lachieze-Rey, M., & Vader, J. P. 1988, A&AS, 73, 1

Vogelsberger, M., Genel, S., Springel, V., et al. 2014a, Nature, 509, 177

Vogelsberger, M., Genel, S., Springel, V., et al. 2014b, MNRAS, 444, 1518

Wagner, J. 2018, A&A, 620, A86

Wagner-Carena, S., Park, J. W., Birrer, S., et al. 2021, ApJ, 909, 187

Walsh, D., Carswell, R. F., & Weymann, R. J. 1979, Nature, 279, 381

Wambsganss, J. 1998, Living Reviews in Relativity, 1, 12

Wambsganss, J. 2006, Gravitational Microlensing (Berlin, Heidelberg: Springer Berlin Heidelberg), 453–540

Wertz, O., Orthen, B., & Schneider, P. 2018, A&A, 617, A140

Weymann, R. J., Latham, D., Angel, J. R. P., et al. 1980, Nature, 285, 641

Winn, J. N., Hall, P. B., & Schechter, P. L. 2003, ApJ, 597, 672

Wong, K. C., Suyu, S. H., Auger, M. W., et al. 2017, MNRAS, 465, 4895

Wong, K. C., Suyu, S. H., Chen, G. C. F., et al. 2020, MNRAS, 498, 1420

Xu, D., Sluse, D., Gao, L., et al. 2015, MNRAS, 447, 3189

Xu, D., Sluse, D., Schneider, P., et al. 2016, MNRAS, 456, 739

Xu, D. D., Mao, S., Wang, J., et al. 2009, MNRAS, 398, 1235

Yıldırım, A., Suyu, S. H., Chen, G. C. F., & Komatsu, E. 2021, arXiv e-prints, arXiv:2109.14615

Yıldırım, A., Suyu, S. H., & Halkola, A. 2020, MNRAS, 493, 4783

Yoo, J., Kochanek, C. S., Falco, E. E., & McLeod, B. A. 2005, ApJ, 626, 51

Yoo, J., Kochanek, C. S., Falco, E. E., & McLeod, B. A. 2006, ApJ, 642, 22

Yuan, W., Riess, A. G., Macri, L. M., Casertano, S., & Scolnic, D. M. 2019, ApJ, 886, 61